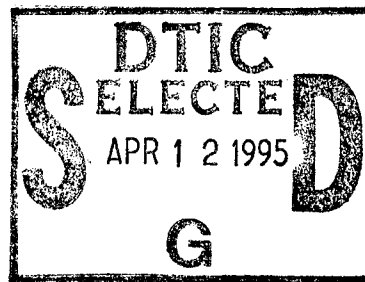


SHUTTLE POTENTIAL AND RETURN ELECTRON EXPERIMENT (SPREE) ELECTROSTATIC ANALYZER (ESA) CALIBRATION REPORT

M.R. Oberhardt
D.A. Hardy
W.E. Slutter
J.O. McGarity
A. Huber

19 June 1994



APPROVED FOR PUBLIC RELEASE; DISTRIBUTION UNLIMITED.

19950410 059



PHILLIPS LABORATORY
Directorate of Geophysics
AIR FORCE MATERIEL COMMAND
HANSCOM AFB, MA 01731-3010

"This technical report has been reviewed and is approved for publication".



DAVID A. HARDY, Chief
Branch Chief
Plasmas & Fields Branch



WILLIAM SWIDER
Deputy Director
Space Physics Division

This report has been reviewed by the ESC Public Affairs Office (PA) and is releaseable to the National Technical Information Service (NTIS).

Qualified requestors may obtain additional copies from the Defense Technical Information Center (DTIC). All others should apply to the National Technical Information Service (NTIS).

If your address has changed, if you wish to be removed from the mailing list, or if the addressee is no longer employed by your organization, please notify PL/TSI, 29 Randolph Road, Hanscom AFB, MA 01731-3010. This will assist us in maintain a current mailing list.

Do not return copies of this report unless contractual obligations or notices on a specific document requires that it be returned.

REPORT DOCUMENTATION PAGE			Form Approved OMB No. 0704-0188	
Public reporting burden for this collection of information is estimated to average 1 hour per response, including the time for reviewing instructions, searching existing data sources, gathering and maintaining the data needed, and completing and reviewing the collection of information. Send comments regarding this burden estimate or any other aspect of this collection of information, including suggestions for reducing this burden, to Washington Headquarters Services, Directorate for Information Operations and Reports, 1215 Jefferson Davis Highway, Suite 1204, Arlington, VA 22202-4302, and to the Office of Management and Budget, Paperwork Reduction Project (0704-0188), Washington, DC 20503.				
1. AGENCY USE ONLY (Leave blank)	2. REPORT DATE 19 June 1994	3. REPORT TYPE AND DATES COVERED Scientific Interim		
4. TITLE AND SUBTITLE Shuttle Potential and Return Electron Experiment (SPREE) Electrostatic Analyzer (ESA) Calibration Report		5. FUNDING NUMBERS PE 6341OF PR 2822 TA 01 WU 01		
6. AUTHOR(S) M.R. Oberhardt, D.A. Hardy, W.E. Slutter *J.O. McGarity, *A. Huber				
7. PERFORMING ORGANIZATION NAME(S) AND ADDRESS(ES) Phillips Laboratory (GPSG) 29 Randolph Road Hanscom AFB, MA 01731-3010		8. PERFORMING ORGANIZATION REPORT NUMBER PL-TR-94-2210 ERP, No. 1155		
9. SPONSORING/MONITORING AGENCY NAME(S) AND ADDRESS(ES)		10. SPONSORING/MONITORING AGENCY REPORT NUMBER		
11. SUPPLEMENTARY NOTES *AMPTEK, Inc., Bedford, MA				
12a. DISTRIBUTION/AVAILABILITY STATEMENT Approved for public release; Distribution unlimited		12b. DISTRIBUTION CODE		
13. ABSTRACT (Maximum 200 words) A pair of 260°, spherical-plate electrostatic analyzer (ESA) units were designed, built and flown as part of the Shuttle Potential and Return Electron Experiment (SPREE) onboard the Tethered Satellite System 1 (TSS-1). Each ESA simultaneously measured ions and electrons in the energy range of 10 eV to 10 keV over an angular fan of 100° by 10°. The deflection voltage of the ESAs was logarithmically stepped through 32 channels at a rate of either 8 (fast mode) or 1 slow mode) sweeps/second. The geometric factors for the two units differed by 2 orders of magnitude so that both ambient and perturbed plasma conditions could be measured during the TSS-1 mission. In this report we present the results of the detailed calibration of these ESAs.				
14. SUBJECT TERMS Particle detectors, Calibration data, Electrostatic analyzers		15. NUMBER OF PAGES 98		
		16. PRICE CODE		
17. SECURITY CLASSIFICATION OF REPORT Unclassified	18. SECURITY CLASSIFICATION OF THIS PAGE Unclassified	19. SECURITY CLASSIFICATION OF ABSTRACT Unclassified	20. LIMITATION OF ABSTRACT SAR	

Accession For	
NTIS CRA&I	<input checked="" type="checkbox"/>
DTIC TAB	<input type="checkbox"/>
Unannounced	<input type="checkbox"/>
Justification	
By	
Distribution /	
Availability Codes	
Dist	Avail and/or Special
A-1	

Contents

1. INTRODUCTION	1
1.1 Electrostatic Analyzer Units	2
1.1.1 Particle Deflection System and Detection Assembly	3
1.1.2 High Voltage Power Supply	3
1.2 Calibration Summary	4
2. CALIBRATION FACILITIES	5
2.1 Electron Calibration System	5
2.2 Ion Calibration System	6
3. ELECTRON ESA CALIBRATION	7
4. ION ESA CALIBRATION	14
5. EFFECTS OF APERTURE AND ANODE SIZES ON DETECTION CAPABILITIES	29
REFERENCES	81

Illustrations

1.	Electron Energy Dependent Geometric Factors for ESA A Zones 1-9 Plotted Versus Energy for the Channel With a Peak Response at Approximately 87 eV	33
2.	Electron Energy Dependent Geometric Factors for ESA A Zones 1-9 Plotted Versus Energy for the Channel With a Peak Response at Approximately 138 eV	34
3.	Electron Energy Dependent Geometric Factors for ESA A Zones 1-9 Plotted Versus Energy for the Channel With a Peak Response at Approximately 270 eV	35,36
4.	Electron Energy Dependent Geometric Factors for ESA A Zones 1-9 Plotted Versus Energy for the Channel With a Peak Response at Approximately 420 eV	37
5.	Electron Energy Dependent Geometric Factors for ESA A Zones 1-9 Plotted Versus Energy for the Channel With a Peak Response at Approximately 660 eV	38
6.	Electron Energy Dependent Geometric Factors for ESA A Zones 1-9 Plotted Versus Energy for the Channel With a Peak Response at Approximately 1040 eV	39
7.	Electron Energy Dependent Geometric Factors for ESA A Zones 1-9 Plotted Versus Energy for the Channel With a Peak Response at Approximately 2040 eV	40
8.	Electron Energy Dependent Geometric Factors for ESA A Zones 1-9 Plotted Versus Energy for the Channel With a Peak Response at Approximately 4000 eV	41
9.	Electron Energy Dependent Geometric Factors for ESA B Zones 0-4 and 6-9 Plotted Versus Energy for the Channel With a Peak Response at 141 eV	42
10.	Electron Energy Dependent Geometric Factors for ESA B Zones 0-3 and 6-9 Plotted Versus Energy for the Channel With a Peak Response at 220 eV	43
11.	Electron Energy Dependent Geometric Factors for ESA B Zones 0-9 Plotted Versus Energy for the Channel With a Peak Response at 275 eV	44,45

Illustrations

12.	Electron Energy Dependent Geometric Factors for ESA B Zones 0-9 Plotted Versus Energy for the Channel With a Peak Response at 440 eV	46
13.	Electron Energy Dependent Geometric Factors for ESA B Zones 0-4 and 6-9 Plotted Versus Energy for the Channel With a Peak Response at 682 eV	47
14.	Electron Energy Dependent Geometric Factors for ESA B Zones 0-9 Plotted Versus Energy for the Channel With a Peak Response at 1070 eV	48
15.	Electron Energy Dependent Geometric Factors for ESA B Zones 0-9 Plotted Versus Energy for the Channel With a Peak Response at 2100 eV	49
16.	Electron Energy Dependent Geometric Factors for ESA B Zones 0-4 and 6-9 Plotted Versus Energy for the Channel With a Peak Response at 4050 eV	50
17.	Electron Energy Dependent Geometric Factors for ESA B Zones 0-9 Plotted Versus Energy for the channel With a Peak Response at 6400 eV	51
18.	Electron Energy Dependent Geometric Factors for ESA B Zones 0-4 and 6-9 Plotted Versus Energy for the Channel With a Peak Response at 10000 eV	52
19.	Normalized Electron Energy Dependent Geometric Factors Plotted vs. Normalized Energy for ESA A Zones 1-9 for the Channel With a Peak Response at 269 eV	53
20.	Normalized Electron Energy Dependent Geometric Factors Plotted vs. Normalized Energy for ESA A Zones 1-9 for the Channel With a Peak Response at 1030 eV	54
21.	Normalized Electron Energy Dependent Geometric Factors Plotted vs. Normalized Energy for ESA B Zones 0, 1, 2, 6, 7, and 9 for the Channel With a Peak Response at 275 eV	55
22.	Normalized Electron Energy Dependent Geometric Factors Plotted vs. Normalized Energy for ESA B Zones 1-4 for the Channel With a Peak Response at 1070 eV	55
23.	Normalized Electron Energy Dependent Geometric Factors Plotted vs. Normalized Energy for ESA A, Electron Zone 5 for the Channels With a Peak Response at 134, 269, 660, 1040, and 3956 eV	56
24.	Normalized Electron Energy Dependent Geometric Factors Plotted vs. Normalized Energy for ESA B, Electron Zone 4 for the Channels With a Peak Response at 141, 275, 682, 1070, and 4100 eV	56
25.	$f(\theta)$, the ESA A Normalized Electron Energy Independent Geometric Factor Averaged Over all Calibrated Energy Channels Plotted Versus Zone Number	57
26.	$f(\theta)$, the ESA B Normalized Electron Energy Independent Geometric Factor Averaged Over all Calibrated Energy Channels Plotted Versus Zone Number	57
27.	Normalized Electron Energy Dependent Geometric Factors Plotted vs. Normalized Energy for ESA A Zones 5 for Pre-flight and Post-flight Data Taken for the Channel With a Peak Response at 1040 eV	58
28.	ESA A Peak Electron Energy Dependent Geometric Factors Plotted as a Function of Energy	59

Illustrations

29.	ESA B Peak Electron Energy Dependent Geometric Factors Plotted as a Functions of Energy	60
30.	ESA A Electron Detection Efficiency Plotted Versus Energy	61
31.	ESA B Electron Detection Efficiency Plotted Versus Energy	61
32.	Central Energy of the ESA A Electron Channels Plotted Versus Channel Number	62
33.	Central Energy of the ESA B Electron Channels Plotted Versus Channel Number	62
34.	Counts Versus Elevation Angle for ESA A Electron Zones 1-9, for the Energy Channel with a Peak Response at 269 eV. The Data are for a Fixed Elevation Angle Within the Angular Scan at 269 eV at a Fixed Azimuth Angle Such That the Elevation Plot Includes the Maximum Counts in the Scan.	63
35.	Counts Versus Azimuthal Angle for ESA A Electron Zones 1-9 for the Energy Channel With a Peak Response at 269 eV. The Data are for a Fixed Elevation Angle Within the Angular Scan at 269 eV at a Fixed Elevation Angle Such That the Azimuth Plot Includes the Maximum Counts in the Scan	64
36.	Ion Energy Dependent Geometric Factors for ESA A Zones 0-9 Plotted Versus Energy for the Energy Channel With a Peak Response at 140 eV	65
37.	Ion Energy Dependent Geometric Factors for ESA A Zones 0-9 Plotted Versus Energy for the Energy Channel With a Peak Response at 430 eV	66
38.	Ion Energy Dependent Geometric Factors for ESA A Zones 0-9 Plotted Versus Energy for the Energy Channel With a Peak Response at 1040 eV	67
39.	Ion Energy Dependent Geometric Factors for ESA A Zones 0-9 Plotted Versus Energy for the Energy Channel With a Peak Response at 6200 eV	68
40.	Ion Energy Dependent Geometric Factors for ESA B Zones 0-9 Plotted Versus Energy for the Energy Channel with a Peak Response at 48 eV	69
41.	Ion Energy Dependent Geometric Factors for ESA B Zones 0-9 Plotted Versus Energy for the Energy Channel With a Peak Response at 210 eV	70
42.	Ion Energy Dependent Geometric Factors for ESA B Zones 0-9 Plotted Versus Energy for the Energy Channel With a Peak Response at 665 eV	71
43.	Ion Energy Dependent Geometric Factors for ESA B Zones 0-9 Plotted Versus Energy for the Energy Channel With a Peak Response at 6200 eV	72
44.	Normalized Ion Energy Dependent Geometric Factors Plotted vs. Normalized Energy for ESA A, Ion Zone 4 for the Energy Channels With a Peak Response at Energies of 140, 430, 1040, and 6200 eV	73

Illustrations

45.	Normalized Ion Energy Dependent Geometric Factors Plotted vs. Normalized Energy for ESA B, Ion Zone 3 for the Energy Channels With a Peak Response at Energies of 48, 220, 660, and 6000 eV	73
46.	$f(\theta)$, the ESA A Normalized Ion Energy Independent Geometric Factor Averaged Over all Calibrated Energy Channels Plotted Versus Zone Number	74
47.	$f(\theta)$, the ESA B Normalized Ion Energy Independent Geometric Factor Averaged Over all Calibrated Energy Channels Plotted Versus Zone Number	74
48.	ESA A Ion Peak Electron Energy Dependent Geometric Factors Plotted as a Function of Energy	75
49.	ESA B Ion Peak Electron Energy Dependent Geometric Factors Plotted as a Function of Energy	76
50.	ESA A Ion Detection Efficiency Plotted Versus Energy	77
51.	ESA B Ion Detection Efficiency Plotted Versus Energy	77
52.	Central Energy of the ESA A Ion Channels Plotted Versus Channel Number	78
53.	Central Energy of the ESA B Ion Channels Plotted Versus Channel Number	78
54.	Counts Versus Elevation Angle for ESA A Ion Zones 1-4 and ESA B Ion Zones 0-4, for the Energy Channel With Peak Response at ~6 keV. The Data are for a Fixed Azimuth Angle Within the Angular Scan Such That the Elevation Plot Includes the Point of Maximum Count Rate in the Scan.	79
55.	Counts Versus Azimuthal Angle for ESA A Ion Zones 0-4 and ESA B Ion Zones 0-4, for the Energy Channel With a Peak Response at ~6 keV. The Data are for a Fixed Elevation Angle Within the Angular Scan Such That the Azimuth Plot Includes the Point of Maximum Count Rate in the Scan.	80

Tables

1.	As Flown ESA Aperture Sizes and Areas	5
2.	Geometric Factor Dependence on the Elevation Angle θ , for ESA A and ESA B Electron Zones	9
3.	Average Calculated Values of $\Delta E/E$ for ESA A and ESA B Electron Zones	14
4.	ESA A Electron Energy Independent Geometric Factors, Fast and Slow Deflection Sweeps	15
5.	ESA B Electron Energy Independent Geometric Factors, Fast and Slow Deflection Sweeps	17
6.	ESA A and ESA B Electron Zone Angular Widths	19
7.	Geometric Factor Dependence on the Elevation Angle θ , for ESA A and ESA B Ion Zones	21
8.	Average, Calculated Values of $\Delta E/E$ for ESA A and ESA B Ion Zones	23
9.	ESA A Ion Energy Independent Geometric Factors, Fast and Slow Deflection Sweeps	24
10.	ESA B Ion Energy Independent Geometric Factors, Fast and Slow Deflection Sweeps	26
11.	ESA A and ESA B Ion Zone Angular Widths	28
12.	ESA Anode Areas	29
13.	Maximum Linear Count Rate Output per Anode	30
14.	Maximum Estimated Linear Flux Measurable per Zone	31
15.	Maximum All IF Count Rates	31
16.	Maximum Estimated Detectable Linear Flux per Zone	32

Acknowledgements

The ESA hardware design and fabrication by Amptek, Inc. were supported by Contract F19628-87-C-0094 with the Geophysics Directorate of the Phillips Laboratory. The authors wish to thank E. Holeman for his work modelling the particle trajectories within the ESA. We thank D. Cooke of the Phillips Laboratory and I. Katz, V.A. Davis, and T.T. Luu of S-Cubed, Inc. for their efforts in modelling the trajectories of particles incident to the ESAs for cases of Orbiter charging. The S-Cubed effort was supported by Contract F19628-90-C-0131 with the Geophysics Directorate. We deeply appreciate the hard work of D. Pendleton of the Geophysics Directorate during the calibration and testing of SPREE. We also wish to acknowledge the labors of Maj C. Lon Enloe in the development, fabrication and testing of the ion calibration source. We thank Capt Brian Maxwell for his assistance in the calibration data acquisition.

Acronyms

CALSYS2	Calibration System 2 Software
CEM	Channel Electron Multiplier
DCORE	Deployer Core Equipment
DPU	Data Processing Unit
ESA	Electrostatic Analyzer
FDR	Flight Data Recorder
FPEG	Fast Pulsed Electron Gun
FWHM	Full Width Half Maximum
GSE	General Support Equipment
KSC	Kennedy Space Center
MCP	Microchannel Plates
MPES	Mission Peculiar Equipment Support Structure
RTMD	Rotary Table Motor Drive
SETS	Shuttle Electrodynamic Tether System
SMB	SPREE Mounting Bracket
SPACE	Spacecraft Particle Correlator Experiment
SPREE	Shuttle Potential and Return Electron Experiment
TSS-1	Tethered Satellite System Mission 1

Nomenclature

A	Effective collecting area
AEZ0-9	ESA A Electron Zones 0-9
AIZ0-9	ESA A Ion Zones 0-9
BEZ0-9	ESA B Electron Zones 0-9
BIZ0-9	ESA B Ion Zones 0-9
E	Energy
E_p	Peak energy in a passband
ε	Detection efficiency
G	Energy independent geometric factor
G(E)	Energy dependent geometric factor
G_p	Peak energy dependent geometric factor in a given energy passband
G_p'	Maximum peak energy dependent geometric factor for a selected detection zone
I_b	Beam intensity
j	Particle flux
Ω	Solid angle of particle detection
R	Particle count rate
R_p	Peak particle count rate
τ_{acc}	Accumulation interval during angular calibration scan

Shuttle Potential and Return Electron Experiment (SPREE) Electrostatic Analyzer (ESA) Calibration Report

1. INTRODUCTION

The Shuttle Potential and Return Electron Experiment (SPREE) was developed as a key component of the Orbiter payload bay experiments studying the electrodynamics of the Tethered Satellite System Mission 1 (TSS-1). The primary goal of the SPREE was to monitor the suprathermal electrons and ions (energies between 10 eV and 10 keV) in the vicinity of the Orbiter during all phases of the Tethered Satellite System Mission 1 (TSS-1) mission. The other goals of SPREE were: 1) to measure the level of positive and negative charging of the Orbiter ground with respect to the space plasma, 2) to not only measure the ambient electron and ion populations present in the SPREE energy range but also to determine the perturbations to those populations produced by the operation of the tether and of the Orbiter-mounted electron beams, and 3) to determine the ion and electron wave-particle interactions (WPI) occurring as a result of Tethered Satellite System Mission 1 (TSS-1) operations.

The SPREE instrumentation to accomplish these goals consisted of seven flight boxes and their associated cabling. These included two multi-angular electrostatic analyzer units (ESAs), each mounted on a rotary table (RTMD), a multiple microprocessor-based Data Processing Unit (DPU), a particle correlator experiment (SPACE) housed within the DPU, and two Flight Data Recorder units (FDRs). This instrumentation suite was installed on the SPREE Mounting Bracket (SMB), located on the port side of the Mission Peculiar Equipment Support

(Received for publication 7 June 1994)

Structure in the Orbiter payload bay. The SPREE shared the Mission Peculiar Equipment Support Structure with the Shuttle Electrodynamic Tether System and the Deployer Core Equipment.

The SPREE ESAs were designed to make simultaneous multi-angular, multi-species measurements. Their design was based upon ESAs flown on the AMPTE, GIOTTO, and CRRES missions^{1,2,3} Each ESA unit houses two triquadrangular electrostatic analyzers with microchannel plate (MCP) detectors and an anode particle detection assembly.^{4,5} An analyzer to measure electrons is nested within the analyzer to measure ions. The combination of the two ESA units mounted on motor driven tables is the first flight of instrumentation in low earth orbit with the capability to fully measure particle distributions in the energy range appropriate to the active experiments onboard the spacecraft. A 90 percent transmission ground screen and its holder mounted on the ESA housing provide an equipotential contour near the aperture that is approximately parallel to the aperture.

1.1 Electrostatic Analyzer Units

The ESA units are core elements of the SPREE hardware. In each nested analyzer, an outer pair of 260° spherical plates is used to measure ions and an inner pair to measure electrons. One end of the analyzer is closed except for a set of entrance apertures, while the other end is attached to the particle detection assembly. Each set of plates consists of two electron-optical elements: a hemispherical analyzer that selects particles in a narrow energy band set by the potential applied between the two plates, followed by an 80° spherical section that acts principally to disperse the particles in position along the surface of the MCP according to their input angle at the entrance aperture. Both elements have the same plate separation and the same potential is applied to each of the elements. Energy analysis and angular dispersion can be achieved with a single 80° pair of spherical plates, but such analyzers have their angular and energy responses smeared together, that is, for an analyzer configured to measure particles in a given energy passband, the passband detected varies with the particle's incident angle at the entrance aperture. The use of the hemispherical analyzer to perform energy analysis produces a detector response where the energy range measured is relatively independent of the incident angle. This in turn provides a more accurate determination of the particle flux. The analyzer is designed so that particles are detected over an angular

¹Hardy, D.A., et al., The Low Energy Plasma Analyzer, accepted for publication in the *IEEE Trans. on Nuclear Science*

²Coates, A.J., et al., A Space-Borne Plasma Analyzer for Three-Dimensional Measurements of the Velocity Distribution, submitted to IEEE 1984 Nuc. Sci. Symposium, Fla.

³Johnstone, A.D., et al., *J. Phys.*, 1987

⁴McGarity, J.O., et al., "Compact Ion/Electron Analyzer for Spaceflight or Laboratory Use." *Reviews of Scientific Instruments*, 63, p. 1973, March 1992

⁵Oberhardt, M.R., et al., "The Shuttle Potential and Return Electron Experiment," *Nuovo Cimento Sezione C*, to be published in 1994

fan of approximately 10° in the plane perpendicular to the plates at the aperture and 100° in the plane parallel to the plates.

1.1.1. PARTICLE DEFLECTION SYSTEM AND DETECTION ASSEMBLY

In the operation of the analyzer, a voltage is applied to each pair of deflection plates. This applied voltage creates a radially directed electric field in the space between the plates. Charged particles entering through the aperture into this space between the plates are accelerated towards the inner plate by the force exerted by the electric field. If the electrical force experienced by a particle approximately balances the centrifugal force produced by the bending of the particle's trajectory in the electric field, then the particle will travel a great circle trajectory through the region between the plates without striking either plate. Particles with either too high or too low an energy for the applied field will collide with either the outer plate or the inner plate, respectively. Similarly, particles of the opposite polarity or neutral particles will undergo multiple collisions with the plates and will not be detected.

The particles on great circle trajectories are focused after passing through the 260° analyzer, so that their angle (β) at the input aperture, within the 100° dimension of the acceptance fan, is imaged as a position along the MCP with an accuracy of approximately 1° . The angle (α) of the particles at the input aperture, in the 10° dimension of the detection fan, is not focused as a position along the MCP. Charged particles that reach the MCP are binned into ten, $10^\circ \times 10^\circ$ zones. With the simultaneous detection of both ions and electrons in the two ESA units, there are a total of 40 zones of particle data. Zone 0 has its lower edge 5° below parallel to the base of the ESA unit while Zone 9 views 5° past the zenith.

Particles that pass through the deflection system reach the ESA's detection assembly. A 52 percent transmissible grounded screen is positioned at the front end of this assembly. Specially designed MCPs intercept the particles as they exit the grounded screen. The trapezoidally-shaped MCPs provide complete coverage of the ESA's acceptance fan. Anodes are positioned after the MCPs to collect the charge cloud emitted by the MCPs. The anodes are split into 10 sections to produce the division of the 100° acceptance fan into the 10 angular zones. The biasing scheme of the MCP/anode assembly provides: post-acceleration of the particles prior to MCP detection, the high voltage necessary to operate the MCPs, and a post-MCP acceleration of the MCP-emitted charge cloud. This configuration results in efficient particle collection at the MCP and efficient charge cloud collection at the anode. The charge pulses collected at the anode are converted into logic pulses by hybrid preamplifier discriminators. These pulses are then transmitted from the ESAs to the Data Processing Unit for conversion into accumulated counts and for use in the Spacecraft Particle Correlator Experiment processing.

1.1.2. HIGH VOLTAGE POWER SUPPLY

A stepping high voltage power supply is used to operate the MCPs and to provide the deflection plate voltages. The deflection plate voltages are swept through a range to measure

electrons and ions at energies from 10 eV to 10 keV. In each deflection sweep, the particle flux is measured in 32 energy channels spaced at equal logarithmic intervals over the energy detection range. The power supply is capable of providing two rates of deflection sweep, obtaining either one complete spectrum per second (slow mode) or eight complete spectra per second (fast mode). During each deflection sweep, the particles are measured simultaneously in all 40 angular zones in the two ESAs.

The high voltage is necessary to operate the MCPs and to provide the deflection plate voltages. The MCPs operate at ± 2500 V at 100 μ A. Four voltages are required for the deflection plates, ranging up to 3400 V for ions and 2500 V for electrons. To generate the voltages, an oscillator was designed to operate at the Orbiter provided bus voltage of 28 V. A step-up transformer uses the oscillator output to drive the input for a pair of Cockcroft-Walton voltage multipliers. The multipliers' filtered output is used by both the MCP biasing scheme and the deflection sweep circuit.

The deflection sweep circuit uses a pair of Amptek HV601 high voltage optocouplers to maintain the deflection plate voltages at the values regulated by the sweep reference circuit. The sweep reference circuit produces 0-8 V over 32 logarithmically spaced steps. The timing of these stepped reference signals is controlled by a clock signal and a reset command. This sweep regulator can operate on two cycles, once per second or eight times per second, or be parked at a selected energy channel.

1.2 Calibration Summary

The Geometric Factor is the factor that converts the counts/second as measured by the analyzers into differential number flux in units of particles/cm² sec ster eV. The geometric factor at any energy step of the analyzers can be expressed as the product of the peak value of the energy dependent geometric factor times a constant that defines the shape of the response function for the analyzers and functions that express the variation in the peak energy dependent geometric factor with angle within the detection fan and with energy. The peak value of the energy dependent geometric factor is defined as the maximum value of the energy dependent geometric factor in the center of the detection fan for unit particle detection efficiency. For ESA A electrons, the peak energy dependent geometric factor is 3.95×10^{-5} cm²-ster, and for ions it is 2.24×10^{-5} cm²-ster. Similarly for ESA B electrons, the peak energy dependent geometric factor is 2.73×10^{-7} cm²-ster and for ions it is 1.39×10^{-7} cm²-ster. For both ESA A and ESA B ions, the $\Delta E/E$ is approximately 11 percent. The $\Delta E/E$ for both ESA A and ESA B electrons is approximately 7 percent. The average ESA A (B) electron elevation angle width is 12.6° (10.0°) and the azimuthal angle width is 8.5° (8.3°). For ions, the average ESA A (B) elevation angle width is 9.2° (10.0°) and the azimuthal angle width is 10.0° (8.8°).

The calibration was performed using identical apertures for ESAs A and B. This was done to speed up the calibration. Following completion of calibration, the geometric factors for flight for the two ESA units were set apart by a factor of approximately 100 by using a smaller

aperture for ESA B. This was done so that accurate measurements could be obtained both in the ambient environment and in highly perturbed plasma conditions resulting from electron beam emission and vehicle charging. The ESA aperture sizes are listed in Table 1.

Table 1. ESA Design Aperture Sizes (cm²)

ESA A Ions (600 μm diameter)	$2.827 \times 10^{-3} = A_1$
ESA A Electrons (400 μm diameter)	$1.257 \times 10^{-3} = A_2$
ESA B Ions (50 μm diameter)	$1.965 \times 10^{-5} = A_3$
ESA B Electrons (40 μm diameter)	$1.257 \times 10^{-5} = A_4$

2. CALIBRATION FACILITIES

2.1 Electron Calibration System⁶

The electron calibration facility consists of a 13" circular, 400 Å thick layer of gold deposited on a quartz flat installed in a cryogenically pumped vacuum chamber. The vacuum chamber is 1 m in diameter and is typically operated at 1×10^{-7} Torr. The layer of gold is isolated from ground so that it can be biased to potentials from 10 V to 50 kV. A monochromatic ultraviolet (UV) source back-illuminates the quartz flat. The UV light enters the back of the gold surface and induces photoemission from the front of the deposited gold. The emitted electrons are accelerated through the voltage drop between the gold surface and a grounded screen in front of that surface. A potential is applied to the gold surface through a specially guarded cable connected to a high voltage power supply external to the vacuum chamber. The ground screen is 90 percent transmissible and mounted on dielectric high voltage standoffs. These standoffs are placed at a distance from the edge of the gold surface sufficient to prevent distortion of the beam structure. Helmholtz coils surround the vacuum chamber and are used to null out the ambient magnetic field to prevent bending of the electron beam at lower energies. The facility's configuration results in the production of a monoenergetic, uniform, monodirectional, and broad electron beam.

The cable applying the potential to the gold and the gold surface itself are guarded to eliminate leakage current to ground, allowing the total emitted current to be monitored using an in-line picoammeter connected directly to the circuit through which the high voltage is applied. This measurement of current emitted from the gold surface allows determination of

⁶Marshall, F.J., et. al., Calibration system for electron detectors in the energy range from 10 eV to 50 keV, *Rev. Sci. Instr.*, 57 (2) 229, 1986

the electron flux in the beam. This total beam flux measurement serves as the absolute calibration standard for the system.

The detector to be calibrated is mounted on a system of computer controlled rotational and translational tables. This gimbaled mounting fixture is placed at the opposite end of the vacuum chamber from the electron beam apparatus. The motion of the fixture allows any instrument's apertures to be positioned at any angle relative to the incoming beam. The setting of the beam energy, positioning of the instrument, the determination of the beam intensity, and the calibration data acquisition are all controlled through the CALSYS2⁷ software package.

2.2 Ion Calibration System⁸

An electron bombardment ion source configured as a Kaufman thruster is used as a calibration standard for ion detectors over the energy range 2 eV to 20 keV. The ion beam is well collimated by a drift tube, and the output of the source is stable to a few percent drift per hour. The beam is nearly monoenergetic, with a full width half maximum (FWHM) in energy of 1 percent over most of the operating range. Several features of the beam change significantly from low (< 100 eV) to high (> 100 eV) energy. These deviations from an ideal beam are well characterized and are accounted for in the calibration of the ion ESAs.

The ion calibration system can be attached to one end of the vacuum chamber by a 23 cm conflat flange. The system itself is constructed of 25 cm conflat tees and straight sections of 20 cm stainless steel tubing with 25 cm conflat flanges. The resulting drift tube is 1.8 m in length exclusive of the high voltage feedthroughs at the inlet end of the system.

The drift tube's first two chambers are independently pumped by small turbomolecular pumps. The calibration system operates most efficiently with a 1 sccm flow of N₂. The differential pumping along the drift tube helps to limit the maximum vacuum chamber pressure to 2×10^{-6} Torr. The length of the drift tube sets the angular width of the ion beam to approximately 2°.

The ionization chamber of the source is biased to the desired operating beam voltage. The positive end of the source's filament is biased to -30 V with respect to the ionization chamber so that electrons are accelerated into the ionization chamber with sufficient energy to ionize the N₂. Because the filament is external to the ionization chamber, ions are created in an equipotential region and the large anomalous ion temperature typical of Kaufman thrusters is avoided. Magnetic field coils wound on the outside of the tube containing the source provide a 10 G field inside the ionization chamber. Trapping of electrons by this field increases the probability that an electron will undergo an ionizing collision before reaching the wall and this

⁷Wilton, R., Private communication, 1990

⁸Enloe, C.L., Private communication, "Operation of an ion calibration source over four orders of magnitude in energy," 1991

more than doubles the source's output. An acceleration grid is biased to -50 V with respect to ground to prevent energetic electrons from exiting the source and mixing with the ion beam.

3. ELECTRON ESA CALIBRATION

For this calibration, data were taken in energy passbands with a peak response at approximately 27 eV, 45 eV, 87 eV, 138 eV, 270 eV, 420 eV, 660 eV, 1040 eV, 2000 eV, 4 keV, 6 keV, and 10 keV. Within each passband the instrument response was determined over a two dimensional grid in angle for a series of energies. At each energy the angular response of the instrument was integrated to give the energy dependent geometric factor. Not all angular scans performed gave usable data. Data omissions will be discussed at the appropriate points in the explanation of the analyses performed. Also, to obtain statistically significant data more quickly, the ESA B electron calibration was performed using the A_2 aperture.

The ESA's measured flux is given by,

$$j(E) = R / \int G(E) dE \quad (1)$$

with $j(E)$ equal to the differential number flux in units of electrons/cm²-sec-ster-eV, R is the measured count rate in counts per second in a selected energy channel, and $G(E)$ equal to the energy dependent geometric factor. The integration of energy dependent geometric factors is performed over the passband of the energy channel.

The energy dependent geometric factor may be written as

$$G(E) = A(E) \epsilon(E) \Omega(E), \quad (2)$$

where $A(E)$ is the effective collecting area, $\epsilon(E)$ is the detector's efficiency in that energy channel, and $\Omega(E)$ is the solid angle over which the particles are detected. The geometry of the sensor basically determines $A(E)$ and $\Omega(E)$ and their dependence on energy is therefore limited. The efficiency is dependent upon energy but does not vary greatly within an energy passband. These characteristics mean that the shape of the response curve of the instrument, that is, the shape of the plot of the energy dependent geometric factor versus energy, will be almost invariant in energy and zone. Figures 1a-8b show the energy dependent geometric factors plotted versus energy for each zone for each energy passband used in the data analysis for ESA A. Figures 9a-18b show similar data for ESA B.

The energy independent geometric factor, G , is the integral of the energy dependent geometric factor, $G(E)$, over the energy passband for a specific energy channel,

$$G = \int G(E) dE \quad (3)$$

This integral may be approximated by,

$$G = \sum [G(E_i) * (E_{i+1} - E_{i-1}) / 2] \quad (4)$$

The summation in Eq. (4) is over the energies in a specific energy channel chosen in the calibration. Equation (4) may be rewritten as

$$G = G_p E_p \sum \{ [G(E_i) / G_p] * [(E_{i+1} - E_{i-1}) / 2E_p] \} \quad (5)$$

where G_p and E_p are the peak energy dependent geometric factor and the energy at which the peak occurs in a passband, respectively, for a given energy channel. G_p is dependent on $\epsilon(E)$ and the ESA zone. The summation in Eq. (5) is over the normalized response curve. Since the shape of the response curve is fixed, this summation will equal a constant A that is invariant of the energy passband sampled. Equation (5) may then be written as

$$G = A G_p E_p. \quad (6)$$

The value of the constant A is obtained by integrating the normalized response curves. Examples of these normalized curves are shown in Figures 19a-22. In Figures 23 and 24, similar normalized curves for ESA A Electron Zone 5 and ESA B Electron Zone 4 are plotted for several different energy channels. Figures 5a-24 demonstrate that the shape of the response curve is reasonably invariant in both energy and in zone.

Since G_p is dependent upon detector efficiency and the zone, the equation for G can be written as

$$G = A G_p' E_p \epsilon(E) f(\theta) \quad (7)$$

where G_p' is the maximum peak energy dependent geometric factor over all energies and zones and $\epsilon(E)$, and $f(\theta)$ are the functions that give the variation in G_p' with energy and angle. The calibration then consists of obtaining sufficient data to allow determination of these five quantities.

A value for A was calculated for every zone for each passband calibrated. These A values were averaged over all energies for each zone and then averaged across all zones. For ESA A electrons, the average A was calculated to be 7.55×10^{-2} , in dimensionless units, with a standard deviation of 2.62×10^{-3} and an uncertainty in determination of the mean A of 8.73×10^{-4} . For ESA B electrons, the mean A was 7.61×10^{-2} , with a standard deviation of 2.92×10^{-3} , and an uncertainty in determination of the mean A of 9.23×10^{-4} . The agreement in the value of A for the two ESAs and the small value of the standard deviation for the A's support the contention that A is reasonably constant. The passbands used for ESA A electrons were those with peak response at 87, 136, 269, 420, 660, 1040, 2040, and 3950 eV. For ESA B, the

passbands used were those with peak response at 141, 220, 275, 440, 682, 1070, 2100, 4050, and 6400 eV, and 10 keV.

To calculate $f(\theta)$, the energy independent geometric factor was calculated for all passbands for which data were taken. In each passband used, the calculated energy independent geometric factor in each zone was normalized to the peak value of the energy independent geometric factor in AEZ5 for ESA A and in BEZ4 for ESA B. The normalized value for a given zone was found to be approximately the same for the different energy passbands with the exception of AEZ9 which showed some significant variation. These normalized values were then averaged in each zone over all of the passbands calibrated. These averages are listed in Table 2 and plotted versus zone in Figures 25 and 26 for ESA A and ESA B, respectively. In addition, the expected cosine falloff is plotted in each figure. ESA A does not demonstrate a smooth falloff in geometric factor across the zones, while ESA B more closely matches the expected cosine falloff. It is not understood why this happens. The determined average $f(\theta)$ values were used in the final calculations of the energy independent geometric factor.

Table 2. Electron $f(\theta)$

Zone	ESA A	ESA B
0	0.508	0.602
1	0.743	0.859
2	0.679	0.951
3	0.963	0.996
4	0.930	1.000
5	1.000	0.950
6	0.826	0.883
7	1.060	0.943
8	0.826	0.851
9	0.824	0.905

Due to a failure of the preamplifier for AEZ0 during calibration, no preflight calibration data were taken for this zone. Instead, the AEZ0 calibration was performed post-flight. Data were collected in the 270 eV and 1 keV passbands. Values of the constant A determined for AEZ0 post-flight were compared to those obtained in the other zones preflight and post-flight. All were in good agreement. For this reason the average A for ESA A was used to determine the geometric factors for AEZ0. This left only the determination of the parameter $f(\theta)$ for AEZ0, since the other four quantities needed in Eq. (7) to determine G would be valid for AEZ0. The $f(\theta)$ determination was performed, normalizing to AEZ5 as before. We also determined, by a comparison of the peak geometric factors preflight and post-flight in both passbands, that only

AEZ6 exhibited a significant drop in response post-flight. The agreement pre- and post-flight of the detector response is well illustrated in Figure 27. No post-flight electron calibration was performed with ESA B.

The $\epsilon(E)$ dependence was calculated from the variation with energy of the value of the peak electron energy dependent geometric factor for ESAs A and B. This variation is shown for each zone in Figures 28 and 29. To calculate $\epsilon(E)$ these values were normalized to the peak energy dependent geometric factor for ESA A for the passband with a peak response at 269 eV in Zone 5 and for ESA B for the passband with a peak response at 275 eV for Zone 4. At each energy passband these normalized peak values were then averaged over zone. The normalized and averaged values are plotted in Figures 30 and 31.

The expected electron detection efficiency of channel electron multipliers can be found in Kurz *et al*⁹ and Paschmann *et al*¹⁰. The postacceleration (pre-MCP) voltage applied to the electrons is +400 V. Adding that voltage to the peak at ~270 eV yields an efficiency peak in our data at ~670 eV. This is 330 V lower than that given by Paschmann *et al*¹⁰. We attribute this to the difference between the MCP absolute detection efficiency and the ESA (that is, instrumental) efficiency and to the nature of the determination of the expected values given in the literature. Kurz' curve is a composite of data taken from numerous sources under varying test conditions. In Kurz' work there is no discussion of the errors in the expected value. Kurz' curve gives an efficiency peak at ~200 eV. Paschmann *et al.* show all known measurements of channel electron multiplier efficiency collected up until publication (1970), and demonstrate that a variety of factors influence the determination of efficiency of an entire instrument. The equations for ESA electron detection efficiency are determined to be:

ESA A electrons:

$$\epsilon(E) = 0.8175, \quad \text{for } E < 87 \text{ eV} \quad (8)$$

$$\epsilon(E) = 0.077 + 0.383 * \text{Log } E, \quad \text{for } 87 \text{ eV} < E < 269 \text{ eV} \quad (9)$$

$$\epsilon(E) = 1.667 - 0.275 * \text{Log } E, \quad \text{for } E > 269 \text{ eV} \quad (10)$$

ESA B electrons:

$$\epsilon(E) = 0.7732, \quad \text{for } E < 141 \text{ eV} \quad (11)$$

$$\epsilon(E) = -0.909 + 0.783 * \text{Log } E, \quad \text{for } 87 \text{ eV} < E < 269 \text{ eV} \quad (12)$$

$$\epsilon(E) = 1.637 - 0.265 * \text{Log } E, \quad \text{for } E > 269 \text{ eV} \quad (13)$$

⁹Kurz, E.A., Channel Electron Multipliers, *American Laboratory*, March, 1979

¹⁰Paschmann, G., *et. al.*, *Rev. of Sci. Instr.*, 41, 1706, 1970

The data points from the very low energy scans were not used in the fitting, because it was determined that for these scans there was significant spreading of the calibration beam. The beam spreading produces an overestimate of the calibration beam density and a resulting underestimate of the energy dependent geometric factor. This in turn creates an erroneously low value of the efficiency. The postacceleration applied to the electrons is intended to provide approximately unity detection efficiency for the MCP below the peak detection efficiency. No tests were done to decouple the ESA detection efficiency from the MCP absolute detection efficiency. We do not attribute all the efficiency drop below 270 eV to beam spreading. The sharp difference between the data points at 220 eV and 275 eV for ESA B shown in Figure 29 is evidence that the efficiency drop below 270 eV may be due in part to an instrument optical effect. For this reason we fit to a straight line the observed efficiency fall off down to energies of 100 eV. Below 100 eV the efficiency is set equal to the value determined at 100 eV.

Next, the central energy of the ESA as a function of voltage step was determined. The SPREE ESA can operate in either the Fast Deflection Sweep Mode or the Slow Deflection Sweep Mode. The deflection voltage is smoothly decayed for the Fast Mode of 8 sweeps/sec. In Fast Mode, the first pulse of the high voltage supply logarithmic digital-to-analog converter (Log DAC) resets the supply to the highest deflection voltage and the second step initiates the decay. Subsequent steps simply maintain the high voltage supply's natural logarithmic decay and serve as data accumulation boundaries. The Slow Mode is one sweep/sec and is operated differently from the Fast Mode. At the first step of the sweep, 31, the highest voltage is set and maintained. The next step sets the supply to the next lowest voltage and then maintains that voltage until the next pulse is issued. The Slow Mode is effectively a step and hold as opposed to the constant decay of the Fast Mode.

The calibrations were performed by maintaining individual voltage steps and collecting data for a specific beam energy. The peak energies, E_p , obtained then should match the central energies when the ESA is operating in Slow Mode. The equations for peak energy for Slow Mode for ESA A and ESA B were determined from the E_p preflight data shown in Figures 32 and 33. These data were fit with a linear regression to yield the Slow Mode energy equations, for $n = 0-31$, with 0 indicating the lowest energy step of the detector. If the power supplies were following the natural logarithmic decay as designed, then the Fast Mode central energies could be obtained from Slow Mode central energies, since they represent equally spaced points on the curve of the decay of the power supply. To determine the central energies for Fast Mode, the following method was employed. The logarithms of the Slow Mode $E_p(n)$ values were calculated. Then, adjacent logarithms of the Slow Mode central energies were averaged. The logarithmic inverse of these averages was then determined to obtain the Fast Mode central energies. A linear regression was performed on the calculated points to obtain the parameters required to describe the Fast Mode energy equations. The Fast and Slow Mode electron energy equations for ESA A and ESA B are shown in Eqs. (14)-(17).

$$E_p(n) = 8.366 * 10^{0.0977n}, \quad \text{for ESA A Fast Sweep Electrons} \quad (14)$$

$$E_p(n) = 9.362 * 10^{0.0977n}, \quad \text{for ESA A Slow Sweep Electrons} \quad (15)$$

$$E_p(n) = 8.134 * 10^{0.0983n}, \quad \text{for ESA B Fast Sweep Electrons} \quad (16)$$

$$E_p(n) = 9.109 * 10^{0.0983n}, \quad \text{for ESA B Slow Sweep Electrons} \quad (17)$$

A post-flight voltage calibration was performed on ESA A to check whether the method of determining the Fast Mode central energies was correct. For this determination the SPREE was operated in the Fast Sweep Mode. The SPREE was positioned in the calibration beam at the angular orientation that produced the maximum response. The SPREE Data Processing Unit and Ground Support Equipment were used to monitor the count rate measured by the ESAs. The electron beam energy was varied to produce the maximum count rate in a particular channel. This beam energy was taken as the energy of the peak response for that energy channel. These data points are shown in Figure 32. One should note that these data agree with the calculated curve for the Fast Sweep Mode energy channels.

Monitoring of the plate voltages during the mission to determine the stability of the energy channels was limited. Over the range of the deflection sweep voltage, the housekeeping signal for the deflection monitor covers a range from 8.0 Volts to 0.008 Volts (0-31). The deflection voltages and accompanying monitor values can be found in *Huber et al*¹¹. The analog housekeeping data are passed through a 16 channel multiplexer and then digitized by a 12 bit analog-to-digital (A/D) converter with a 10 Volt full scale range. In theory, a 0.0024 Volt accuracy should have been provided with this scheme. The lowest housekeeping monitor voltage, 0.008, converts to three bit resolution, but the increment to the next 2 or 3 steps above it is ~0.002 Volts. Unfortunately, these increments between steps at the bottom end of the sweep supply are less than the conversion accuracy of the A/D converter. Ideally, an A/D with greater resolution should have been chosen. Further compounding the issue is the location of the converter. The converter is in the Data Processing Unit and the deflection monitor voltages are generated inside each ESA. The ESA is referenced to chassis and the deflection monitor signal is single ended and routed through two harnesses prior to reaching the Data Processing Unit. Enough noise is generated to mask the lowest 12 steps of the deflection monitor.

The deflection monitor telemetry for Fast Mode and Slow Mode differ also. In Slow Mode, the highest level (8.0) Volts is reported twice at the beginning of each sweep and then subsequent steps show the value following the natural logarithmic decline. In the Fast Mode, the highest value is reported only once and all subsequent steps follow the natural decline. The Data Processing Unit samples the deflection monitor voltage a few hundred microseconds

¹¹Huber, et. al., *Prototype Instrumentation and Design Studies*, PL-TR-91-2236, September, 1991

after the step pulse is sent within the high voltage supply. In Fast Mode, the deflection voltage is smoothly decayed from the beginning and never held at a fixed position so that there would be 32 unique values reported by the deflection monitor (if there were enough bits and a clean signal). In the Slow Mode, the sampling occurs so quickly after the step pulse is sent (with respect to the decay time), that the supply monitor is being polled before the supply has decayed to the level for that voltage step. In Slow Mode, then, the reported deflection monitor voltages lag the actual deflection voltage by a step.

Plugging the equations for ϵ and E_p and the values of A , G_p' , and $f(\theta)$ into Eq. (7), and accounting for the as-flown aperture size of the B electron ESA leads to the formation of a set of equations to determine G for each of the electron zones at any energy for both ESA A and ESA B in both Fast and Slow deflection sweep modes. From these equations, a lookup table has been created and used as an analysis tool. The tabulated values for G for ESA A electrons and ESA B electrons are in Tables 4 and 5, for aperture sizes of 400 μm for the ESA A electrons and 40 μm for the ESA B electrons.

Two other characteristics of the instrument that we can derive from the calibration data are the ESAs' $\Delta E/E$ s and the angular acceptance of the zones. The values of $\Delta E/E$ were determined from the E_p values and the data taken from the plots of the energy dependent geometric factor with peak responses at 269, 420, 660, and 3956 eV for ESA A electrons and at 275, 440, 1070, and 2100 eV for ESA B electrons. The $\Delta E/E$ for each zone for each of the above passbands was determined from the FWHM of the plots. The FWHMs were then averaged across the energy channels for each zone (see Table 3). The standard deviations for all of these averaged $\Delta E/E$ values were all less than 1 percent. One should note that the variation across the zones for $\Delta E/E$ for ESA A and ESA B matches the variation seen across the zones for the $f(\theta)$ values. Based upon the ESA dimensions, the maximum $\Delta E/E$ for the electron ESAs was calculated to be 11.1 percent.⁴

The angular acceptance is defined in terms of the angles (α) and (β). The elevation angle, (β), is the focused angle determined by the anode shape, and the azimuthal angle, (α), is the unfocused angle determined by the deflection plate separation. The elevation angle calculated from the analyzer dimensions is 10° and the azimuthal angle is 8°. The angular width of the detection zones in both the elevation and azimuthal angles was determined in the following manner. The angles at which the maximum count rate occurred were determined for the angular scans at energies of 269, 660 and 2040 eV for ESA A and 275, 440, and 2100 eV for ESA B. These were the scans at the energy of the maximum response for the passbands calibrated. Plots were made of the counts versus elevation angle at the azimuthal angle where the count maximum occurred as were plots of the counts versus azimuthal angle at the elevation angle where the count maximum occurred.

Examples of these plots of the single angle scans of the counts are shown in Figures 34 and 35. The angles given are the angular position of the ESA in the calibration facility coordinate system. Figure 34 highlights the overlap between ESA zones in the elevation angle and Figure 35 illustrates the accumulated position loss of the calibration table in the course of

Table 3. Electron $\Delta E/E$

Zone	ESA A (Percent)	ESA B (Percent)
0	5.80	7.74
1	6.00	7.73
2	6.70	7.83
3	7.60	7.99
4	7.50	7.36
5	7.60	7.33
6	6.40	7.57
7	6.80	7.37
8	6.40	7.80
9	6.90	7.59
Avg	6.80	7.60

a scan. From these plots, the angular width was determined as the FWHM in each zone. These values were then averaged across energy to provide the angular width for each zone. The angular widths for the electron ESAs are given in Table 6. There was considerable variance in the ESA A azimuthal angles across energy in some of the zones. No such variance was seen in the elevation angle averages for either ESA. There is also an unexplained difference between ESA A and ESA B in the magnitude of the average elevation angles.

The unusual $f(\theta)$ results for ESA A electrons and the ESA A electron $\Delta E/E$ results along with the ESA A electron angular widths and variance, indicate that there may be some slight misalignment of the deflection plates in the ESA A electron unit. The electron calibration data were relatively noise-free. Only one instance of minor cross-talk was observed: when AEZ3 registered peak counts, AEZ2 and AEZ4 showed a fraction of that peak response. Dark count and UV contamination scans were performed for a center energy of 1 keV and demonstrated that the electron background counts were very low. Also, all ESA A and ESA B electron zones were noise-free a few hours following initial high voltage turn-on during the TSS-1 mission.

4. ION ESA CALIBRATION

The ion ESAs were calibrated using the same basic methods as for the electron ESAs. Some additional steps, however, had to be taken with the ion data due to differences between the ion and electron beam systems as well as noise in some of the ESA ion zones. The SPREE calibration was the first time that the ion beam system⁸ was used to calibrate an ion ESA. Previous Geophysics Directorate ion ESAs were calibrated using the electron beam with the

Table 4. ESA A Electron Fast Deflection Sweep Geometric Factors

Energy Step	<u>AEZ0</u>	<u>AEZ1</u>	<u>AEZ2</u>	<u>AEZ3</u>	<u>AEZ4</u>	<u>AEZ5</u>	<u>AEZ6</u>	<u>AEZ7</u>	<u>AEZ8</u>	<u>AEZ9</u>
0	1.04E-05	1.52E-05	1.38E-05	1.97E-05	1.90E-05	2.04E-05	1.69E-05	2.17E-05	1.68E-05	1.68E-05
1	1.30E-05	1.90E-05	1.73E-05	2.46E-05	2.38E-05	2.56E-05	2.11E-05	2.72E-05	2.11E-05	2.11E-05
2	1.62E-05	2.38E-05	2.17E-05	3.08E-05	2.98E-05	3.20E-05	2.64E-05	3.40E-05	2.64E-05	2.64E-05
3	2.03E-05	2.98E-05	2.72E-05	3.86E-05	3.73E-05	4.01E-05	3.31E-05	4.26E-05	3.31E-05	3.30E-05
4	2.55E-05	3.73E-05	3.40E-05	4.83E-05	4.67E-05	5.02E-05	4.15E-05	5.33E-05	4.14E-05	4.14E-05
5	3.19E-05	4.67E-05	4.26E-05	6.05E-05	5.84E-05	6.28E-05	5.19E-05	6.67E-05	5.19E-05	5.18E-05
6	3.99E-05	5.84E-05	5.34E-05	7.57E-05	7.32E-05	7.87E-05	6.50E-05	8.36E-05	6.49E-05	6.48E-05
7	5.00E-05	7.32E-05	6.68E-05	9.49E-05	9.16E-05	9.85E-05	8.14E-05	1.05E-04	8.13E-05	8.12E-05
8	6.26E-05	9.16E-05	8.37E-05	1.19E-04	1.15E-04	1.23E-04	1.02E-04	1.31E-04	1.02E-04	1.02E-04
9	7.84E-05	1.15E-04	1.05E-04	1.49E-04	1.44E-04	1.54E-04	1.28E-04	1.64E-04	1.28E-04	1.27E-04
10	9.82E-05	1.44E-04	1.31E-04	1.86E-04	1.80E-04	1.93E-04	1.60E-04	2.05E-04	1.60E-04	1.59E-04
11	1.26E-04	1.85E-04	1.69E-04	2.40E-04	2.31E-04	2.49E-04	2.06E-04	2.64E-04	2.05E-04	2.05E-04
12	1.65E-04	2.42E-04	2.21E-04	3.13E-04	3.03E-04	3.25E-04	2.69E-04	3.46E-04	2.69E-04	2.68E-04
13	2.16E-04	3.16E-04	2.88E-04	4.09E-04	3.95E-04	4.25E-04	3.51E-04	4.52E-04	3.51E-04	3.50E-04
14	2.81E-04	4.11E-04	3.76E-04	5.33E-04	5.15E-04	5.54E-04	4.58E-04	5.88E-04	4.57E-04	4.56E-04
15	3.66E-04	5.35E-04	4.89E-04	6.94E-04	6.70E-04	7.21E-04	5.96E-04	7.66E-04	5.95E-04	5.94E-04
16	4.55E-04	6.66E-04	6.08E-04	8.64E-04	8.34E-04	8.97E-04	7.41E-04	9.53E-04	7.40E-04	7.39E-04
17	5.55E-04	8.11E-04	7.41E-04	1.05E-03	1.02E-03	1.09E-03	9.03E-04	1.16E-03	9.02E-04	9.00E-04
18	6.75E-04	9.87E-04	9.02E-04	1.28E-03	1.24E-03	1.33E-03	1.10E-03	1.41E-03	1.10E-03	1.10E-03
19	8.21E-04	1.20E-03	1.10E-03	1.56E-03	1.50E-03	1.62E-03	1.34E-03	1.72E-03	1.33E-03	1.33E-03
20	9.97E-04	1.46E-03	1.33E-03	1.89E-03	1.83E-03	1.96E-03	1.62E-03	2.09E-03	1.62E-03	1.62E-03
21	1.21E-03	1.77E-03	1.62E-03	2.30E-03	2.22E-03	2.38E-03	1.97E-03	2.53E-03	1.97E-03	1.96E-03
22	1.47E-03	2.15E-03	1.96E-03	2.78E-03	2.69E-03	2.89E-03	2.39E-03	3.07E-03	2.39E-03	2.38E-03
23	1.78E-03	2.60E-03	2.37E-03	3.37E-03	3.26E-03	3.50E-03	2.89E-03	3.72E-03	2.89E-03	2.89E-03
24	2.15E-03	3.15E-03	2.87E-03	4.08E-03	3.94E-03	4.23E-03	3.50E-03	4.50E-03	3.50E-03	3.49E-03
25	2.60E-03	3.80E-03	3.47E-03	4.93E-03	4.76E-03	5.12E-03	4.23E-03	5.44E-03	4.23E-03	4.22E-03
26	3.14E-03	4.59E-03	4.19E-03	5.95E-03	5.74E-03	6.18E-03	5.10E-03	6.56E-03	5.10E-03	5.09E-03
27	3.78E-03	5.53E-03	5.05E-03	7.17E-03	6.92E-03	7.44E-03	6.15E-03	7.91E-03	6.14E-03	6.13E-03
28	4.55E-03	6.65E-03	6.08E-03	8.62E-03	8.33E-03	8.95E-03	7.40E-03	9.52E-03	7.39E-03	7.38E-03
29	5.46E-03	7.99E-03	7.30E-03	1.04E-02	1.00E-02	1.08E-02	8.89E-03	1.14E-02	8.88E-03	8.87E-03
30	6.55E-03	9.58E-03	8.75E-03	1.24E-02	1.20E-02	1.29E-02	1.07E-02	1.37E-02	1.07E-02	1.06E-02
31	7.84E-03	1.15E-02	1.05E-02	1.49E-02	1.44E-02	1.54E-02	1.28E-02	1.64E-02	1.27E-02	1.27E-02

Table 4. (cont'd) ESA A Electron Slow Deflection Sweep Geometric Factors

Energy Step	<u>AEZ0</u>	<u>AEZ1</u>	<u>AEZ2</u>	<u>AEZ3</u>	<u>AEZ4</u>	<u>AEZ5</u>	<u>AEZ6</u>	<u>AEZ7</u>	<u>AEZ8</u>	<u>AEZ9</u>
0	1.16E-05	1.70E-05	1.55E-05	2.20E-05	2.12E-05	2.28E-05	1.89E-05	2.43E-05	1.89E-05	1.88E-05
1	1.45E-05	2.12E-05	1.94E-05	2.75E-05	2.66E-05	2.86E-05	2.36E-05	3.04E-05	2.36E-05	2.36E-05
2	1.82E-05	2.66E-05	2.43E-05	3.45E-05	3.33E-05	3.58E-05	2.96E-05	3.80E-05	2.96E-05	2.95E-05
3	2.28E-05	3.33E-05	3.04E-05	4.32E-05	4.17E-05	4.48E-05	3.71E-05	4.76E-05	3.70E-05	3.70E-05
4	2.85E-05	4.17E-05	3.81E-05	5.41E-05	5.22E-05	5.61E-05	4.64E-05	5.97E-05	4.64E-05	4.63E-05
5	3.57E-05	5.22E-05	4.77E-05	6.77E-05	6.54E-05	7.03E-05	5.81E-05	7.47E-05	5.80E-05	5.79E-05
6	4.47E-05	6.54E-05	5.97E-05	8.48E-05	8.19E-05	8.80E-05	7.27E-05	9.35E-05	7.27E-05	7.26E-05
7	5.60E-05	8.19E-05	7.48E-05	1.06E-04	1.02E-04	1.10E-04	9.11E-05	1.17E-04	9.10E-05	9.08E-05
8	7.01E-05	1.03E-04	9.36E-05	1.33E-04	1.28E-04	1.38E-04	1.14E-04	1.47E-04	1.14E-04	1.14E-04
9	8.77E-05	1.28E-04	1.17E-04	1.66E-04	1.61E-04	1.73E-04	1.43E-04	1.84E-04	1.43E-04	1.42E-04
10	1.10E-04	1.62E-04	1.48E-04	2.09E-04	2.02E-04	2.17E-04	1.80E-04	2.31E-04	1.80E-04	1.79E-04
11	1.45E-04	2.11E-04	1.93E-04	2.74E-04	2.65E-04	2.85E-04	2.35E-04	3.03E-04	2.35E-04	2.35E-04
12	1.89E-04	2.76E-04	2.52E-04	3.58E-04	3.46E-04	3.72E-04	3.07E-04	3.95E-04	3.07E-04	3.07E-04
13	2.46E-04	3.60E-04	3.29E-04	4.67E-04	4.51E-04	4.85E-04	4.01E-04	5.16E-04	4.01E-04	4.00E-04
14	3.21E-04	4.69E-04	4.29E-04	6.08E-04	5.88E-04	6.32E-04	5.22E-04	6.71E-04	5.22E-04	5.21E-04
15	4.12E-04	6.03E-04	5.51E-04	7.82E-04	7.55E-04	8.12E-04	6.71E-04	8.63E-04	6.71E-04	6.70E-04
16	5.03E-04	7.35E-04	6.72E-04	9.53E-04	9.20E-04	9.90E-04	8.18E-04	1.05E-03	8.17E-04	8.16E-04
17	6.12E-04	8.95E-04	8.18E-04	1.16E-03	1.12E-03	1.20E-03	9.96E-04	1.28E-03	9.95E-04	9.93E-04
18	7.44E-04	1.09E-03	9.95E-04	1.41E-03	1.36E-03	1.47E-03	1.21E-03	1.56E-03	1.21E-03	1.21E-03
19	9.05E-04	1.32E-03	1.21E-03	1.72E-03	1.66E-03	1.78E-03	1.47E-03	1.89E-03	1.47E-03	1.47E-03
20	1.10E-03	1.61E-03	1.47E-03	2.08E-03	2.01E-03	2.16E-03	1.79E-03	2.30E-03	1.79E-03	1.78E-03
21	1.33E-03	1.95E-03	1.78E-03	2.53E-03	2.44E-03	2.62E-03	2.17E-03	2.79E-03	2.17E-03	2.16E-03
22	1.62E-03	2.36E-03	2.16E-03	3.06E-03	2.96E-03	3.18E-03	2.63E-03	3.38E-03	2.63E-03	2.62E-03
23	1.96E-03	2.86E-03	2.61E-03	3.71E-03	3.58E-03	3.85E-03	3.18E-03	4.09E-03	3.18E-03	3.17E-03
24	2.36E-03	3.46E-03	3.16E-03	4.48E-03	4.33E-03	4.66E-03	3.85E-03	4.95E-03	3.84E-03	3.84E-03
25	2.85E-03	4.18E-03	3.81E-03	5.41E-03	5.23E-03	5.62E-03	4.65E-03	5.97E-03	4.64E-03	4.63E-03
26	3.44E-03	5.04E-03	4.60E-03	6.53E-03	6.31E-03	6.78E-03	5.60E-03	7.21E-03	5.60E-03	5.59E-03
27	4.15E-03	6.07E-03	5.54E-03	7.86E-03	7.59E-03	8.16E-03	6.75E-03	8.68E-03	6.74E-03	6.73E-03
28	4.98E-03	7.29E-03	6.66E-03	9.45E-03	9.13E-03	9.82E-03	8.11E-03	1.04E-02	8.11E-03	8.09E-03
29	5.98E-03	8.75E-03	7.99E-03	1.13E-02	1.10E-02	1.18E-02	9.74E-03	1.25E-02	9.73E-03	9.71E-03
30	7.17E-03	1.05E-02	9.58E-03	1.36E-02	1.31E-02	1.41E-02	1.17E-02	1.50E-02	1.17E-02	1.16E-02
31	8.57E-03	1.25E-02	1.14E-02	1.63E-02	1.57E-02	1.69E-02	1.39E-02	1.79E-02	1.39E-02	1.39E-02

Table 5. ESA B Electron Fast Deflection Sweep Geometric Factors

Energy Step	<u>BEZ0</u>	<u>BEZ1</u>	<u>BEZ2</u>	<u>BEZ3</u>	<u>BEZ4</u>	<u>BEZ5</u>	<u>BEZ6</u>	<u>BEZ7</u>	<u>BEZ8</u>	<u>BEZ9</u>
0	7.87E-08	1.12E-07	1.24E-07	1.30E-07	1.31E-07	1.24E-07	1.15E-07	1.23E-07	1.11E-07	1.18E-07
1	9.87E-08	1.41E-07	1.56E-07	1.63E-07	1.64E-07	1.56E-07	1.45E-07	1.54E-07	1.39E-07	1.48E-07
2	1.24E-07	1.77E-07	1.95E-07	2.05E-07	2.06E-07	1.95E-07	1.81E-07	1.94E-07	1.75E-07	1.86E-07
3	1.55E-07	2.21E-07	2.45E-07	2.57E-07	2.58E-07	2.45E-07	2.28E-07	2.43E-07	2.19E-07	2.33E-07
4	1.95E-07	2.78E-07	3.07E-07	3.22E-07	3.23E-07	3.07E-07	2.85E-07	3.05E-07	2.75E-07	2.93E-07
5	2.44E-07	3.48E-07	3.85E-07	4.04E-07	4.05E-07	3.85E-07	3.58E-07	3.82E-07	3.45E-07	3.67E-07
6	3.06E-07	4.37E-07	4.83E-07	5.06E-07	5.08E-07	4.83E-07	4.49E-07	4.79E-07	4.33E-07	4.60E-07
7	3.84E-07	5.48E-07	6.06E-07	6.35E-07	6.37E-07	6.06E-07	5.63E-07	6.01E-07	5.42E-07	5.77E-07
8	4.81E-07	6.87E-07	7.60E-07	7.96E-07	7.99E-07	7.60E-07	7.06E-07	7.53E-07	6.80E-07	7.24E-07
9	6.04E-07	8.61E-07	9.53E-07	9.98E-07	1.00E-06	9.53E-07	8.85E-07	9.45E-07	8.53E-07	9.07E-07
10	7.57E-07	1.08E-06	1.20E-06	1.25E-06	1.26E-06	1.19E-06	1.11E-06	1.19E-06	1.07E-06	1.14E-06
11	9.50E-07	1.35E-06	1.50E-06	1.57E-06	1.58E-06	1.50E-06	1.39E-06	1.49E-06	1.34E-06	1.43E-06
12	1.19E-06	1.70E-06	1.88E-06	1.97E-06	1.98E-06	1.88E-06	1.75E-06	1.86E-06	1.68E-06	1.79E-06
13	1.55E-06	2.22E-06	2.45E-06	2.57E-06	2.58E-06	2.45E-06	2.28E-06	2.43E-06	2.19E-06	2.33E-06
14	2.13E-06	3.04E-06	3.37E-06	3.53E-06	3.54E-06	3.37E-06	3.13E-06	3.34E-06	3.02E-06	3.21E-06
15	2.91E-06	4.15E-06	4.59E-06	4.81E-06	4.83E-06	4.59E-06	4.27E-06	4.55E-06	4.11E-06	4.37E-06
16	3.73E-06	5.33E-06	5.89E-06	6.17E-06	6.20E-06	5.89E-06	5.47E-06	5.84E-06	5.28E-06	5.61E-06
17	4.56E-06	6.50E-06	7.19E-06	7.53E-06	7.57E-06	7.19E-06	6.68E-06	7.13E-06	6.44E-06	6.85E-06
18	5.56E-06	7.93E-06	8.78E-06	9.19E-06	9.23E-06	8.77E-06	8.15E-06	8.70E-06	7.86E-06	8.35E-06
19	6.78E-06	9.67E-06	1.07E-05	1.12E-05	1.13E-05	1.07E-05	9.94E-06	1.06E-05	9.58E-06	1.02E-05
20	8.25E-06	1.18E-05	1.30E-05	1.36E-05	1.37E-05	1.30E-05	1.21E-05	1.29E-05	1.17E-05	1.24E-05
21	1.00E-05	1.43E-05	1.59E-05	1.66E-05	1.67E-05	1.58E-05	1.47E-05	1.57E-05	1.42E-05	1.51E-05
22	1.22E-05	1.74E-05	1.93E-05	2.02E-05	2.03E-05	1.93E-05	1.79E-05	1.91E-05	1.73E-05	1.83E-05
23	1.48E-05	2.12E-05	2.34E-05	2.45E-05	2.46E-05	2.34E-05	2.17E-05	2.32E-05	2.10E-05	2.23E-05
24	1.80E-05	2.57E-05	2.84E-05	2.97E-05	2.99E-05	2.84E-05	2.64E-05	2.82E-05	2.54E-05	2.70E-05
25	2.18E-05	3.11E-05	3.44E-05	3.60E-05	3.62E-05	3.44E-05	3.20E-05	3.41E-05	3.08E-05	3.28E-05
26	2.64E-05	3.76E-05	4.16E-05	4.36E-05	4.38E-05	4.16E-05	3.87E-05	4.13E-05	3.73E-05	3.97E-05
27	3.19E-05	4.55E-05	5.03E-05	5.27E-05	5.30E-05	5.03E-05	4.68E-05	4.99E-05	4.51E-05	4.79E-05
28	3.85E-05	5.49E-05	6.08E-05	6.36E-05	6.39E-05	6.07E-05	5.64E-05	6.02E-05	5.44E-05	5.79E-05
29	4.64E-05	6.62E-05	7.32E-05	7.67E-05	7.70E-05	7.32E-05	6.80E-05	7.26E-05	6.56E-05	6.97E-05
30	5.58E-05	7.96E-05	8.81E-05	9.23E-05	9.27E-05	8.81E-05	8.19E-05	8.74E-05	7.89E-05	8.39E-05
31	6.71E-05	9.57E-05	1.06E-04	1.11E-04	1.11E-04	1.06E-04	9.83E-05	1.05E-04	9.47E-05	1.01E-04

Table 5. (cont'd) ESA B Electron Slow Deflection Sweep Geometric Factors

Energy Step	<u>BEZ0</u>	<u>BEZ1</u>	<u>BEZ2</u>	<u>BEZ3</u>	<u>BEZ4</u>	<u>BEZ5</u>	<u>BEZ6</u>	<u>BEZ7</u>	<u>BEZ8</u>	<u>BEZ9</u>
0	8.81E-08	1.26E-07	1.39E-07	1.46E-07	1.46E-07	1.39E-07	1.29E-07	1.38E-07	1.25E-07	1.32E-07
1	1.11E-07	1.58E-07	1.74E-07	1.83E-07	1.84E-07	1.74E-07	1.62E-07	1.73E-07	1.56E-07	1.66E-07
2	1.39E-07	1.98E-07	2.19E-07	2.29E-07	2.30E-07	2.19E-07	2.03E-07	2.17E-07	1.96E-07	2.08E-07
3	1.74E-07	2.48E-07	2.74E-07	2.87E-07	2.89E-07	2.74E-07	2.55E-07	2.72E-07	2.46E-07	2.61E-07
4	2.18E-07	3.11E-07	3.44E-07	3.60E-07	3.62E-07	3.44E-07	3.20E-07	3.41E-07	3.08E-07	3.28E-07
5	2.73E-07	3.90E-07	4.31E-07	4.52E-07	4.54E-07	4.31E-07	4.01E-07	4.28E-07	3.86E-07	4.11E-07
6	3.43E-07	4.89E-07	5.41E-07	5.67E-07	5.69E-07	5.41E-07	5.03E-07	5.37E-07	4.84E-07	5.15E-07
7	4.30E-07	6.13E-07	6.79E-07	7.11E-07	7.14E-07	6.78E-07	6.30E-07	6.73E-07	6.07E-07	6.46E-07
8	5.39E-07	7.69E-07	8.51E-07	8.91E-07	8.95E-07	8.51E-07	7.91E-07	8.44E-07	7.62E-07	8.10E-07
9	6.76E-07	9.65E-07	1.07E-06	1.12E-06	1.12E-06	1.07E-06	9.91E-07	1.06E-06	9.55E-07	1.02E-06
10	8.48E-07	1.21E-06	1.34E-06	1.40E-06	1.41E-06	1.34E-06	1.24E-06	1.33E-06	1.20E-06	1.27E-06
11	1.06E-06	1.52E-06	1.68E-06	1.76E-06	1.77E-06	1.68E-06	1.56E-06	1.66E-06	1.50E-06	1.60E-06
12	1.33E-06	1.90E-06	2.11E-06	2.20E-06	2.21E-06	2.10E-06	1.96E-06	2.09E-06	1.88E-06	2.00E-06
13	1.82E-06	2.60E-06	2.88E-06	3.01E-06	3.03E-06	2.87E-06	2.67E-06	2.85E-06	2.58E-06	2.74E-06
14	2.49E-06	3.56E-06	3.94E-06	4.12E-06	4.14E-06	3.93E-06	3.66E-06	3.90E-06	3.52E-06	3.75E-06
15	3.38E-06	4.82E-06	5.33E-06	5.58E-06	5.61E-06	5.33E-06	4.95E-06	5.29E-06	4.77E-06	5.08E-06
16	4.13E-06	5.89E-06	6.51E-06	6.82E-06	6.85E-06	6.51E-06	6.05E-06	6.46E-06	5.83E-06	6.20E-06
17	5.03E-06	7.18E-06	7.95E-06	8.32E-06	8.36E-06	7.94E-06	7.38E-06	7.88E-06	7.11E-06	7.57E-06
18	6.14E-06	8.76E-06	9.69E-06	1.01E-05	1.02E-05	9.68E-06	9.00E-06	9.61E-06	8.67E-06	9.23E-06
19	7.48E-06	1.07E-05	1.18E-05	1.24E-05	1.24E-05	1.18E-05	1.10E-05	1.17E-05	1.06E-05	1.12E-05
20	9.11E-06	1.30E-05	1.44E-05	1.51E-05	1.51E-05	1.44E-05	1.34E-05	1.42E-05	1.29E-05	1.37E-05
21	1.11E-05	1.58E-05	1.75E-05	1.83E-05	1.84E-05	1.75E-05	1.62E-05	1.73E-05	1.56E-05	1.66E-05
22	1.35E-05	1.92E-05	2.12E-05	2.22E-05	2.23E-05	2.12E-05	1.97E-05	2.11E-05	1.90E-05	2.02E-05
23	1.63E-05	2.33E-05	2.58E-05	2.70E-05	2.71E-05	2.58E-05	2.40E-05	2.56E-05	2.31E-05	2.45E-05
24	1.98E-05	2.83E-05	3.13E-05	3.27E-05	3.29E-05	3.12E-05	2.90E-05	3.10E-05	2.80E-05	2.98E-05
25	2.40E-05	3.42E-05	3.79E-05	3.97E-05	3.98E-05	3.78E-05	3.52E-05	3.75E-05	3.39E-05	3.60E-05
26	2.90E-05	4.14E-05	4.58E-05	4.80E-05	4.82E-05	4.58E-05	4.25E-05	4.54E-05	4.10E-05	4.36E-05
27	3.50E-05	5.00E-05	5.53E-05	5.79E-05	5.82E-05	5.53E-05	5.14E-05	5.48E-05	4.95E-05	5.27E-05
28	4.23E-05	6.03E-05	6.67E-05	6.99E-05	7.02E-05	6.67E-05	6.20E-05	6.62E-05	5.97E-05	6.35E-05
29	5.09E-05	7.26E-05	8.04E-05	8.42E-05	8.45E-05	8.03E-05	7.46E-05	7.97E-05	7.19E-05	7.65E-05
30	6.12E-05	8.73E-05	9.66E-05	1.01E-04	1.02E-04	9.65E-05	8.97E-05	9.58E-05	8.65E-05	9.20E-05
31	7.34E-05	1.05E-04	1.16E-04	1.21E-04	1.22E-04	1.16E-04	1.08E-04	1.15E-04	1.04E-04	1.10E-04

polarity on the ESA deflection plates reversed. Like the electron calibration, the ESA B ion calibration was performed with the ESA A aperture. One instrumental difference between the electron and ion ESAs is that the electron ESAs use one MCP for zones 0-9 while the ion ESAs use one MCP for zones 0-4 and another MCP for zones 5-9.

Table 6. Angular Width of Electron ESA Zones Averaged Across Selected Energy Channel (degrees)

ESA Zone	Elevation (β)	Azimuth (α)
AEZ1	15.3	7.4
AEZ2	11.9	7.7
AEZ3	12.2	8.6
AEZ4	11.3	8.3
AEZ5	12.2	9.5
AEZ6	11.7	9.1
AEZ7	13.7	8.6
AEZ8	11.9	7.9
AEZ0	13.0	9.2
BEZ0	9.2	7.5
BEZ1	10.1	8.1
BEZ2	9.5	9.3
BEZ3	9.9	9.3
BEZ4	10.0	8.3
BEZ5	9.5	9.0
BEZ6	9.4	7.9
BEZ7	10.5	7.2
BEZ8	10.2	7.8
BEZ9	11.5	8.6

The ion beam drift tube pressure was kept to $\sim 5 \times 10^{-5}$ Torr to prevent the degradation of the beam. For all ion beam energies used in this calibration, the FWHM of the beam was approximately $0.1E_{\text{beam}}$. Since this is an order of magnitude less than the $\Delta E/E$ for the ion ESA this had a negligible effect on the calibration. Ion beam purity was considered to be unity for the purposes of this calibration. We determined that the current density at the ESA detection location was 0.82 of that at the location of the Faraday cup.

The CALSYS2 determination of $G(E)$ does not account for any variation in the beam current during a scan. Consequently, if any current drifts occur within a calibration scan, the $G(E)$ determined by CALSYS2 can be in error. There were a number of ion calibration scans in which there was a significant drift of the ion beam's current. Adjustments to the energy dependent geometric factors obtained in these scans were attempted. These adjustments were based on the assumption that the ion beam current drifted linearly throughout the duration of the scan. Using this assumption did not give energy dependent geometric factors consistent with those obtained when the current density was stable. We recommend all future users of the ion beam system disregard all ion calibration data files that contain a significant current drift.

The energy passbands calibrated for ESA A ions were those with peak responses at approximately 140, 430, 1040, 6200, and 7600 eV. For ESA B ion calibration, the energy passbands calibrated were those with peak responses at 48, 60, 92, 220, 665, 6200, and 7600 eV. The value for A for ESA B data centered at 48 eV was not used, since the scan was cut off at the high end of the energy passband. The data for ESA A centered at 38 eV were not used because of observations of some unusual beam spreading. Figures 36a-43c show examples of the ion energy dependent geometric factors for each zone of the ESA A and ESA B. (Recall that the ESA B data were obtained using the ESA A ion aperture.) In Figures 44 and 45, similar normalized curves for ESA A Ion Zone 3 and ESA B Ion Zone 4 are plotted for several energy channels. Figures 36a-45 demonstrate that the shape of the response curve for the ions is relatively invariant in both energy and zone for both ESAs. For ESA A ions, the mean A was calculated to be 1.01×10^{-1} , in dimensionless units, with a standard deviation of 1.96×10^{-3} and an uncertainty in determination of the mean A equal to 6.20×10^{-4} . For ESA B ions, the mean A was 1.07×10^{-1} , with a standard deviation of 1.88×10^{-3} , and an uncertainty in determination of the mean A equal to 5.94×10^{-4} .

A significant level of background noise was present throughout the calibration in BIZ5 and BIZ6. Occasional noise was present in BIZ2. This can be seen in Figures 40-43. This noise did not affect the determination of the constant A, however. This background level proved to be a factor mainly in the choice of G_p .

To check rejection characteristics, a 5 keV electron beam was scanned by the ESA B ion zones with the ESA A sized aperture for ESA central energies of 1077, 442, and 93 eV with a data accumulation interval of 1 minute. The ion count rates were all well below 1 per second, except for those zones already identified as noisy. The noisy zones, BIZ5 and BIZ6, showed no appreciable count rate increase during these rejection tests. Dark count and UV contamination scans were performed as well at a center energy of 1 keV. Both showed count rates of $< 1/\text{second}$. In flight, there was some noise in AIZ4, BIZ4 and BIZ5. After approximately 3 hours of on-orbit operation, this noise level had settled to approximately 10 counts/second in those 3 zones. Payload bay pressure was low (10^{-5} to 10^{-6} Torr) and therefore not a factor in producing the noise observed.

For the $f(\theta)$ determination, the ion energy-independent geometric factor in each zone for each energy passband characterized was normalized to the peak value of ion energy-independent geometric factor in AIZ4 for ESA A and in BIZ4 for ESA B for that energy passband. The normalized factor for a given zone was found to be approximately the same for the different energy channels for both ESA A and ESA B. These normalized factors were then averaged for each zone over all of the energy channels calibrated. These average values are shown in Table 7. Values of this normalized, averaged ion G plotted versus zone are shown in Figures 46 and 47 for ESA A and ESA B, respectively. In addition, the expected cosine falloff is plotted in each figure. ESA A shows a sharp difference in response between the two MCPs used. For the zones for each MCP the falloff with angle is greater than a cosine falloff. The $f(\theta)$ normalization for ESA A ions was performed using AIZ4 instead of AIZ3 to smooth out some of the disparity

between the two plates. ESA B demonstrates a smooth falloff in geometric factor across the zones, with again a greater than cosine falloff in the outer zones. This greater than cosine falloff is not understood. The determined $f(\theta)$ values were used in the final calculations of the ion energy independent geometric factor.

Table 7. Ion $f(\theta)$

Zone	ESA A	ESA B
0	0.465	0.442
1	0.686	0.770
2	0.843	0.887
3	1.010	0.989
4	1.000	1.000
5	0.790	0.963
6	0.767	0.913
7	0.721	0.801
8	0.599	0.647
9	0.406	0.400

The expected ion detection efficiency is shown in Kurz *et al.*⁹ Ion detection efficiency has been shown to be dependent on the species being measured, but the basic curve shape remains the same for all species. According to studies performed, there are mass-dependent efficiency variations for ions through mass 40 for ions incident on the channel electron multiplier with energies of less than 2-4 keV. No attempts were made to compensate for species in the determination of the efficiencies for the ion ESAs and no data were identified in the literature for MCP detection efficiency of nitrogen ions. Figures 48 and 49 show the peak ion energy dependent geometric factors for ESA A and ESA B. The ESA A and ESA B ion detection efficiency curves are shown in Figures 50 and 51. The efficiency curves were obtained from fits to the normalized peak ion energy dependent geometric factors, shown as asterisks on the plot.

The peak, energy dependent geometric factors were normalized to the value of G_p at 6200 eV from Zone 3 for ESA A and 6020 eV from Zone 4 for ESA B (ESA B G_p' given for aperture size A_1). BIZ5 had a higher G_p at 6020 eV, but that result was due to the high level of background counts in that zone, so it was not used as G_p' . The measured ion ESAs' efficiency curves are in good agreement with the published data. For ESA A, 90 percent detection efficiency begins at ~1.8 keV and for ESA B at ~750 eV. Since the ion post-acceleration (pre-MCP) was 2100 V this gives energies for 90 percent efficiency of 3.9 keV and 2.85 keV. From Kurz' data, for monoatomic ions, 90 percent detection efficiency should begin at 4 keV and for

H_1^+ , at ~2 keV. The difference between the low energy ion detection efficiencies and the location of the efficiency peaks of ESA A and ESA B are unexpected. The explanation of this disparity is that one of the MCP pairs in ESA A had operating characteristics very different from its mate and the pair in ESA B, as was evidenced in the $f(\theta)$ plots. Eqs. (18)-(21) yield the efficiency values for ESA A and ESA B ion detection.

ESA A ions:

$$\epsilon(E) = 0.202 + 0.208 * \text{Log } E, \quad \text{for } E < 6200 \text{ eV} \quad (18)$$

$$\epsilon(E) = 2.298 - 0.342 * \text{Log } E, \quad \text{for } E > 6200 \text{ eV} \quad (19)$$

ESA B ions:

$$\epsilon(E) = 0.590 + 0.108 * \text{Log } E, \quad \text{for } E < 6200 \text{ eV} \quad (20)$$

$$\epsilon(E) = 1.542 - 0.143 * \text{Log } E, \quad \text{for } E > 6200 \text{ eV} \quad (21)$$

The central energies for both Fast and Slow Modes for the ion ESAs were determined as for the electron ESAs. The deflection monitor information discussed in Section III applies to the ion ESAs as well. The ion beam was operated at a beam current such that shifts in center energy did not need to be taken into account.⁸ Figures 52 and 53 show the E_p data, the E_p curve fits to those data for Slow Mode, and the calculated Fast Mode E_p curves, for ESA A and ESA B, respectively. Eqs. (22)-(25) give the energy equations for the ion ESAs.

$$E_p(n) = 8.755 * 10^{0.0965n}, \quad \text{for ESA A Fast Sweep Ions} \quad (22)$$

$$E_p(n) = 9.784 * 10^{0.0965n}, \quad \text{for ESA A Slow Sweep Ions} \quad (23)$$

$$E_p(n) = 9.26 * 10^{0.0956n}, \quad \text{for ESA B Fast Sweep Ions} \quad (24)$$

$$E_p(n) = 10.26 * 10^{0.0956n}, \quad \text{for ESA B Slow Sweep Ions} \quad (25)$$

A set of equations to determine G for each of the ion zones at any energy for both ESAs A and B in both Fast and Slow deflection sweep modes is derived by inserting into Eq. (7) the equations for ϵ and E_p and the values of A, G_p' , and $f(\theta)$ and by accounting for the as-flown aperture size of the B ion ESA. From these equations, a lookup table has been created and used as an analysis tool. Also, note that, due to a wiring harness problem, incomplete (that is fewer energy scans than the other electron zones) but sufficient data were collected for the calibration of BIZ5. The tabulated values for G for ESA A ions and ESA B ions are in Tables 9 and 10, for aperture sizes of 600 μm for the ESA A and 50 μm for the ESA B. Sufficient post-

flight data were taken to show that the ion ESAs were operating properly. These data are not adequate for performing a post-flight calibration.

As was done for the electrons, we can calculate the $\Delta E/E$ and angular acceptance for the ion ESAs. From the E_p values and the data taken for scans at energies of 140, 420, and 6200 eV for ESA A ions and at energies of 210, 655, and 6020 eV for ESA B ions, the values of $\Delta E/E$ were determined. The $\Delta E/E$ for each zone for each of the above scans was determined from the FWHM of the data in the figures corresponding to the scans listed. The FWHMs were then averaged across the energy channels for each zone. ESA A shows some difference in $\Delta E/E$ between the lowest energy checked and the higher two energies; this feature can also be seen in Figure 44. ESA B shows no significant differences in $\Delta E/E$ at the various energies checked. The maximum expected $\Delta E/E$ for the ion ESAs based on the ESA dimensions was calculated to be 14.8 percent.⁴ The actual values obtained are lower, as was the case for the electron ESAs. Table 8 contains the values obtained from the data analyzed.

Table 8. Ion $\Delta E/E$

Zone	ESA A (Percent)	ESA B (Percent)
0	10.4	10.3
1	10.4	10.9
2	10.7	10.8
3	11.2	10.9
4	11.1	10.0
5	10.4	10.3
6	10.2	10.3
7	10.7	11.0
8	10.7	11.1
9	9.6	10.6
Avg	10.5	10.7

The ion elevation angle calculated from the analyzer dimensions is 10° and the azimuthal angle is 10° . The angular width of the detection zones in both the elevation and azimuthal angles was determined in the following manner. The angle at which the maximum count rate occurred was determined for the angular scan at the following energies; 140, 420 and 6240 eV for ESA A and 210, 655, and 6020 eV for ESA B. These scans are at the peak response in energy of the channels calibrated. Plots were made of the counts versus elevation angle at the azimuthal angle where the count maximum occurred and of the counts versus

Table 9. ESA A Ion Fast Deflection Sweep Geometric Factors

Energy Step	<u>AIZ0</u>	<u>AIZ1</u>	<u>AIZ2</u>	<u>AIZ3</u>	<u>AIZ4</u>	<u>AIZ5</u>	<u>AIZ6</u>	<u>AIZ7</u>	<u>AIZ8</u>	<u>AIZ9</u>
0	3.68E-06	5.43E-06	6.66E-06	8.00E-06	7.91E-06	6.25E-06	6.07E-06	5.70E-06	4.74E-06	3.21E-06
1	4.83E-06	7.12E-06	8.74E-06	1.05E-05	1.04E-05	8.20E-06	7.96E-06	7.47E-06	6.21E-06	4.21E-06
2	6.32E-06	9.32E-06	1.14E-05	1.37E-05	1.36E-05	1.07E-05	1.04E-05	9.78E-06	8.13E-06	5.52E-06
3	8.25E-06	1.22E-05	1.49E-05	1.79E-05	1.77E-05	1.40E-05	1.36E-05	1.28E-05	1.06E-05	7.20E-06
4	1.08E-05	1.59E-05	1.95E-05	2.34E-05	2.31E-05	1.83E-05	1.77E-05	1.67E-05	1.38E-05	9.39E-06
5	1.40E-05	2.06E-05	2.53E-05	3.04E-05	3.01E-05	2.38E-05	2.31E-05	2.17E-05	1.80E-05	1.22E-05
6	1.82E-05	2.68E-05	3.29E-05	3.95E-05	3.91E-05	3.09E-05	3.00E-05	2.82E-05	2.34E-05	1.59E-05
7	2.36E-05	3.48E-05	4.27E-05	5.13E-05	5.07E-05	4.00E-05	3.89E-05	3.65E-05	3.04E-05	2.06E-05
8	3.06E-05	4.51E-05	5.53E-05	6.64E-05	6.56E-05	5.19E-05	5.04E-05	4.73E-05	3.93E-05	2.67E-05
9	3.95E-05	5.83E-05	7.16E-05	8.60E-05	8.49E-05	6.71E-05	6.51E-05	6.12E-05	5.09E-05	3.45E-05
10	5.11E-05	7.53E-05	9.25E-05	1.11E-04	1.10E-04	8.67E-05	8.42E-05	7.91E-05	6.57E-05	4.46E-05
11	6.59E-05	9.72E-05	1.19E-04	1.43E-04	1.42E-04	1.12E-04	1.09E-04	1.02E-04	8.48E-05	5.75E-05
12	8.50E-05	1.25E-04	1.54E-04	1.85E-04	1.83E-04	1.44E-04	1.40E-04	1.32E-04	1.09E-04	7.42E-05
13	1.09E-04	1.61E-04	1.98E-04	2.38E-04	2.35E-04	1.86E-04	1.80E-04	1.69E-04	1.41E-04	9.56E-05
14	1.41E-04	2.08E-04	2.55E-04	3.06E-04	3.03E-04	2.39E-04	2.32E-04	2.18E-04	1.81E-04	1.23E-04
15	1.81E-04	2.67E-04	3.28E-04	3.94E-04	3.89E-04	3.08E-04	2.98E-04	2.80E-04	2.33E-04	1.58E-04
16	2.33E-04	3.43E-04	4.21E-04	5.06E-04	5.00E-04	3.95E-04	3.83E-04	3.60E-04	2.99E-04	2.03E-04
17	2.99E-04	4.41E-04	5.41E-04	6.50E-04	6.42E-04	5.07E-04	4.92E-04	4.62E-04	3.84E-04	2.61E-04
18	3.83E-04	5.65E-04	6.94E-04	8.33E-04	8.23E-04	6.50E-04	6.31E-04	5.93E-04	4.93E-04	3.34E-04
19	4.91E-04	7.24E-04	8.89E-04	1.07E-03	1.06E-03	8.34E-04	8.09E-04	7.60E-04	6.32E-04	4.29E-04
20	6.29E-04	9.28E-04	1.14E-03	1.37E-03	1.35E-03	1.07E-03	1.04E-03	9.74E-04	8.10E-04	5.49E-04
21	8.05E-04	1.19E-03	1.46E-03	1.75E-03	1.73E-03	1.37E-03	1.33E-03	1.25E-03	1.04E-03	7.03E-04
22	1.03E-03	1.52E-03	1.87E-03	2.24E-03	2.21E-03	1.75E-03	1.70E-03	1.59E-03	1.33E-03	8.99E-04
23	1.32E-03	1.94E-03	2.38E-03	2.86E-03	2.83E-03	2.24E-03	2.17E-03	2.04E-03	1.70E-03	1.15E-03
24	1.68E-03	2.48E-03	3.05E-03	3.66E-03	3.62E-03	2.86E-03	2.77E-03	2.61E-03	2.17E-03	1.47E-03
25	2.15E-03	3.17E-03	3.89E-03	4.68E-03	4.62E-03	3.65E-03	3.54E-03	3.33E-03	2.77E-03	1.88E-03
26	2.75E-03	4.05E-03	4.97E-03	5.97E-03	5.90E-03	4.66E-03	4.52E-03	4.25E-03	3.53E-03	2.40E-03
27	3.50E-03	5.17E-03	6.34E-03	7.62E-03	7.53E-03	5.95E-03	5.77E-03	5.42E-03	4.51E-03	3.06E-03
28	4.47E-03	6.59E-03	8.09E-03	9.72E-03	9.60E-03	7.59E-03	7.36E-03	6.92E-03	5.75E-03	3.90E-03
29	5.70E-03	8.40E-03	1.03E-02	1.24E-02	1.22E-02	9.67E-03	9.39E-03	8.82E-03	7.33E-03	4.97E-03
30	7.14E-03	1.05E-02	1.29E-02	1.55E-02	1.53E-02	1.21E-02	1.18E-02	1.10E-02	9.18E-03	6.23E-03
31	8.61E-03	1.27E-02	1.56E-02	1.87E-02	1.85E-02	1.46E-02	1.42E-02	1.33E-02	1.11E-02	7.52E-03

Table 9. (cont'd) ESA A Ion Slow Deflection Sweep Geometric Factors

Energy Step	<u>AIZ0</u>	<u>AIZ1</u>	<u>AIZ2</u>	<u>AIZ3</u>	<u>AIZ4</u>	<u>AIZ5</u>	<u>AIZ6</u>	<u>AIZ7</u>	<u>AIZ8</u>	<u>AIZ9</u>
0	4.22E-06	6.22E-06	7.63E-06	9.17E-06	9.06E-06	7.16E-06	6.95E-06	6.53E-06	5.43E-06	3.68E-06
1	5.53E-06	8.15E-06	1.00E-05	1.20E-05	1.19E-05	9.38E-06	9.10E-06	8.55E-06	7.11E-06	4.82E-06
2	7.22E-06	1.07E-05	1.31E-05	1.57E-05	1.55E-05	1.23E-05	1.19E-05	1.12E-05	9.30E-06	6.31E-06
3	9.42E-06	1.39E-05	1.71E-05	2.05E-05	2.02E-05	1.60E-05	1.55E-05	1.46E-05	1.21E-05	8.23E-06
4	1.23E-05	1.81E-05	2.22E-05	2.67E-05	2.64E-05	2.08E-05	2.02E-05	1.90E-05	1.58E-05	1.07E-05
5	1.60E-05	2.35E-05	2.89E-05	3.47E-05	3.43E-05	2.71E-05	2.63E-05	2.47E-05	2.05E-05	1.39E-05
6	2.07E-05	3.06E-05	3.75E-05	4.50E-05	4.45E-05	3.52E-05	3.41E-05	3.21E-05	2.67E-05	1.81E-05
7	2.69E-05	3.96E-05	4.86E-05	5.84E-05	5.77E-05	4.56E-05	4.42E-05	4.16E-05	3.46E-05	2.34E-05
8	3.48E-05	5.13E-05	6.29E-05	7.56E-05	7.47E-05	5.90E-05	5.73E-05	5.38E-05	4.47E-05	3.03E-05
9	4.49E-05	6.63E-05	8.14E-05	9.77E-05	9.66E-05	7.63E-05	7.41E-05	6.96E-05	5.78E-05	3.92E-05
10	5.80E-05	8.56E-05	1.05E-04	1.26E-04	1.25E-04	9.85E-05	9.56E-05	8.98E-05	7.47E-05	5.07E-05
11	7.49E-05	1.10E-04	1.36E-04	1.63E-04	1.61E-04	1.27E-04	1.23E-04	1.16E-04	9.63E-05	6.53E-05
12	9.65E-05	1.42E-04	1.75E-04	2.10E-04	2.07E-04	1.64E-04	1.59E-04	1.49E-04	1.24E-04	8.42E-05
13	1.24E-04	1.83E-04	2.25E-04	2.70E-04	2.67E-04	2.11E-04	2.05E-04	1.92E-04	1.60E-04	1.08E-04
14	1.60E-04	2.36E-04	2.89E-04	3.47E-04	3.43E-04	2.71E-04	2.63E-04	2.47E-04	2.06E-04	1.39E-04
15	2.05E-04	3.03E-04	3.72E-04	4.46E-04	4.41E-04	3.49E-04	3.38E-04	3.18E-04	2.64E-04	1.79E-04
16	2.64E-04	3.89E-04	4.77E-04	5.73E-04	5.66E-04	4.48E-04	4.34E-04	4.08E-04	3.39E-04	2.30E-04
17	3.38E-04	4.99E-04	6.12E-04	7.36E-04	7.27E-04	5.74E-04	5.57E-04	5.24E-04	4.35E-04	2.95E-04
18	4.34E-04	6.40E-04	7.85E-04	9.43E-04	9.32E-04	7.37E-04	7.15E-04	6.72E-04	5.58E-04	3.79E-04
19	5.56E-04	8.20E-04	1.01E-03	1.21E-03	1.19E-03	9.44E-04	9.16E-04	8.61E-04	7.15E-04	4.85E-04
20	7.12E-04	1.05E-03	1.29E-03	1.55E-03	1.53E-03	1.21E-03	1.17E-03	1.10E-03	9.16E-04	6.21E-04
21	9.11E-04	1.34E-03	1.65E-03	1.98E-03	1.96E-03	1.55E-03	1.50E-03	1.41E-03	1.17E-03	7.95E-04
22	1.17E-03	1.72E-03	2.11E-03	2.53E-03	2.50E-03	1.98E-03	1.92E-03	1.80E-03	1.50E-03	1.02E-03
23	1.49E-03	2.20E-03	2.70E-03	3.24E-03	3.20E-03	2.53E-03	2.45E-03	2.31E-03	1.92E-03	1.30E-03
24	1.90E-03	2.81E-03	3.44E-03	4.14E-03	4.09E-03	3.23E-03	3.14E-03	2.95E-03	2.45E-03	1.66E-03
25	2.43E-03	3.58E-03	4.40E-03	5.28E-03	5.22E-03	4.13E-03	4.00E-03	3.76E-03	3.13E-03	2.12E-03
26	3.10E-03	4.57E-03	5.61E-03	6.74E-03	6.66E-03	5.27E-03	5.11E-03	4.80E-03	3.99E-03	2.71E-03
27	3.96E-03	5.84E-03	7.16E-03	8.60E-03	8.50E-03	6.72E-03	6.52E-03	6.12E-03	5.09E-03	3.45E-03
28	5.05E-03	7.44E-03	9.13E-03	1.10E-02	1.08E-02	8.57E-03	8.31E-03	7.81E-03	6.49E-03	4.40E-03
29	6.43E-03	9.48E-03	1.16E-02	1.40E-02	1.38E-02	1.09E-02	1.06E-02	9.96E-03	8.28E-03	5.61E-03
30	7.84E-03	1.16E-02	1.42E-02	1.70E-02	1.68E-02	1.33E-02	1.29E-02	1.21E-02	1.01E-02	6.84E-03
31	9.46E-03	1.39E-02	1.71E-02	2.06E-02	2.03E-02	1.61E-02	1.56E-02	1.46E-02	1.22E-02	8.25E-03

Table 10. ESA B Ion Fast Deflection Sweep Geometric Factors

Energy Step	<u>BIZ0</u>	<u>BIZ1</u>	<u>BIZ2</u>	<u>BIZ3</u>	<u>BIZ4</u>	<u>BIZ5</u>	<u>BIZ6</u>	<u>BIZ7</u>	<u>BIZ8</u>	<u>BIZ9</u>
0	4.14E-08	7.21E-08	8.31E-08	9.27E-08	9.37E-08	9.02E-08	8.55E-08	7.50E-08	6.06E-08	3.74E-08
1	5.24E-08	9.12E-08	1.05E-07	1.17E-07	1.18E-07	1.14E-07	1.08E-07	9.49E-08	7.67E-08	4.74E-08
2	6.62E-08	1.15E-07	1.33E-07	1.48E-07	1.50E-07	1.44E-07	1.37E-07	1.20E-07	9.70E-08	5.99E-08
3	8.38E-08	1.46E-07	1.68E-07	1.87E-07	1.89E-07	1.82E-07	1.73E-07	1.52E-07	1.23E-07	7.57E-08
4	1.06E-07	1.84E-07	2.13E-07	2.37E-07	2.39E-07	2.31E-07	2.19E-07	1.92E-07	1.55E-07	9.58E-08
5	1.34E-07	2.33E-07	2.69E-07	2.99E-07	3.03E-07	2.91E-07	2.76E-07	2.43E-07	1.96E-07	1.21E-07
6	1.69E-07	2.95E-07	3.39E-07	3.78E-07	3.83E-07	3.68E-07	3.49E-07	3.06E-07	2.48E-07	1.53E-07
7	2.14E-07	3.72E-07	4.29E-07	4.78E-07	4.83E-07	4.65E-07	4.41E-07	3.87E-07	3.13E-07	1.93E-07
8	2.70E-07	4.70E-07	5.42E-07	6.04E-07	6.10E-07	5.88E-07	5.58E-07	4.89E-07	3.95E-07	2.44E-07
9	3.41E-07	5.94E-07	6.84E-07	7.63E-07	7.71E-07	7.42E-07	7.04E-07	6.18E-07	4.99E-07	3.08E-07
10	4.30E-07	7.50E-07	8.64E-07	9.63E-07	9.74E-07	9.37E-07	8.89E-07	7.80E-07	6.30E-07	3.89E-07
11	5.43E-07	9.47E-07	1.09E-06	1.22E-06	1.23E-06	1.18E-06	1.12E-06	9.85E-07	7.96E-07	4.91E-07
12	6.86E-07	1.19E-06	1.38E-06	1.54E-06	1.55E-06	1.49E-06	1.42E-06	1.24E-06	1.00E-06	6.20E-07
13	8.66E-07	1.51E-06	1.74E-06	1.94E-06	1.96E-06	1.89E-06	1.79E-06	1.57E-06	1.27E-06	7.83E-07
14	1.09E-06	1.90E-06	2.19E-06	2.44E-06	2.47E-06	2.38E-06	2.26E-06	1.98E-06	1.60E-06	9.88E-07
15	1.38E-06	2.40E-06	2.77E-06	3.08E-06	3.12E-06	3.00E-06	2.85E-06	2.50E-06	2.02E-06	1.25E-06
16	1.74E-06	3.03E-06	3.49E-06	3.89E-06	3.93E-06	3.79E-06	3.59E-06	3.15E-06	2.55E-06	1.57E-06
17	2.19E-06	3.82E-06	4.40E-06	4.91E-06	4.96E-06	4.78E-06	4.53E-06	3.97E-06	3.21E-06	1.98E-06
18	2.77E-06	4.82E-06	5.55E-06	6.19E-06	6.26E-06	6.02E-06	5.71E-06	5.01E-06	4.05E-06	2.50E-06
19	3.49E-06	6.08E-06	7.00E-06	7.81E-06	7.89E-06	7.60E-06	7.21E-06	6.32E-06	5.11E-06	3.15E-06
20	4.40E-06	7.66E-06	8.83E-06	9.84E-06	9.95E-06	9.58E-06	9.09E-06	7.97E-06	6.44E-06	3.98E-06
21	5.54E-06	9.66E-06	1.11E-05	1.24E-05	1.25E-05	1.21E-05	1.15E-05	1.00E-05	8.12E-06	5.01E-06
22	6.99E-06	1.22E-05	1.40E-05	1.56E-05	1.58E-05	1.52E-05	1.44E-05	1.27E-05	1.02E-05	6.32E-06
23	8.81E-06	1.53E-05	1.77E-05	1.97E-05	1.99E-05	1.92E-05	1.82E-05	1.60E-05	1.29E-05	7.97E-06
24	1.11E-05	1.93E-05	2.23E-05	2.48E-05	2.51E-05	2.42E-05	2.29E-05	2.01E-05	1.63E-05	1.00E-05
25	1.40E-05	2.44E-05	2.81E-05	3.13E-05	3.16E-05	3.05E-05	2.89E-05	2.53E-05	2.05E-05	1.26E-05
26	1.76E-05	3.07E-05	3.54E-05	3.94E-05	3.99E-05	3.84E-05	3.64E-05	3.19E-05	2.58E-05	1.59E-05
27	2.22E-05	3.87E-05	4.46E-05	4.97E-05	5.02E-05	4.83E-05	4.59E-05	4.02E-05	3.25E-05	2.01E-05
28	2.80E-05	4.87E-05	5.61E-05	6.26E-05	6.32E-05	6.09E-05	5.78E-05	5.07E-05	4.09E-05	2.53E-05
29	3.52E-05	6.13E-05	7.07E-05	7.88E-05	7.96E-05	7.67E-05	7.27E-05	6.38E-05	5.16E-05	3.18E-05
30	4.38E-05	7.63E-05	8.80E-05	9.81E-05	9.91E-05	9.54E-05	9.05E-05	7.94E-05	6.42E-05	3.96E-05
31	5.39E-05	9.38E-05	1.08E-04	1.21E-04	1.22E-04	1.17E-04	1.11E-04	9.76E-05	7.89E-05	4.87E-05

Table 10. (cont'd) ESA B Ion Slow Deflection Sweep Geometric Factors

Energy Step	<u>BIZ0</u>	<u>BIZ1</u>	<u>BIZ2</u>	<u>BIZ3</u>	<u>BIZ4</u>	<u>BIZ5</u>	<u>BIZ6</u>	<u>BIZ7</u>	<u>BIZ8</u>	<u>BIZ9</u>
0	4.66E-08	8.11E-08	9.35E-08	1.04E-07	1.05E-07	1.01E-07	9.62E-08	8.44E-08	6.82E-08	4.21E-08
1	5.89E-08	1.03E-07	1.18E-07	1.32E-07	1.33E-07	1.28E-07	1.22E-07	1.07E-07	8.63E-08	5.33E-08
2	7.45E-08	1.30E-07	1.50E-07	1.67E-07	1.68E-07	1.62E-07	1.54E-07	1.35E-07	1.09E-07	6.74E-08
3	9.42E-08	1.64E-07	1.89E-07	2.11E-07	2.13E-07	2.05E-07	1.95E-07	1.71E-07	1.38E-07	8.52E-08
4	1.19E-07	2.07E-07	2.39E-07	2.66E-07	2.69E-07	2.59E-07	2.46E-07	2.16E-07	1.74E-07	1.08E-07
5	1.50E-07	2.62E-07	3.02E-07	3.37E-07	3.40E-07	3.28E-07	3.11E-07	2.73E-07	2.20E-07	1.36E-07
6	1.90E-07	3.31E-07	3.82E-07	4.25E-07	4.30E-07	4.14E-07	3.93E-07	3.44E-07	2.78E-07	1.72E-07
7	2.40E-07	4.18E-07	4.82E-07	5.37E-07	5.43E-07	5.23E-07	4.96E-07	4.35E-07	3.52E-07	2.17E-07
8	3.03E-07	5.28E-07	6.09E-07	6.79E-07	6.86E-07	6.60E-07	6.27E-07	5.50E-07	4.44E-07	2.74E-07
9	3.83E-07	6.67E-07	7.69E-07	8.57E-07	8.66E-07	8.34E-07	7.91E-07	6.94E-07	5.61E-07	3.46E-07
10	4.84E-07	8.42E-07	9.71E-07	1.08E-06	1.09E-06	1.05E-06	9.99E-07	8.76E-07	7.08E-07	4.37E-07
11	6.11E-07	1.06E-06	1.23E-06	1.37E-06	1.38E-06	1.33E-06	1.26E-06	1.11E-06	8.94E-07	5.52E-07
12	7.71E-07	1.34E-06	1.55E-06	1.72E-06	1.74E-06	1.68E-06	1.59E-06	1.40E-06	1.13E-06	6.97E-07
13	9.73E-07	1.69E-06	1.95E-06	2.18E-06	2.20E-06	2.12E-06	2.01E-06	1.76E-06	1.42E-06	8.80E-07
14	1.23E-06	2.14E-06	2.46E-06	2.75E-06	2.78E-06	2.67E-06	2.54E-06	2.22E-06	1.80E-06	1.11E-06
15	1.55E-06	2.70E-06	3.11E-06	3.46E-06	3.50E-06	3.37E-06	3.20E-06	2.81E-06	2.27E-06	1.40E-06
16	1.95E-06	3.40E-06	3.92E-06	4.37E-06	4.42E-06	4.25E-06	4.03E-06	3.54E-06	2.86E-06	1.77E-06
17	2.46E-06	4.29E-06	4.94E-06	5.51E-06	5.57E-06	5.36E-06	5.09E-06	4.46E-06	3.61E-06	2.23E-06
18	3.11E-06	5.41E-06	6.23E-06	6.95E-06	7.03E-06	6.76E-06	6.42E-06	5.63E-06	4.55E-06	2.81E-06
19	3.92E-06	6.82E-06	7.86E-06	8.77E-06	8.86E-06	8.53E-06	8.09E-06	7.10E-06	5.74E-06	3.54E-06
20	4.94E-06	8.60E-06	9.91E-06	1.11E-05	1.12E-05	1.08E-05	1.02E-05	8.95E-06	7.23E-06	4.47E-06
21	6.23E-06	1.08E-05	1.25E-05	1.39E-05	1.41E-05	1.36E-05	1.29E-05	1.13E-05	9.12E-06	5.63E-06
22	7.85E-06	1.37E-05	1.57E-05	1.76E-05	1.77E-05	1.71E-05	1.62E-05	1.42E-05	1.15E-05	7.10E-06
23	9.89E-06	1.72E-05	1.98E-05	2.21E-05	2.24E-05	2.15E-05	2.04E-05	1.79E-05	1.45E-05	8.94E-06
24	1.25E-05	2.17E-05	2.50E-05	2.79E-05	2.82E-05	2.71E-05	2.57E-05	2.26E-05	1.82E-05	1.13E-05
25	1.57E-05	2.73E-05	3.15E-05	3.51E-05	3.55E-05	3.42E-05	3.24E-05	2.84E-05	2.30E-05	1.42E-05
26	1.98E-05	3.45E-05	3.97E-05	4.43E-05	4.47E-05	4.31E-05	4.09E-05	3.58E-05	2.90E-05	1.79E-05
27	2.49E-05	4.34E-05	5.00E-05	5.58E-05	5.64E-05	5.43E-05	5.15E-05	4.51E-05	3.65E-05	2.25E-05
28	3.14E-05	5.47E-05	6.30E-05	7.02E-05	7.10E-05	6.83E-05	6.48E-05	5.69E-05	4.59E-05	2.84E-05
29	3.95E-05	6.88E-05	7.93E-05	8.84E-05	8.94E-05	8.61E-05	8.16E-05	7.16E-05	5.79E-05	3.57E-05
30	4.86E-05	8.46E-05	9.75E-05	1.09E-04	1.10E-04	1.06E-04	1.00E-04	8.80E-05	7.11E-05	4.39E-05
31	5.97E-05	1.04E-04	1.20E-04	1.34E-04	1.35E-04	1.30E-04	1.23E-04	1.08E-04	8.74E-05	5.40E-05

azimuthal angle at the elevation angle where the count maximum occurred. Examples of the counts versus angle plots for these single angle scans are shown in Figures 54 and 55. The angles given are the angular position of the ESA in the calibration facility coordinate system. From these plots, the FWHM was determined for each zone. Since the ion beam spread is significantly less than the expected angular resolution of the ESA in both angles, this method is all that is required to determine the angular width. These values were then averaged across energy to provide the angular width for each zone. Also, averages were used instead of just using the one energy scan yielding G_p' , due to the accumulated position loss in the calibration tables after multiple scans had been run. The angular widths for the ion ESAs are given in Table 11. No significant variance was seen in the elevation angle averages across energy for either ESA. The azimuthal width of ESA B ion zones was less than predicted and less than the width of ESA A. However, the same general trend in azimuthal width versus zone number is seen in both ion ESAs.

Table 11. Angular Width of Ion ESA Zones Averaged Across Selected Energy Channels (degrees)

ESA Zone	Elevation (β)	Azimuth (α)
AIZ0	8.0	9.4
AIZ1	9.6	9.9
AIZ2	9.1	10.8
AIZ3	10.3	11.2
AIZ4	9.1	11.4
AIZ5	8.9	10.3
AIZ6	9.4	10.7
AIZ7	9.6	10.4
AIZ8	9.1	8.9
AIZ9	9.1	7.2
BIZ0	9.2	7.6
BIZ1	11.3	9.0
BIZ2	10.5	9.6
BIZ3	11.3	10.1
BIZ4	9.5	9.6
BIZ5	8.6	9.3
BIZ6	10.3	9.4
BIZ7	10.0	8.4
BIZ8	10.0	7.4
BIZ9	9.1	7.7

5. EFFECTS OF APERTURE AND ANODE SIZES ON DETECTION CAPABILITIES

Initial testing on the ESAs in flight configuration revealed an unacceptable noise level in some of the zones. One of the solutions to this noise problem was the replacement of some low current zener diodes that had been used to produce the 200 V potential difference between the MCPs and the anodes. These zener diodes were removed and replaced with pairs of 1N148 signal diodes operating in reverse bias. This resulted in operation in the microampere region as required and in a certain amount of noise reduction. Following the diode replacements, noise in the various detectors persisted. The final solution to the noise problem was a redesign of the anode layout to minimize field emission effects at the edges of the MCPs. See Table 12 for the as-flown anode sizes. The anode redesign was checked to ascertain whether the reduction in anode size would significantly alter the ESA geometric factors.

The commonly held view of channel electron multiplier operation has been that an electron multiplier operates linearly only if its output current is below or approximately at 10 percent of its total strip current.⁹ Assuming an average MCP bias current of 42.5 μ A, linear output of 0.1, and linear gain of 1×10^6 , and knowing that the MCP area is 9.5 cm², it is possible to obtain the estimated maximum available linear count rate over the area of each MCP, for an unapertured ESA, using Eq. (26). The estimated maximum linear flux per MCP is 2.792×10^6 counts/sec/cm². Given that the area of the anodes is significantly less than that of the MCPs, the estimated maximum linear count rate is reduced. This estimated maximum anode output linear count rate can be calculated for each ESA zone by multiplying each zone's anode area by 2.792×10^6 counts/sec/cm². Performing this calculation, one obtains the values listed in Table 13.

Table 12. ESA Anode Areas (cm²)

Zone	Ion Sensor	Electron Sensor
0	0.388	0.242
1	0.515	0.248
2	0.515	0.248
3	0.515	0.248
4	0.484	0.237
5	0.484	0.237
6	0.515	0.248
7	0.515	0.248
8	0.515	0.248
9	0.388	0.242

$$(I_{\text{Bias Ave}} * \Delta_{\text{Linear Output}}) / [(1.6022 \times 10^{-19}) * A_{\text{MCP}} * G_{\text{Linear}}] \quad (26)$$

Table 13. Estimated Maximum Linear Count Rate Output per Anode (counts/sec)

Zone	Ion Sensor	Electron Sensor
0	1.083×10^6	6.755×10^5
1	1.438×10^6	6.923×10^5
2	1.438×10^6	6.923×10^5
3	1.438×10^6	6.923×10^5
4	1.351×10^6	6.616×10^5
5	1.351×10^6	6.616×10^5
6	1.438×10^6	6.923×10^5
7	1.438×10^6	6.923×10^5
8	1.438×10^6	6.923×10^5
9	1.083×10^6	6.755×10^5

In addition to the anode area, the ground screens both on the outside of the ESA and in the detection assembly, and the aperture size must be taken into account when determining the upper limit on linear flux. As noted previously, the transmissibility of the external ground screen, τ_1 , is 90 percent and the detection assembly ground screen transmissibility, τ_2 , is 52 percent. Eq. (27) yields the estimated maximum linear flux measurable in each zone. Values obtained from Eq. (27) are listed in Table 14.

$$\left(\begin{array}{c} \text{Maximum Linear Flux} \\ \text{Measured per Zone} \end{array} \right) = \left(\begin{array}{c} \text{Maximum Linear Count Rate} \\ \text{at each Anode} \end{array} \right) / (\tau_1 * \tau_2 * \text{Aperture Area}) \quad (27)$$

Nominally, the linear counting threshold of the A111F preamplifier is approximately 3.3 MHz. However, the A111Fs used in SPREE cannot approach that level of input due to the reduction in gain set for them. For flight, the A111F gain settings were reduced to eliminate noise, making them the limiting element in the detection scheme. The maximum count rates for each of the 40 A111Fs flown in the ESAs are listed in Table 15. The percentages directly below each A111F threshold give the ratio of maximum A111F count rate to the maximum linear count rate output for the corresponding anode. Multiplying the percentages in Table 15 by the maximum linear flux in each zone from Table 14 yields the maximum linear flux measurable by the A111Fs in the SPREE ESAs. (See Table 16.)

Table 14. Estimated Maximum Linear Flux Measured per Zone (counts/sec/cm²)

Zone	Ion Sensor		Electron Sensor	
	ESA A	ESA B	ESA A	ESA B
	A ₁ area used	A ₃ area used	A ₂ area used	A ₄ area used
0	8.186 x 10 ⁸	1.178 x 10 ¹¹	1.149 x 10 ⁹	1.149 x 10 ¹¹
1	1.087 x 10 ⁹	1.564 x 10 ¹¹	1.177 x 10 ⁹	1.177 x 10 ¹¹
2	1.087 x 10 ⁹	1.564 x 10 ¹¹	1.177 x 10 ⁹	1.177 x 10 ¹¹
3	1.087 x 10 ⁹	1.564 x 10 ¹¹	1.177 x 10 ⁹	1.177 x 10 ¹¹
4	1.021 x 10 ⁹	1.469 x 10 ¹¹	1.125 x 10 ⁹	1.125 x 10 ¹¹
5	1.021 x 10 ⁹	1.469 x 10 ¹¹	1.125 x 10 ⁹	1.125 x 10 ¹¹
6	1.087 x 10 ⁹	1.564 x 10 ¹¹	1.177 x 10 ⁹	1.177 x 10 ¹¹
7	1.087 x 10 ⁹	1.564 x 10 ¹¹	1.177 x 10 ⁹	1.177 x 10 ¹¹
8	1.087 x 10 ⁹	1.564 x 10 ¹¹	1.177 x 10 ⁹	1.177 x 10 ¹¹
9	8.186 x 10 ⁸	1.178 x 10 ¹¹	1.149 x 10 ⁹	1.149 x 10 ¹¹

Table 15. Maximum A111F Count Rates (counts/sec)

Zone	ESA A		ESA B	
	Ion Sensor	Electron Sensor	Ion Sensor	Electron Sensor
0	5.37 x 10 ⁵ 50%	4.74 x 10 ⁵ 70%	5.12 x 10 ⁵ 47%	4.37 x 10 ⁵ 65%
1	5.24 x 10 ⁵ 36%	5.62 x 10 ⁵ 81%	5.12 x 10 ⁵ 36%	6.12 x 10 ⁵ 88%
2	5.24 x 10 ⁵ 36%	7.24 x 10 ⁵ 105%	5.37 x 10 ⁵ 37%	5.12 x 10 ⁵ 74%
3	5.62 x 10 ⁵ 39%	4.87 x 10 ⁵ 70%	5.12 x 10 ⁵ 36%	6.99 x 10 ⁵ 101%
4	5.12 x 10 ⁵ 38%	6.24 x 10 ⁵ 94%	5.24 x 10 ⁵ 39%	6.49 x 10 ⁵ 98%
5	5.37 x 10 ⁵ 40%	4.74 x 10 ⁵ 72%	4.99 x 10 ⁵ 37%	5.87 x 10 ⁵ 89%
6	6.74 x 10 ⁵ 47%	4.87 x 10 ⁵ 70%	4.99 x 10 ⁵ 35%	5.62 x 10 ⁵ 81%
7	5.99 x 10 ⁵ 42%	4.24 x 10 ⁵ 61%	5.12 x 10 ⁵ 36%	5.37 x 10 ⁵ 78%
8	5.12 x 10 ⁵ 36%	5.37 x 10 ⁵ 78%	5.37 x 10 ⁵ 37%	3.74 x 10 ⁵ 54%
9	4.37 x 10 ⁵ 40%	6.49 x 10 ⁵ 96%	5.12 x 10 ⁵ 47%	7.49 x 10 ⁵ 111%

Table 16. Estimated Maximum Detectable Linear Flux (counts/sec/cm²)

Zone	Ion Sensor		Electron Sensor	
	ESA A	ESA B	ESA A	ESA B
	A ₁ area used	A ₃ area used	A ₂ area used	A ₄ area used
0	4.093 x 10 ⁸	5.537 x 10 ¹⁰	8.084 x 10 ⁸	7.469 x 10 ¹⁰
1	3.913 x 10 ⁸	5.630 x 10 ¹⁰	9.534 x 10 ⁸	1.036 x 10 ¹¹
2	3.913 x 10 ⁸	5.787 x 10 ¹⁰	1.177 x 10 ⁹	8.710 x 10 ¹⁰
3	4.239 x 10 ⁸	7.531 x 10 ¹⁰	8.239 x 10 ⁸	1.177 x 10 ¹¹
4	3.880 x 10 ⁸	5.729 x 10 ¹⁰	1.056 x 10 ⁹	1.103 x 10 ¹¹
5	4.084 x 10 ⁸	5.435 x 10 ¹⁰	8.100 x 10 ⁸	1.001 x 10 ¹¹
6	5.109 x 10 ⁸	5.474 x 10 ¹⁰	8.239 x 10 ⁸	9.534 x 10 ¹⁰
7	4.565 x 10 ⁸	5.630 x 10 ¹⁰	7.180 x 10 ⁸	9.181 x 10 ¹⁰
8	3.913 x 10 ⁸	5.789 x 10 ¹⁰	9.181 x 10 ⁸	6.536 x 10 ¹⁰
9	3.274 x 10 ⁸	5.537 x 10 ¹⁰	1.103 x 10 ⁹	1.149 x 10 ¹¹

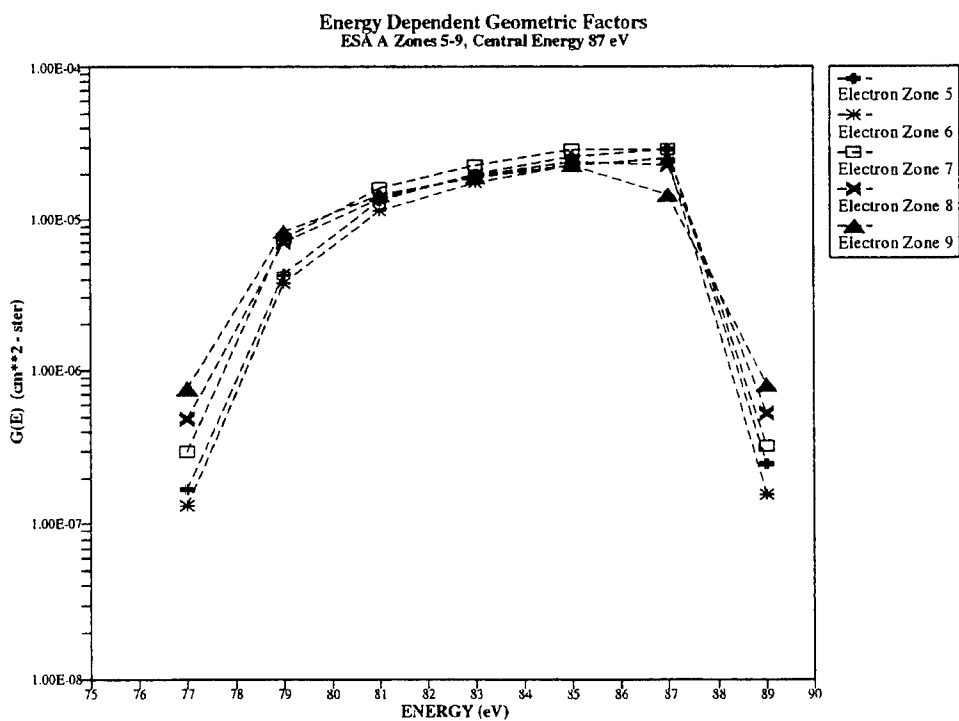
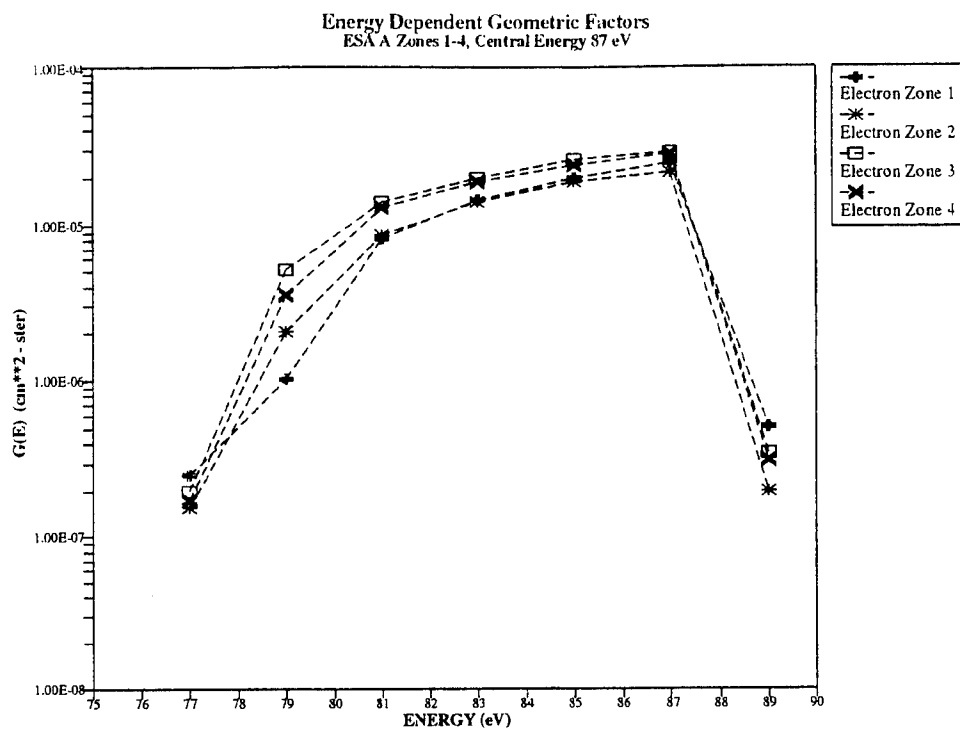


Figure 1. Electron Energy Dependent Geometric Factors for ESA A Zones 1-4 and 5-9 Plotted Versus Energy for the Channel With a Peak Response at Approximately 87 eV a) Zones 1-4; b) Zones 5-9

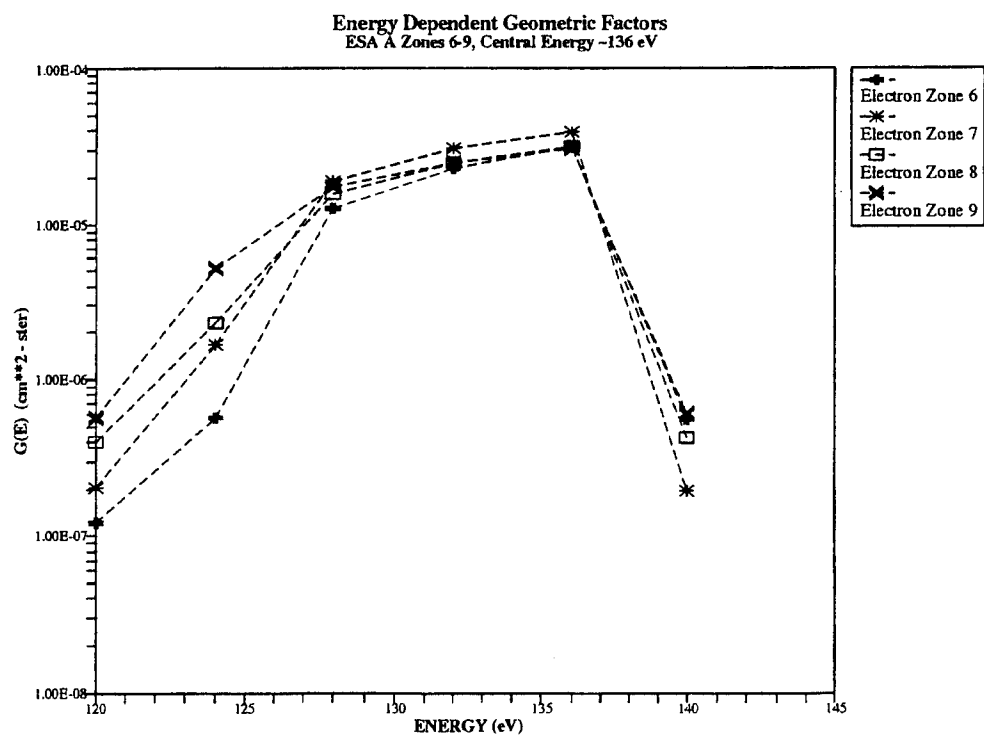
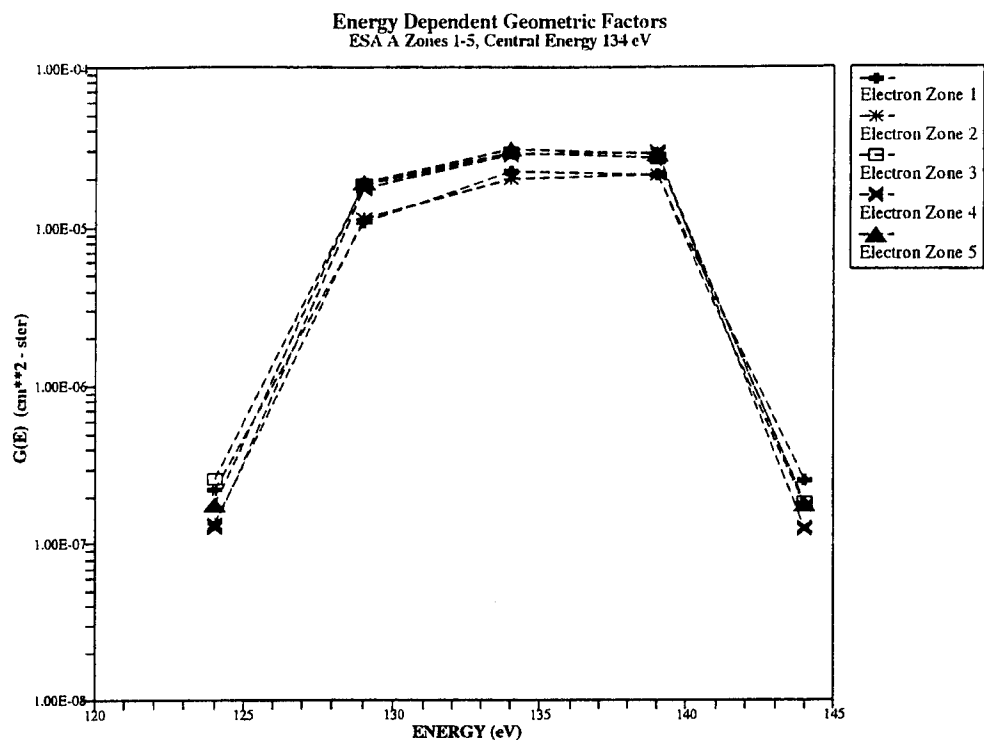


Figure 2. Electron Energy Dependent Geometric Factors for ESA A Zones 1-5 and 6-9 Plotted Versus Energy for the Channel With a Peak Response at Approximately 138 eV a) Zones 1-5; b) Zones 6-9

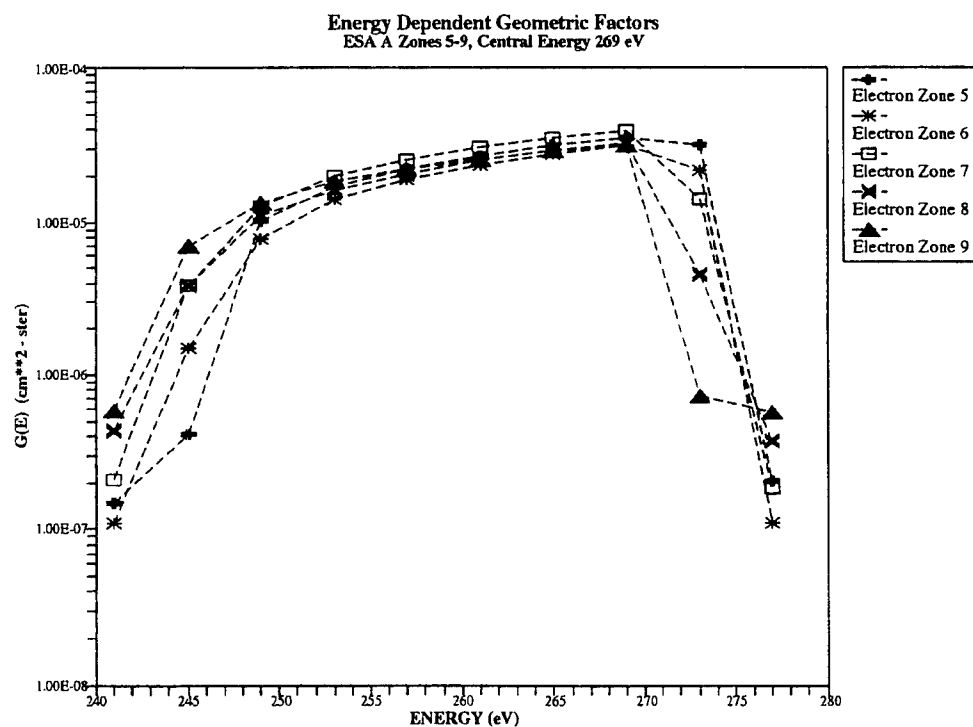
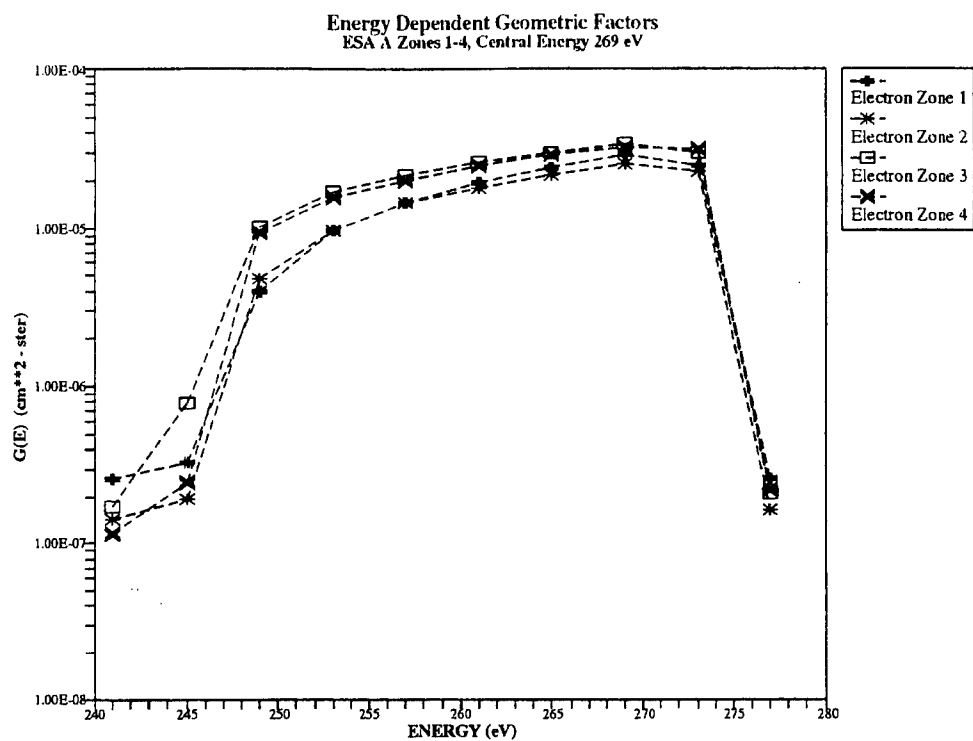


Figure 3. Electron Energy Dependent Geometric Factors for ESA A Zones 1-4 and 5-9 Plotted Versus Energy for the Channel With a Peak Response at Approximately 270 eV a) Zones 1-4; b) Zones 5-9

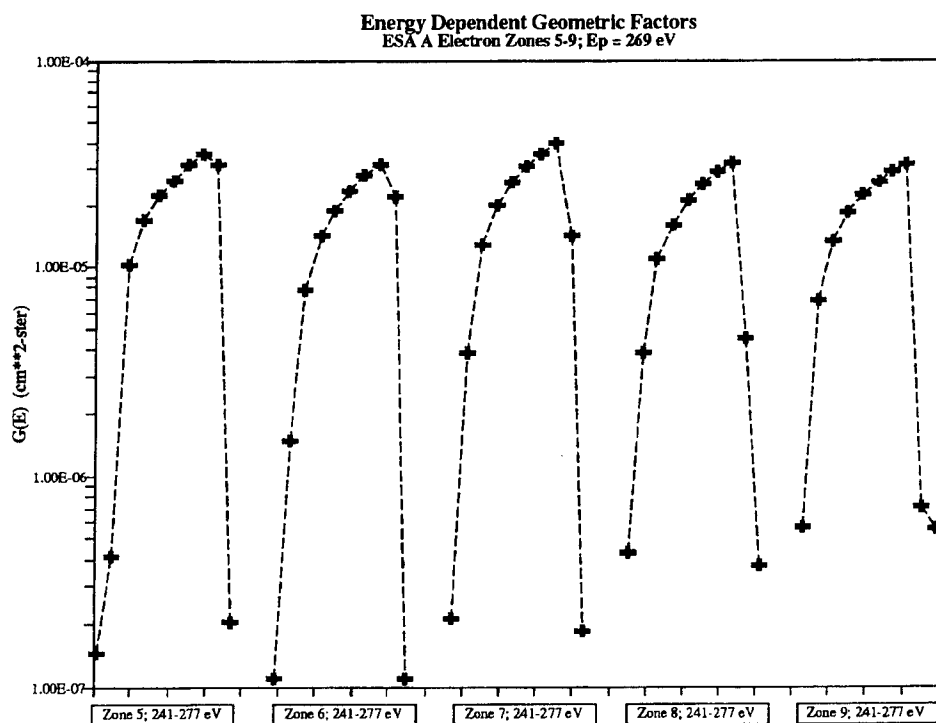
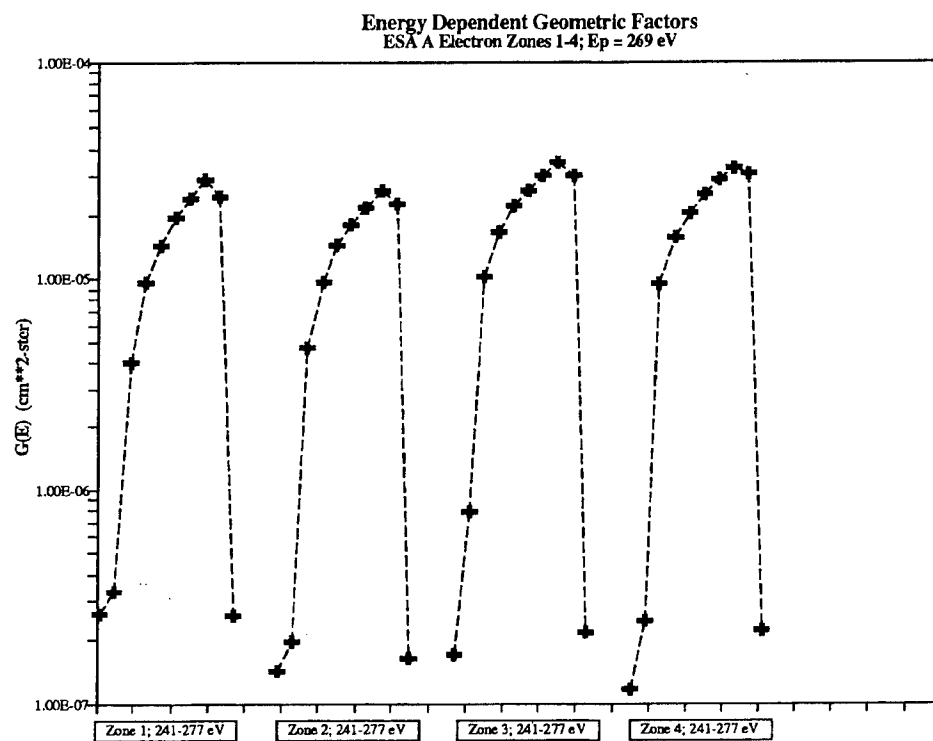


Figure 3. (cont.) Electron Energy Dependent Geometric Factors for ESA A Zones 1-4 and 5-9 Plotted Versus Energy for the Channel With a Peak Response at Approximately 270 eV c) Zones 1-4; d) Zones 5-9

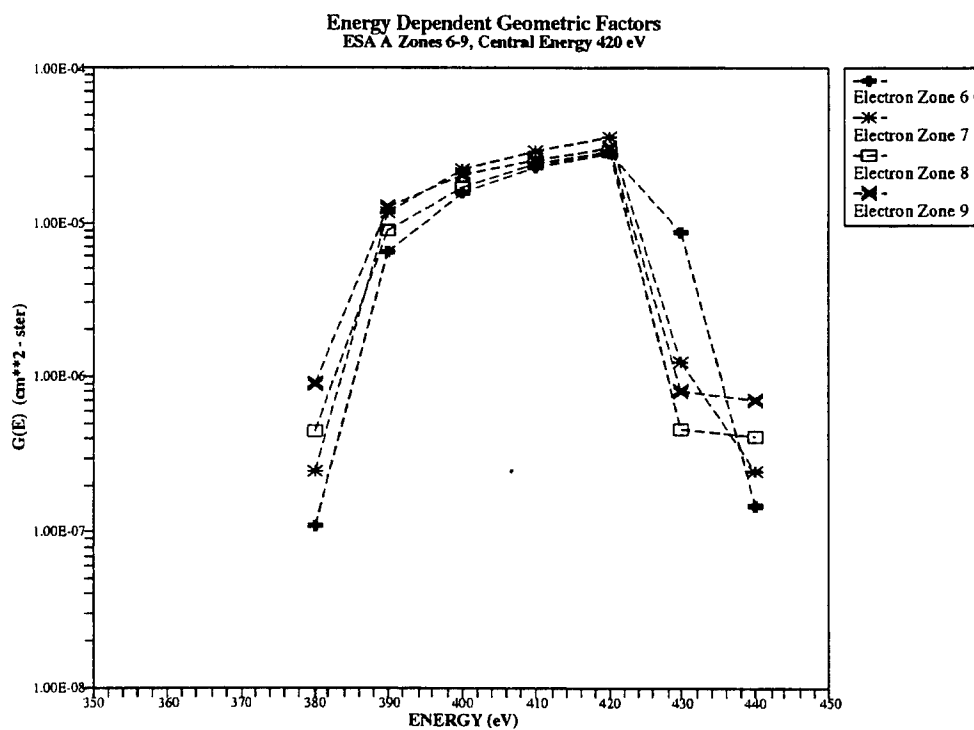
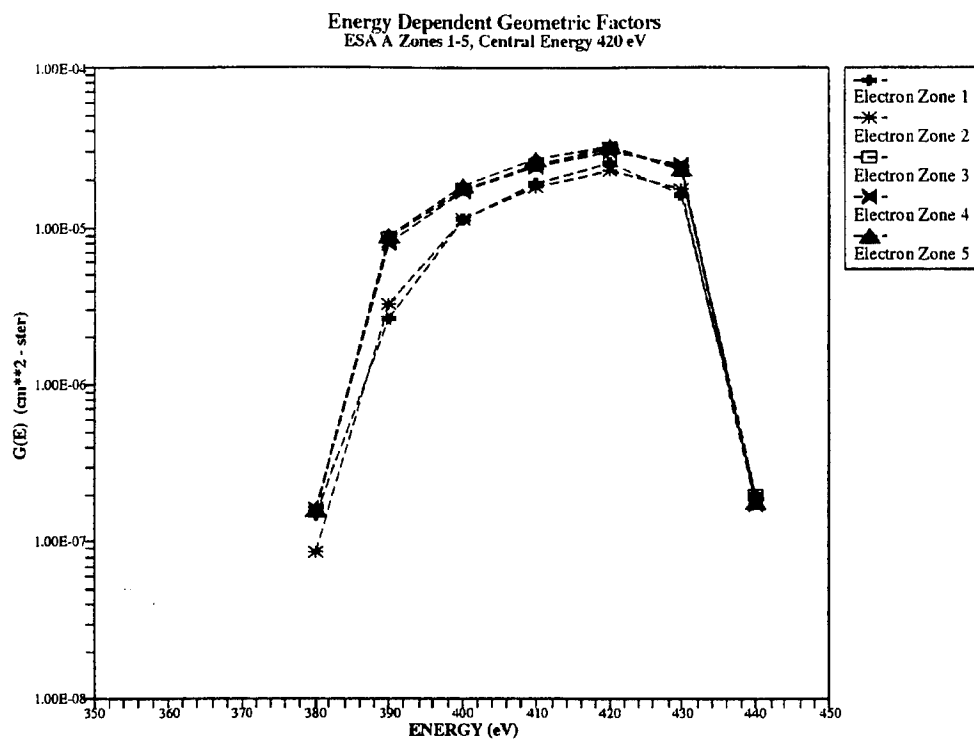


Figure 4. Electron Energy Dependent Geometric Factors for ESA A Zones 1-5 and 6-9 Plotted Versus Energy for the Channel With a Peak Response at Approximately 420 eV a) Zones 1-5; b) Zones 6-9

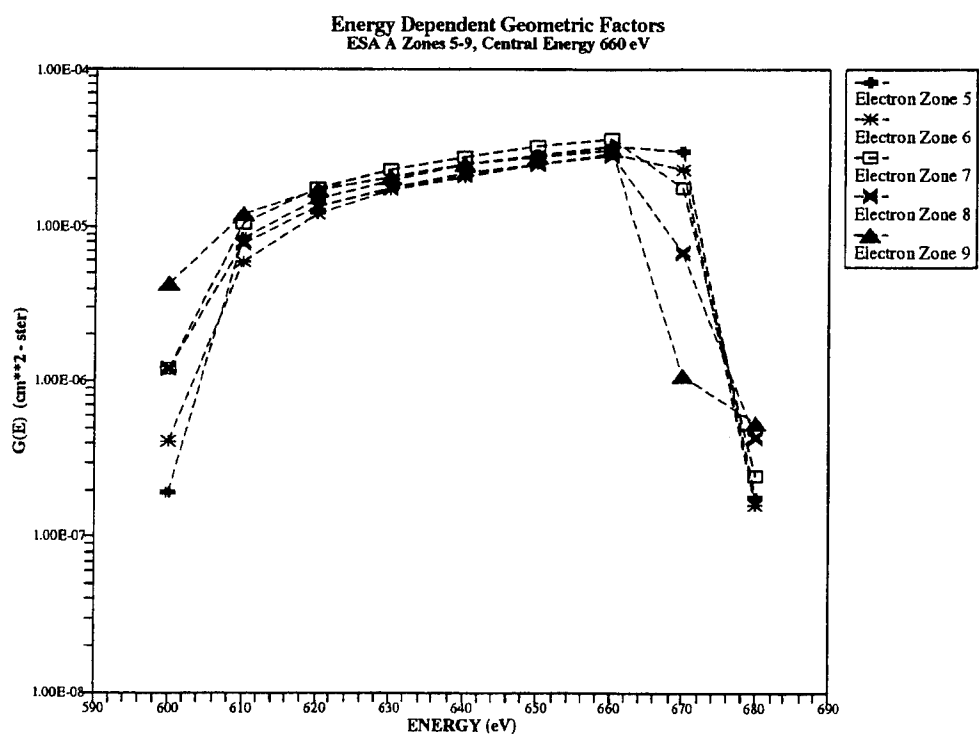
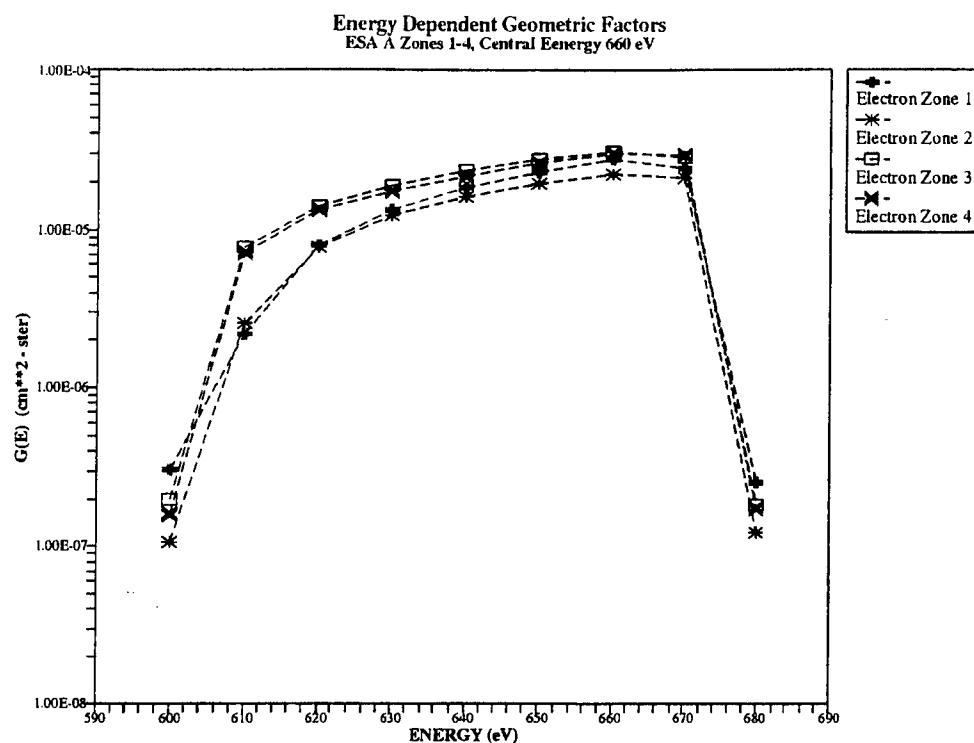


Figure 5. Electron Energy Dependent Geometric Factors for ESA A Zones 1-4 and 5-9 Plotted Versus Energy for the Channel With a Peak Response at Approximately 660 eV a) Zones 1-4; b) Zones 5-9

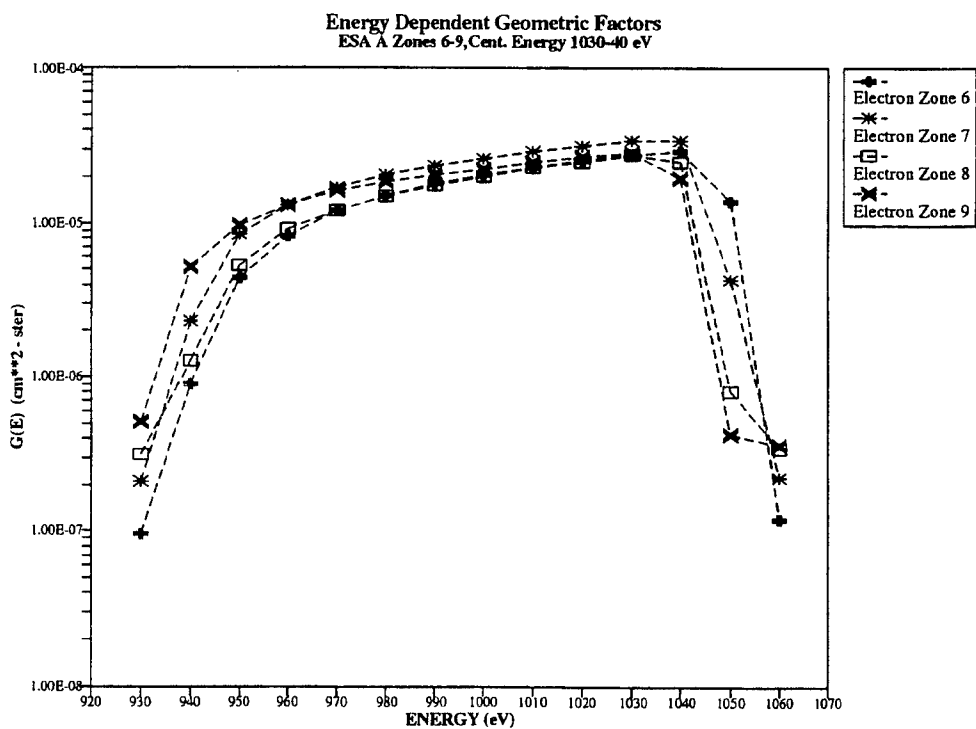
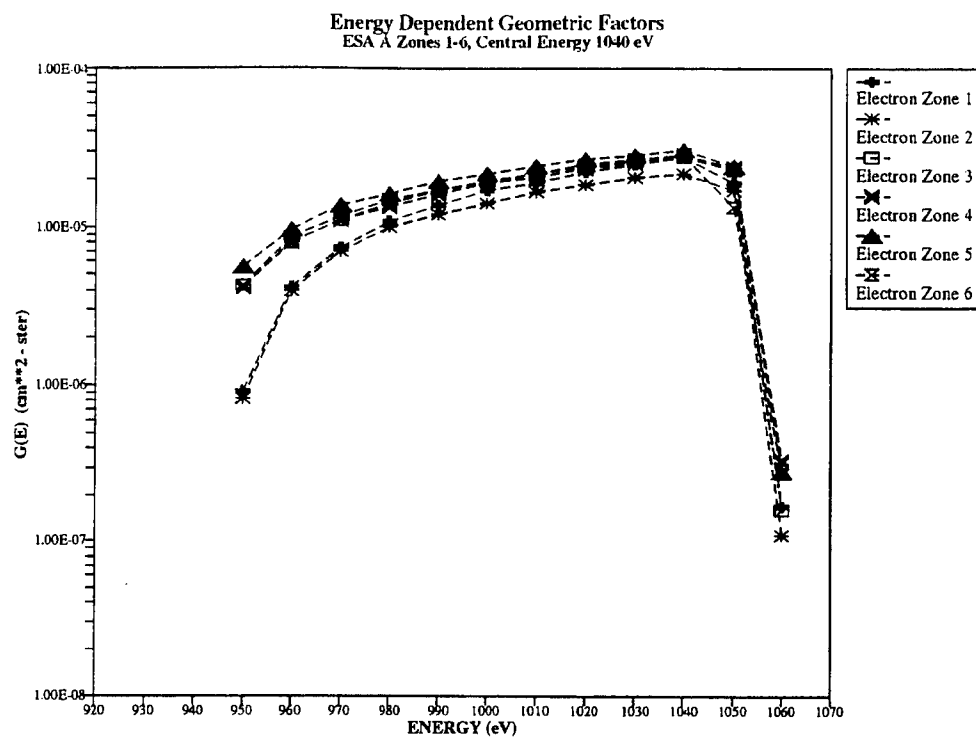


Figure 6. Electron Energy Dependent Geometric Factors for ESA A Zones 1-6 and 6-9 Plotted Versus Energy for the Channel With a Peak Response at Approximately 1040 eV a) Zones 1-6; b) Zones 6-9

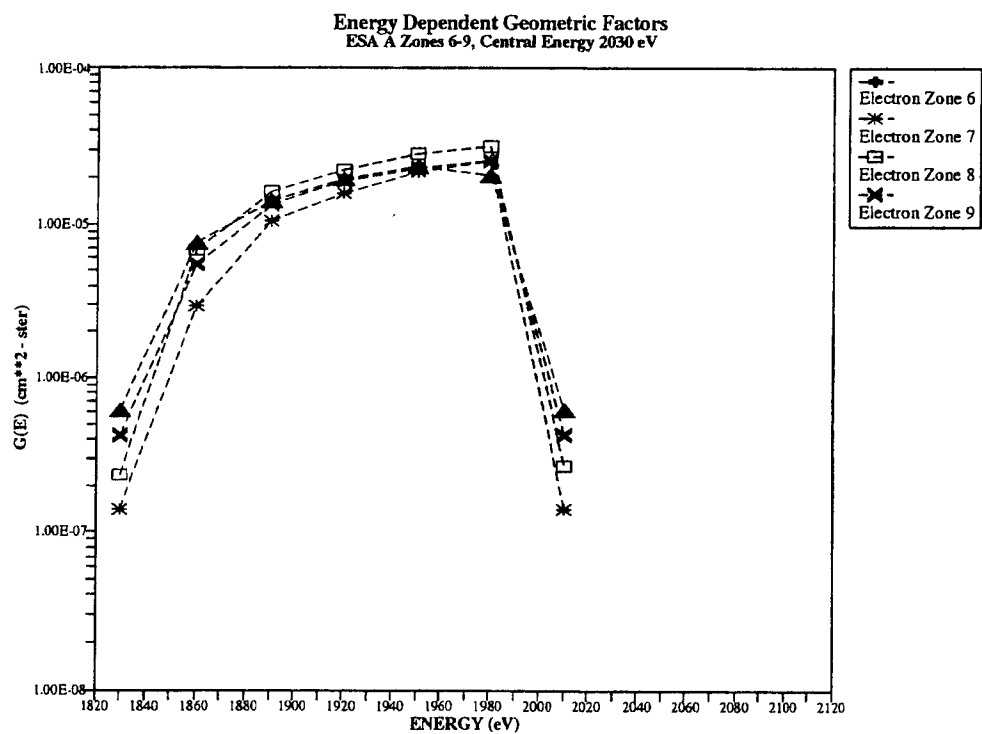
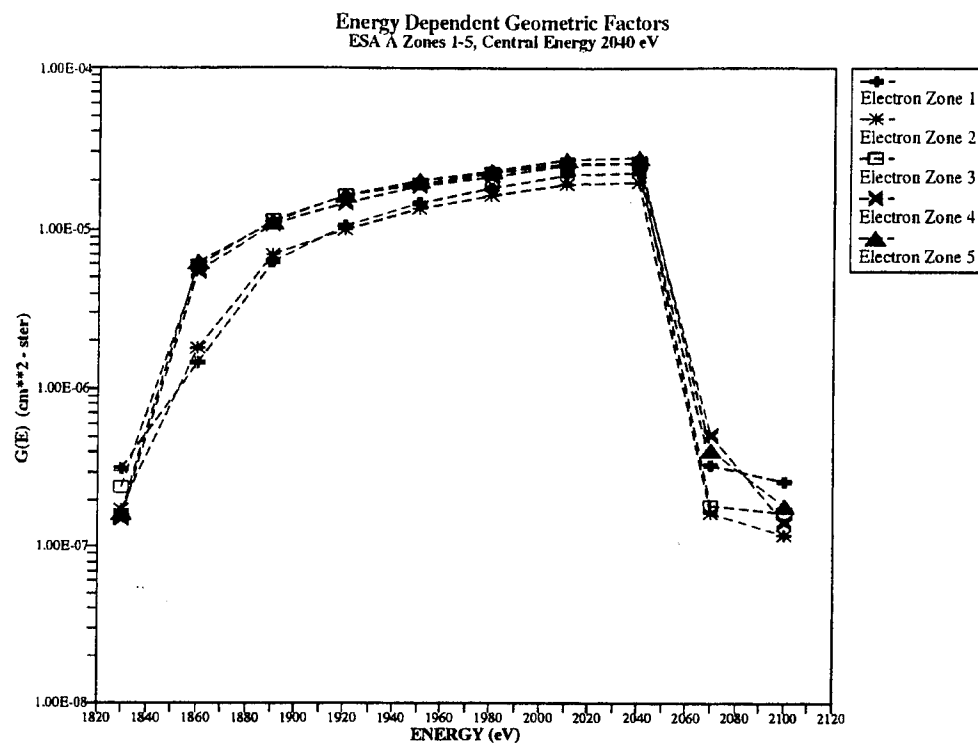


Figure 7. Electron Energy Dependent Geometric Factors for ESA A Zones 1-5 and 6-9 Plotted Versus Energy for the Channel With a Peak Response at Approximately 2040 eV a) Zones 1-5; b) Zones 6-9

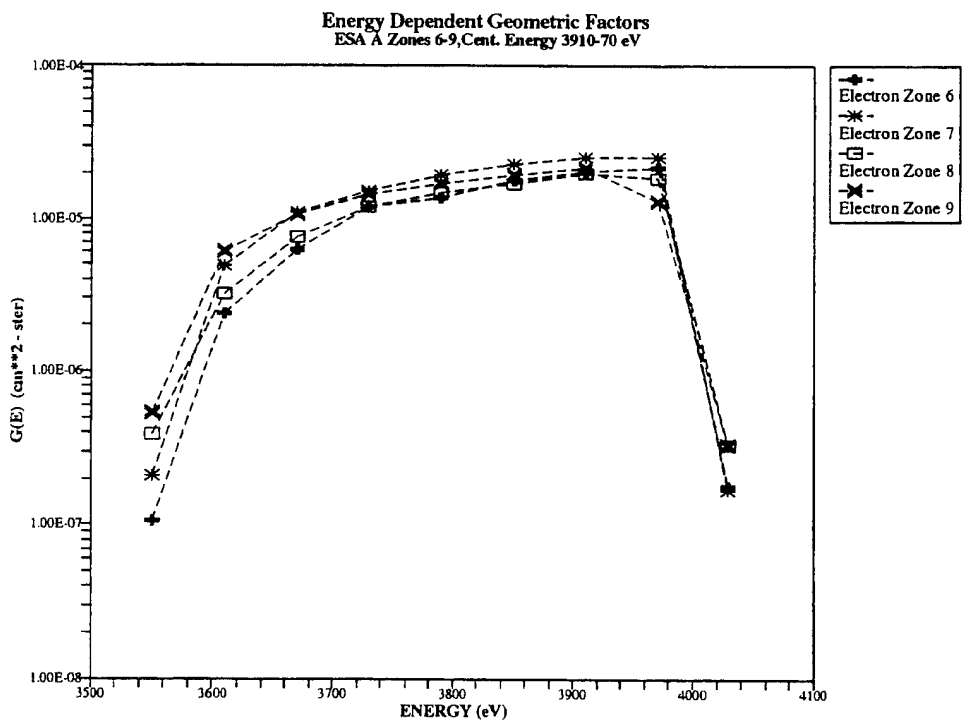
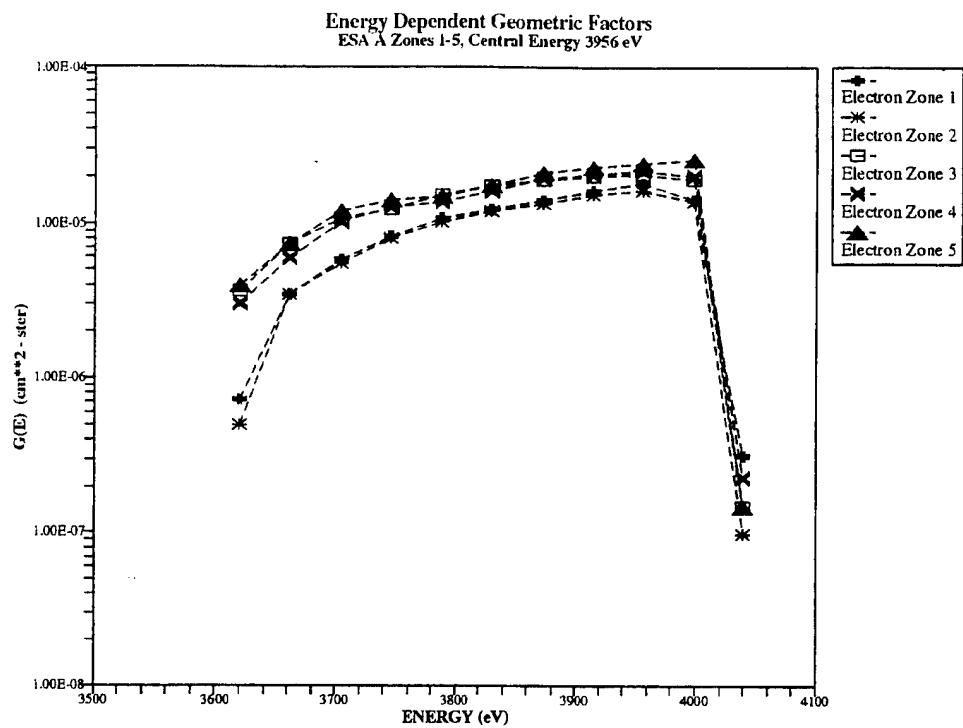


Figure 8. Electron Energy Dependent Geometric Factors for ESA A Zones 1-5 and 6-9 Plotted Versus Energy for the Channel With a Peak Response at Approximately 4000 eV a) Zones 1-5; b) Zones 6-9

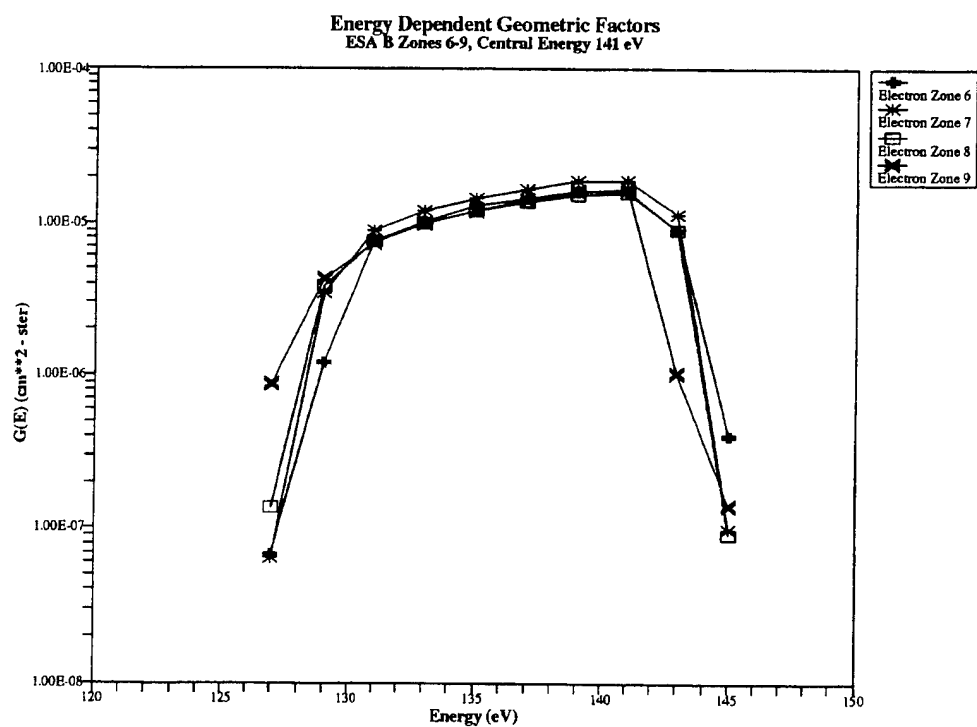
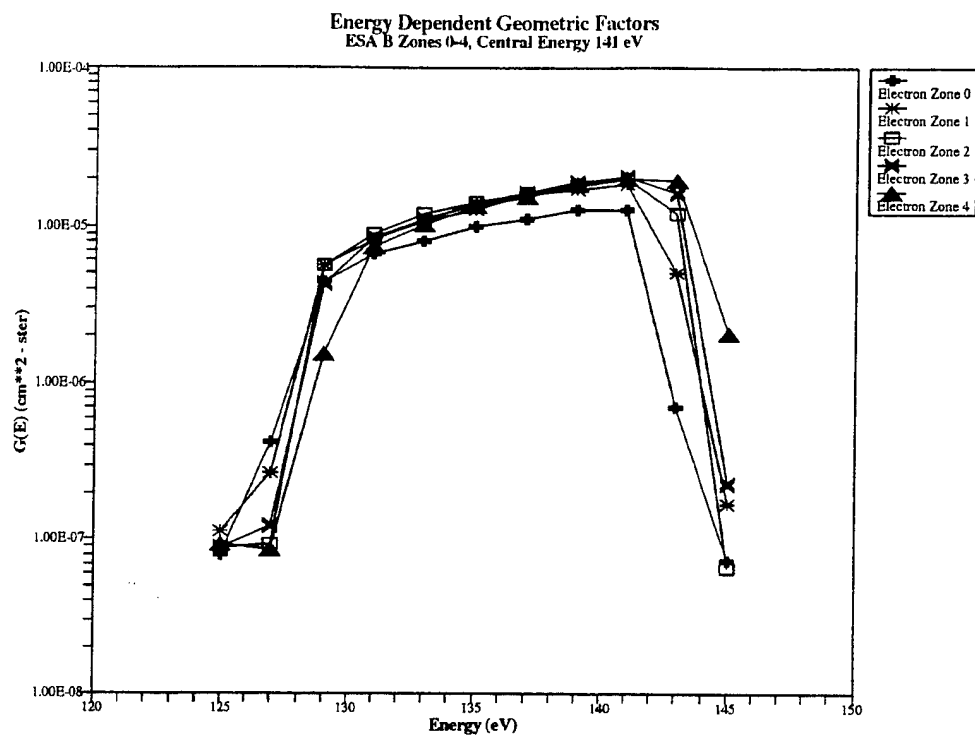


Figure 9. Electron Energy Dependent Geometric Factors for ESA B Zones 0-4 and 6-9 Plotted Versus Energy for the Channel With a Peak Response at 141 eV
a) Zones 0-4; b) Zones 6-9

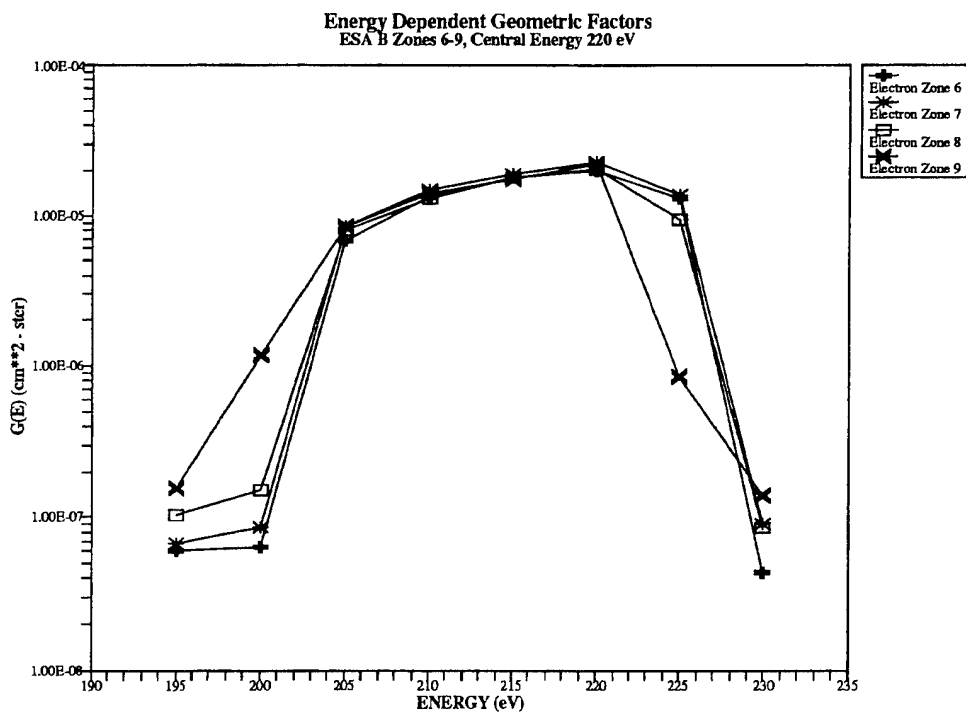
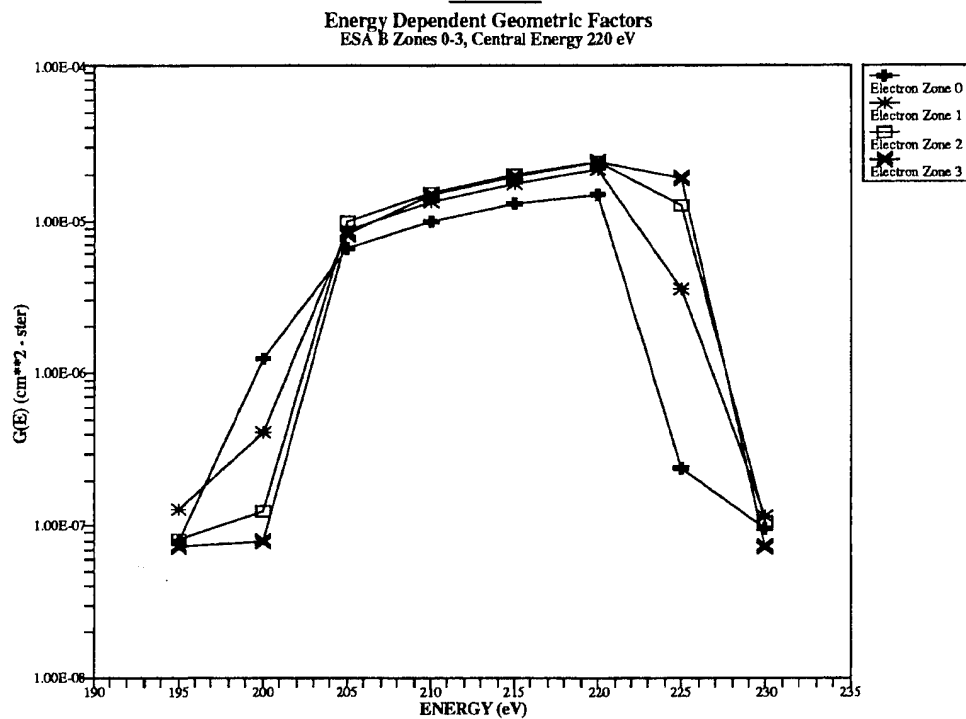


Figure 10. Electron Energy Dependent Geometric Factors for ESA B Zones 0-3 and 6-9
Plotted Versus Energy for the Channel With a Peak Response at 220 eV
a) Zones 0-3; b) Zones 6-9

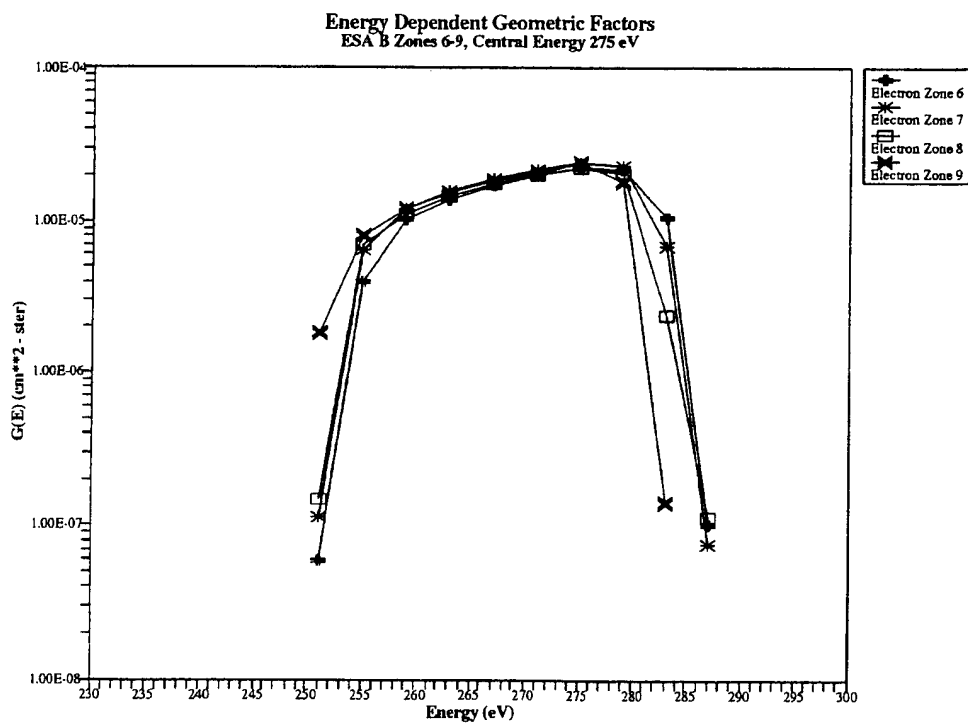
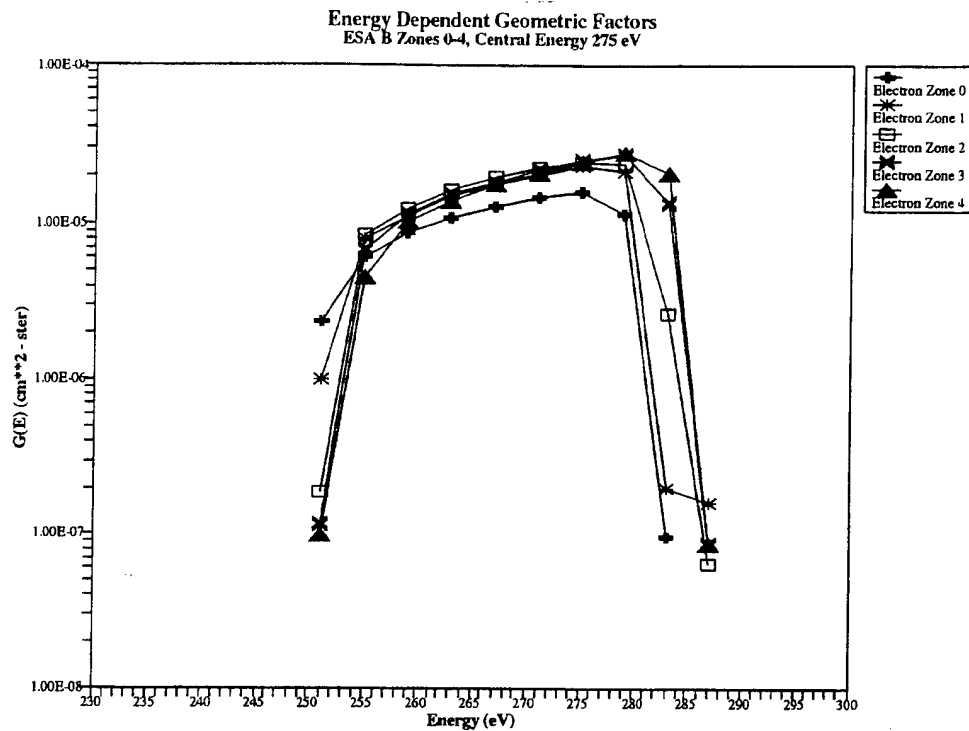


Figure 11. Electron Energy Dependent Geometric Factors for ESA B Zones 0-4 and 6-9
Plotted Versus Energy for the Channel With a Peak Response at 275 eV
a) Zones 0-4; b) Zones 6-9

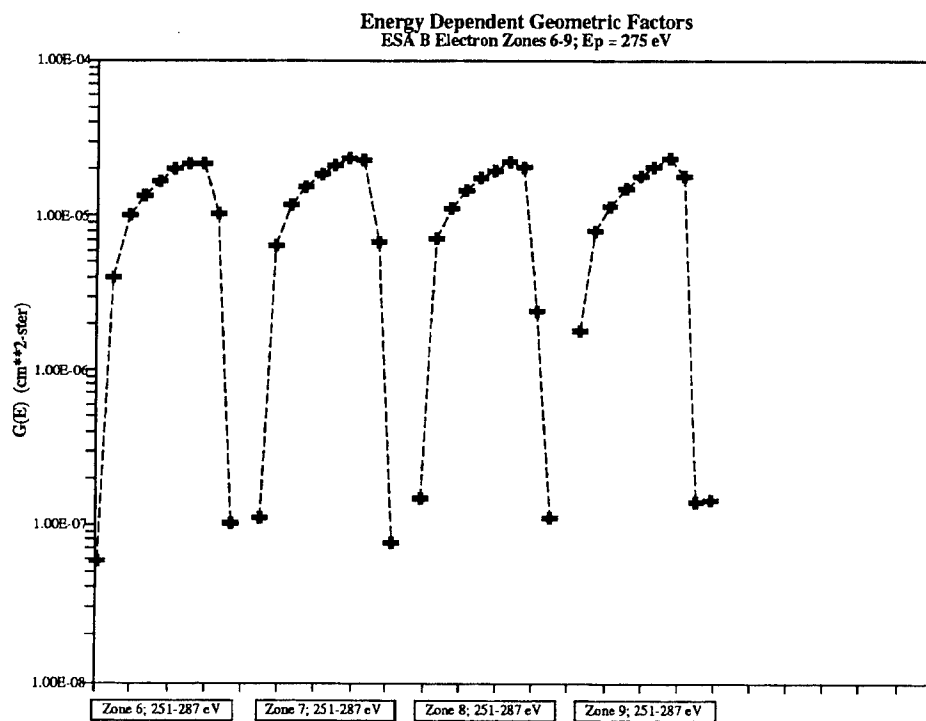
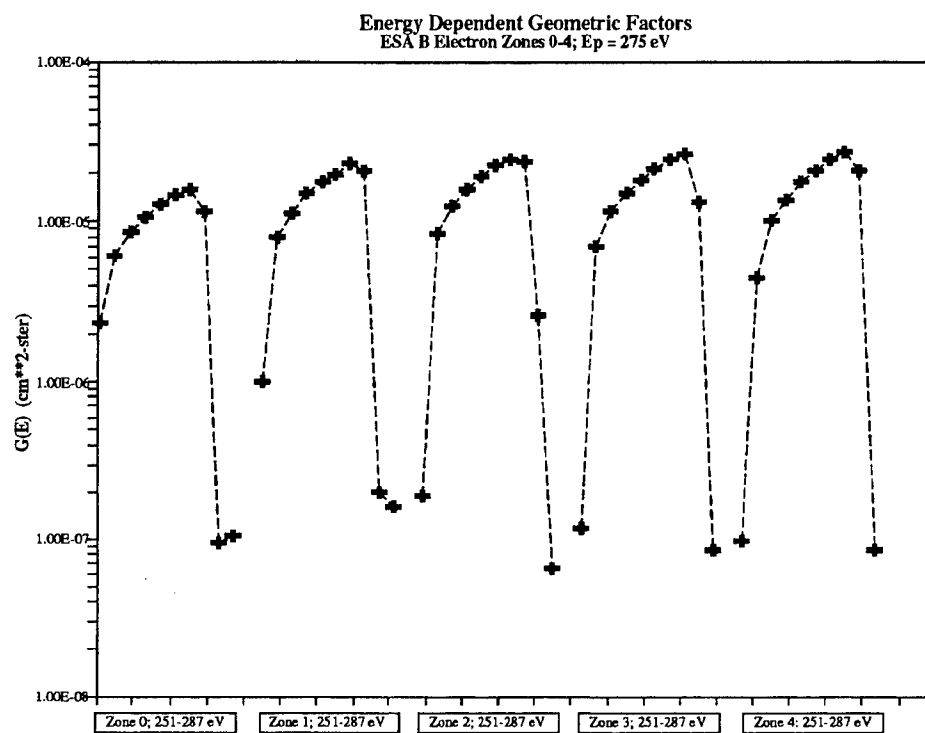


Figure 11. (cont.) Electron Energy Dependent Geometric Factors for ESA B Zones 0-4 and 6-9 Plotted Versus Energy for the Channel With a Peak Response at 275 eV c) Zones 0-4; d) Zones 6-9

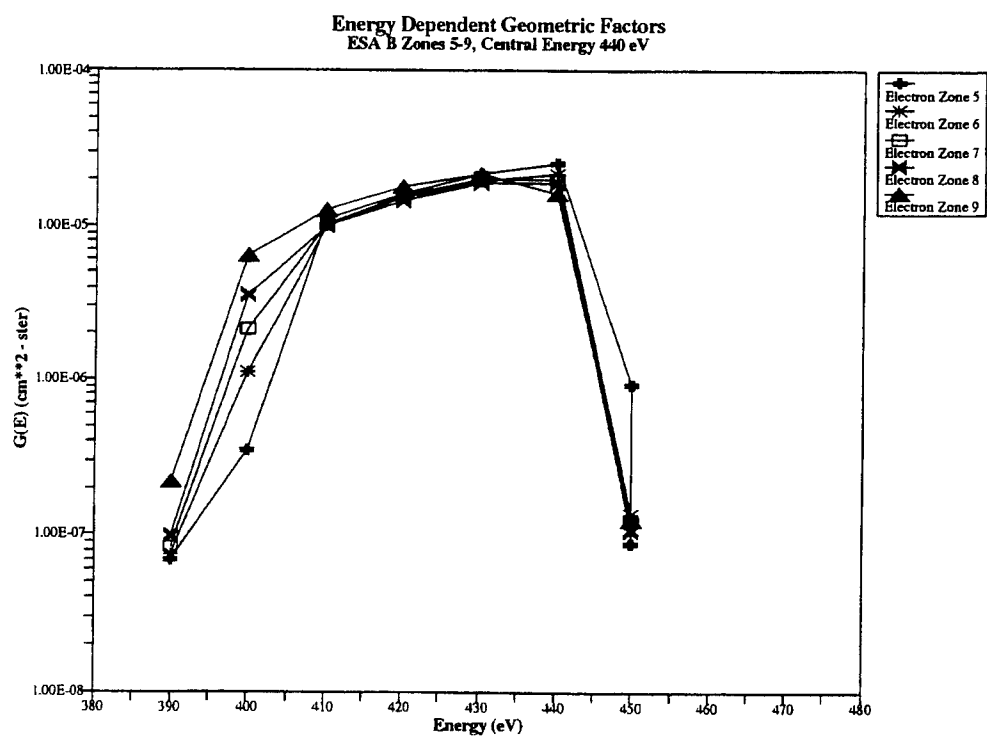
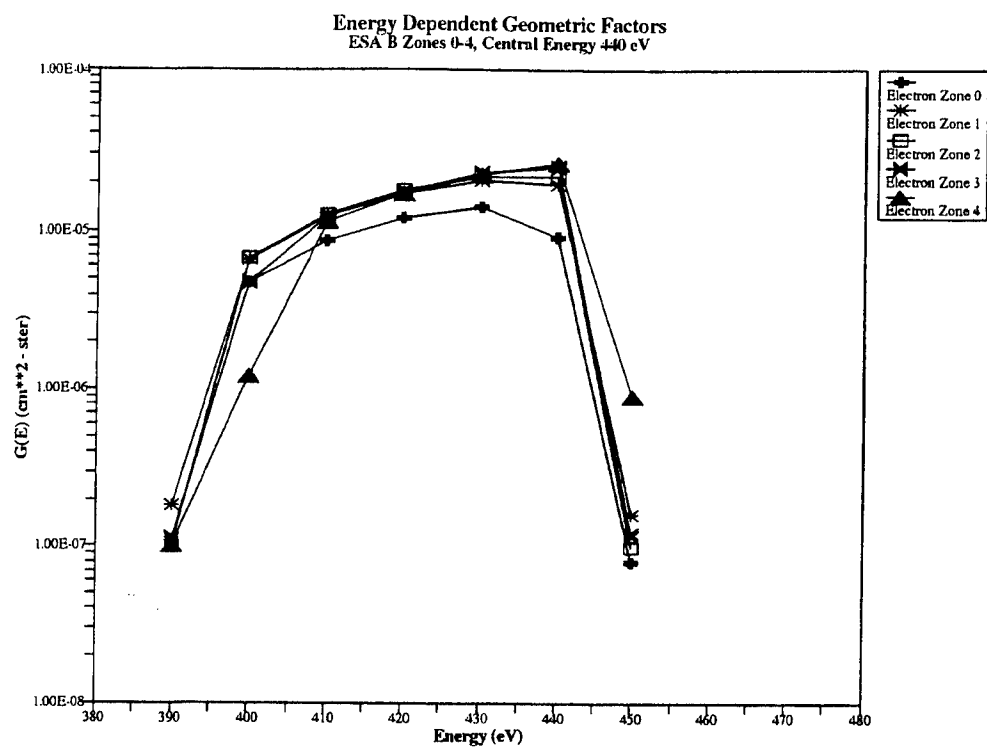


Figure 12. Electron Energy Dependent Geometric Factors for ESA B Zones 0-4 and 5-9 Plotted Versus Energy for the Channel With a Peak Response at 440 eV
a) Zones 0-4; b) Zones 5-9

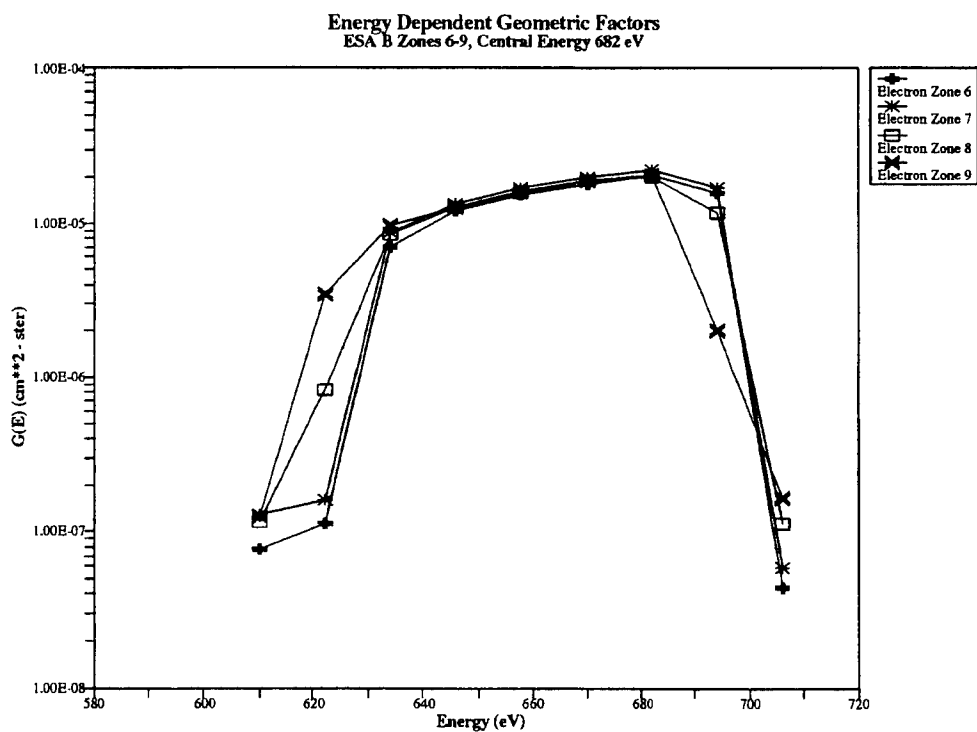
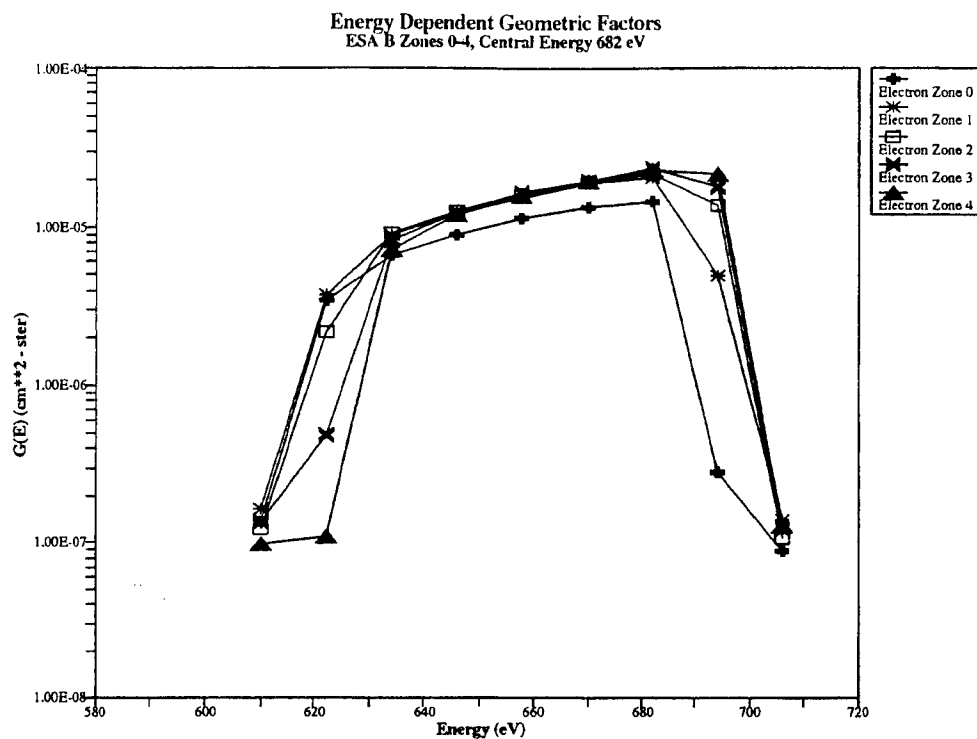


Figure 13. Electron Energy Dependent Geometric Factors for ESA B Zones 0-4 and 6-9 Plotted Versus Energy for the Channel With a Peak Response at 682 eV
a) Zones 0-4; b) Zones 6-9

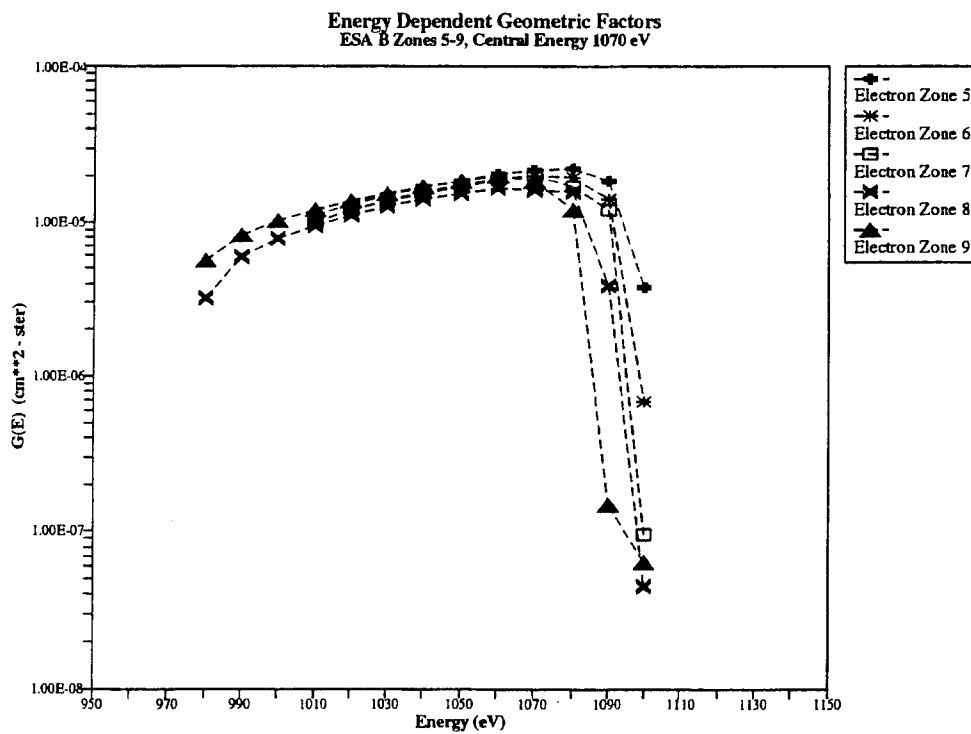
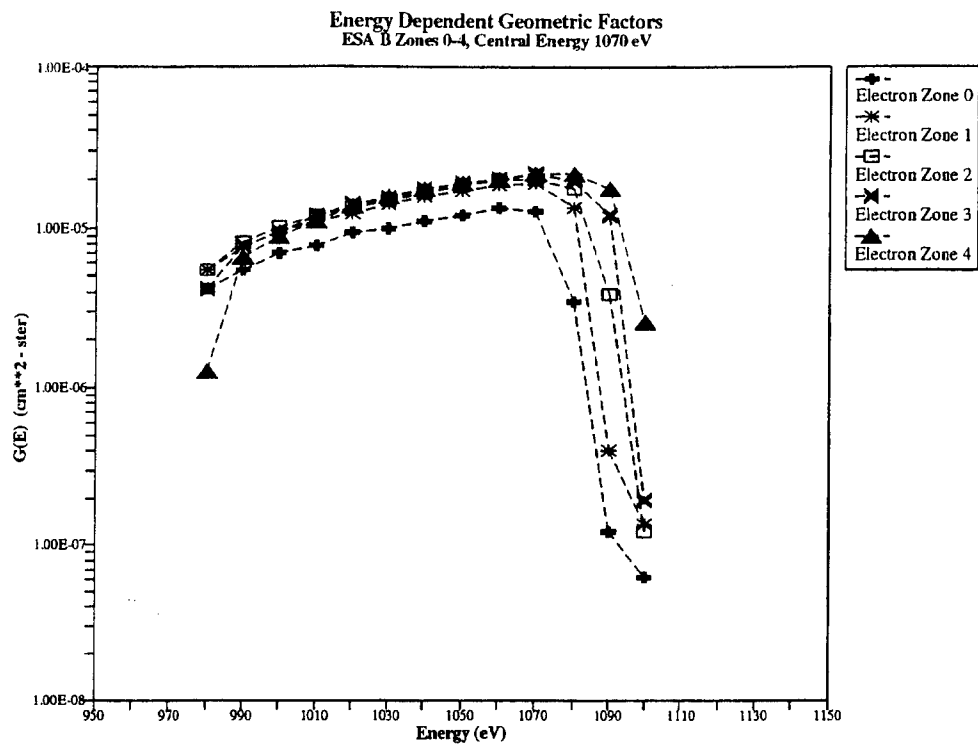


Figure 14. Electron Energy Dependent Geometric Factors for ESA B Zones 0-4 and 5-9
Plotted Versus Energy for the Channel With a Peak Response at 1070 eV
a) Zones 0-4; b) Zones 5-9

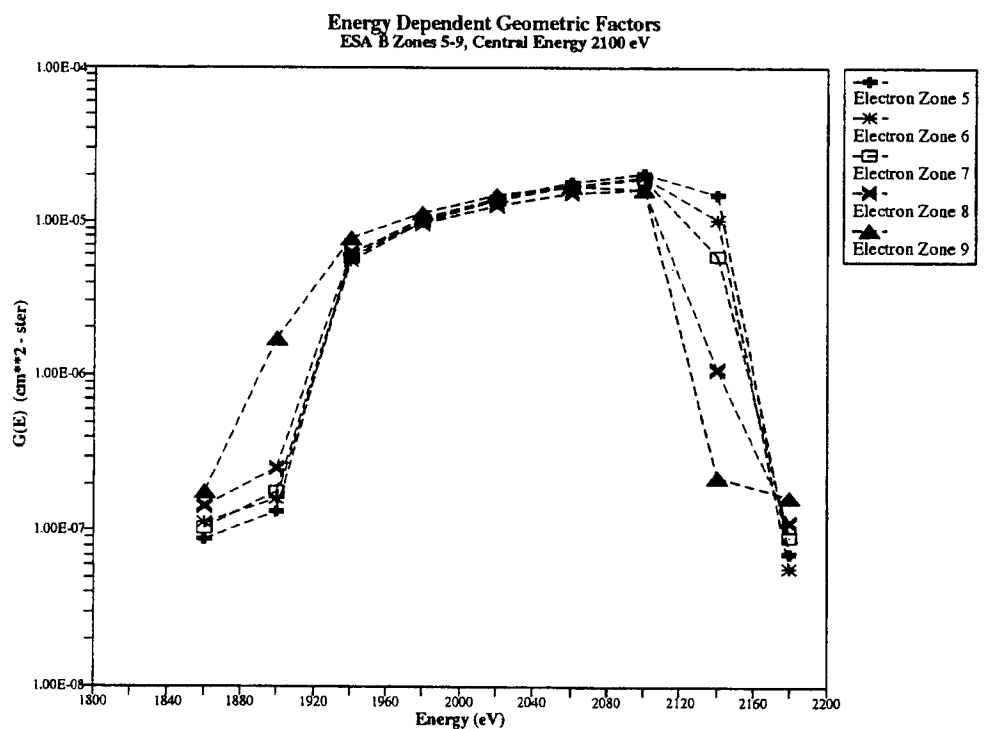
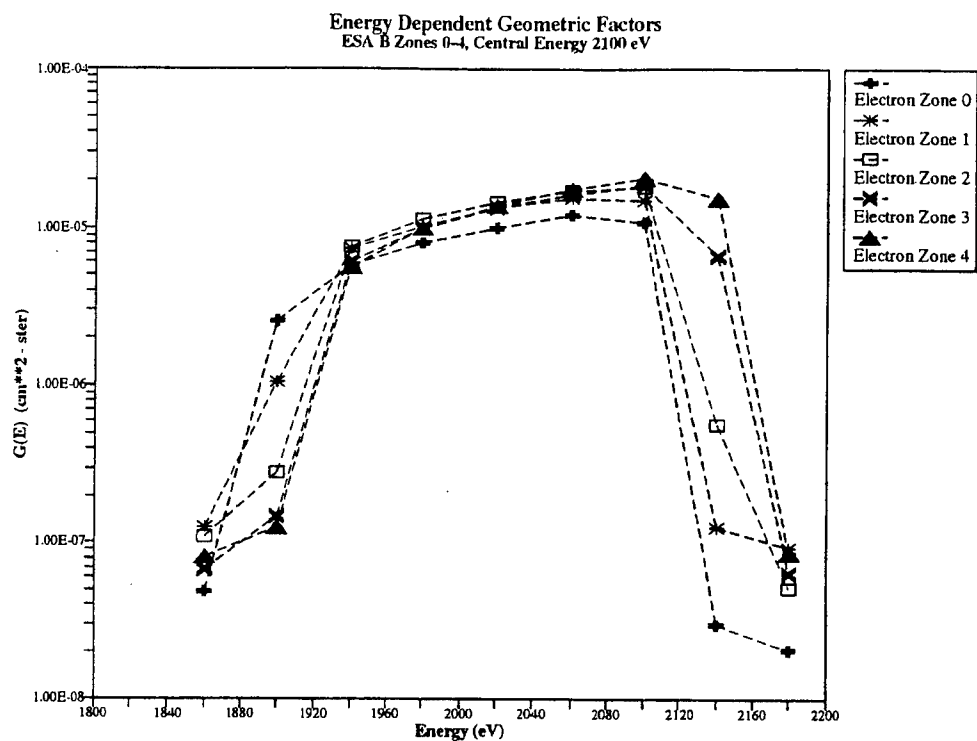


Figure 15. Electron Energy Dependent Geometric Factors for ESA B Zones 0-4 and 5-9
Plotted Versus Energy for the Channel With a Peak Response at 2100 eV
a) Zones 0-4; b) Zones 5-9

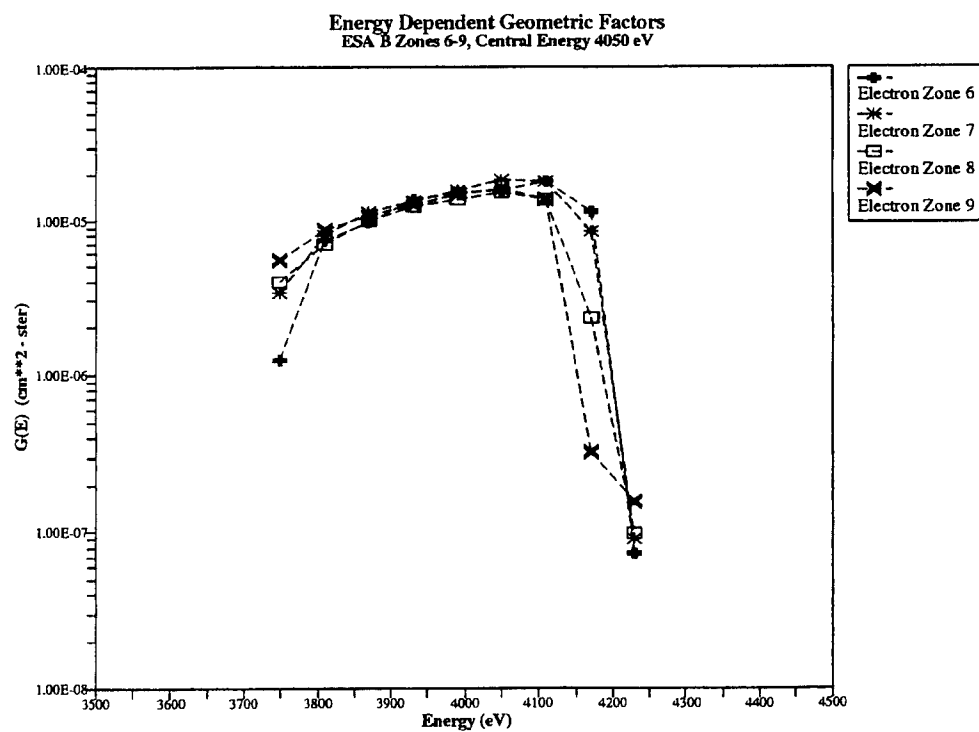
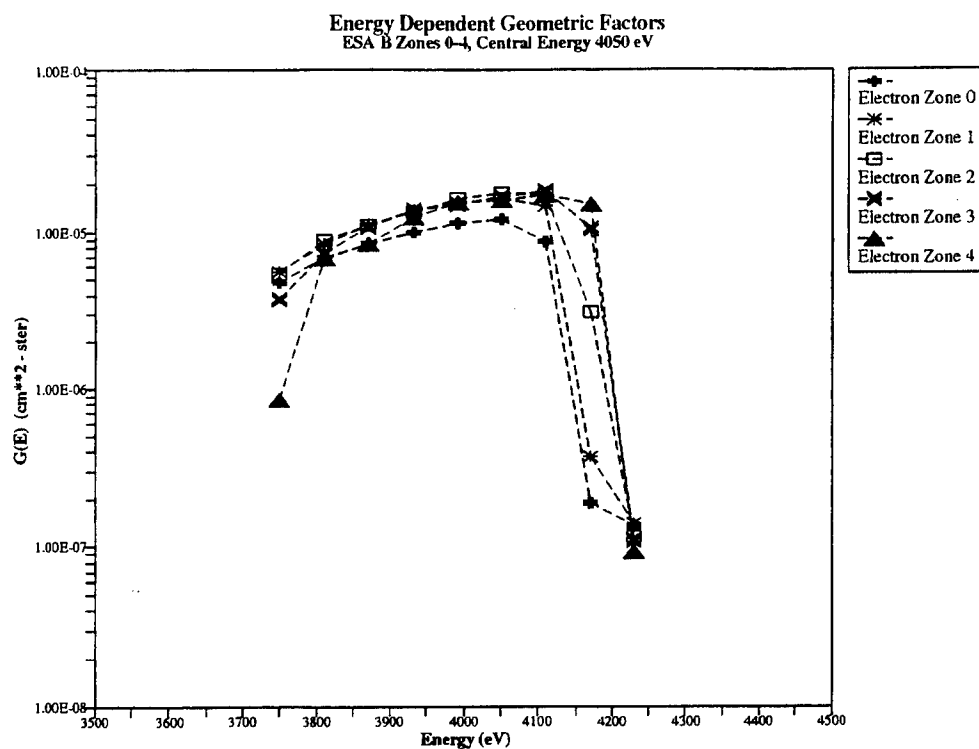


Figure 16. Electron Energy Dependent Geometric Factors for ESA B Zones 0-4 and 6-9
Plotted Versus Energy for the Channel With a Peak Response at 4050 eV
a) Zones 0-4; b) Zones 6-9

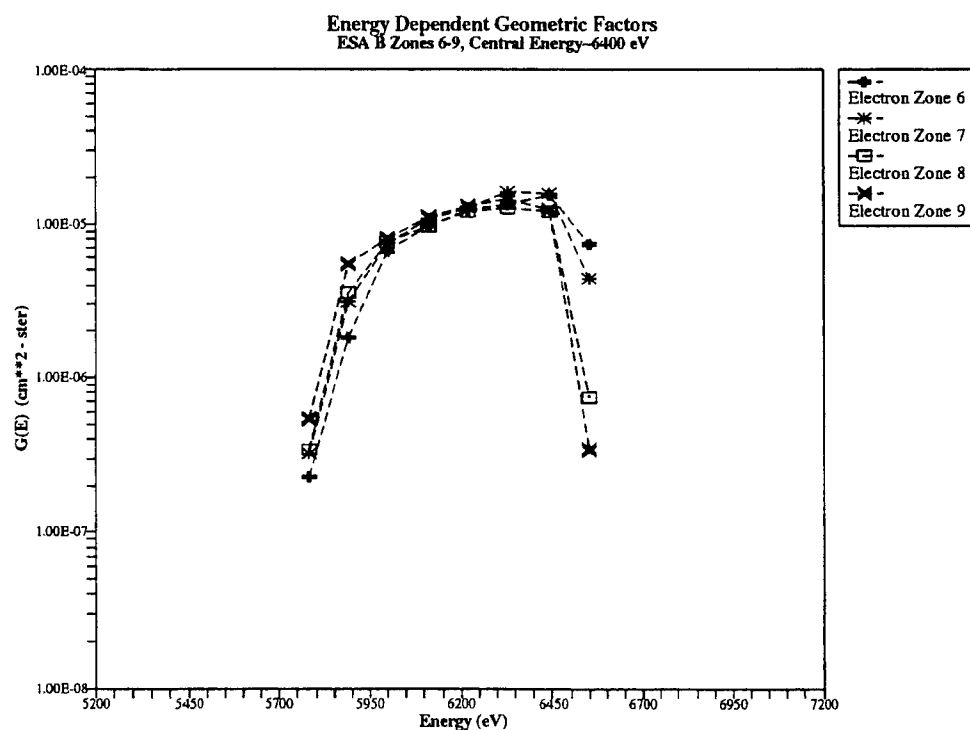
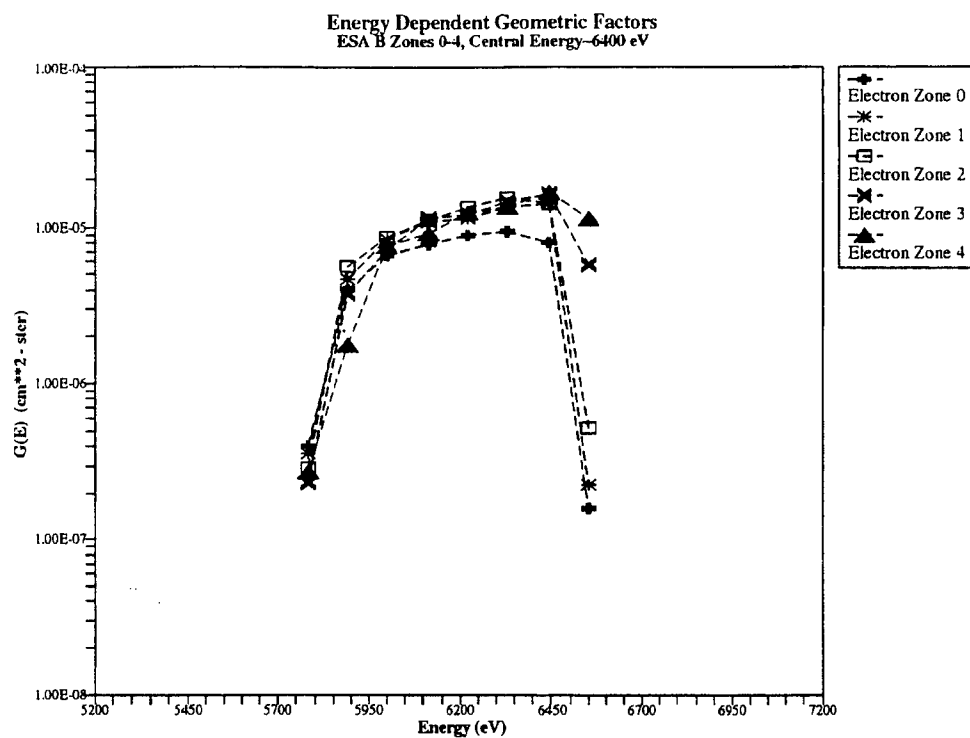


Figure 17. Electron Energy Dependent Geometric Factors for ESA B Zones 0-4 and 6-9 Plotted Versus Energy for the channel With a Peak Response at 6400 eV
a) Zones 0-4; b) Zones 6-9

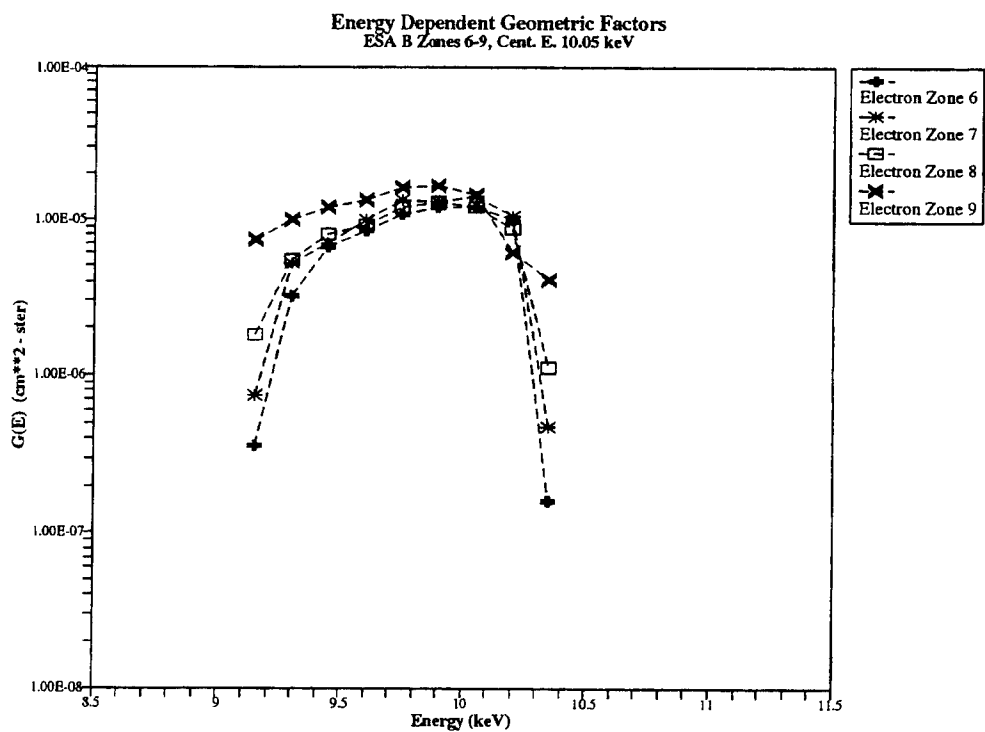
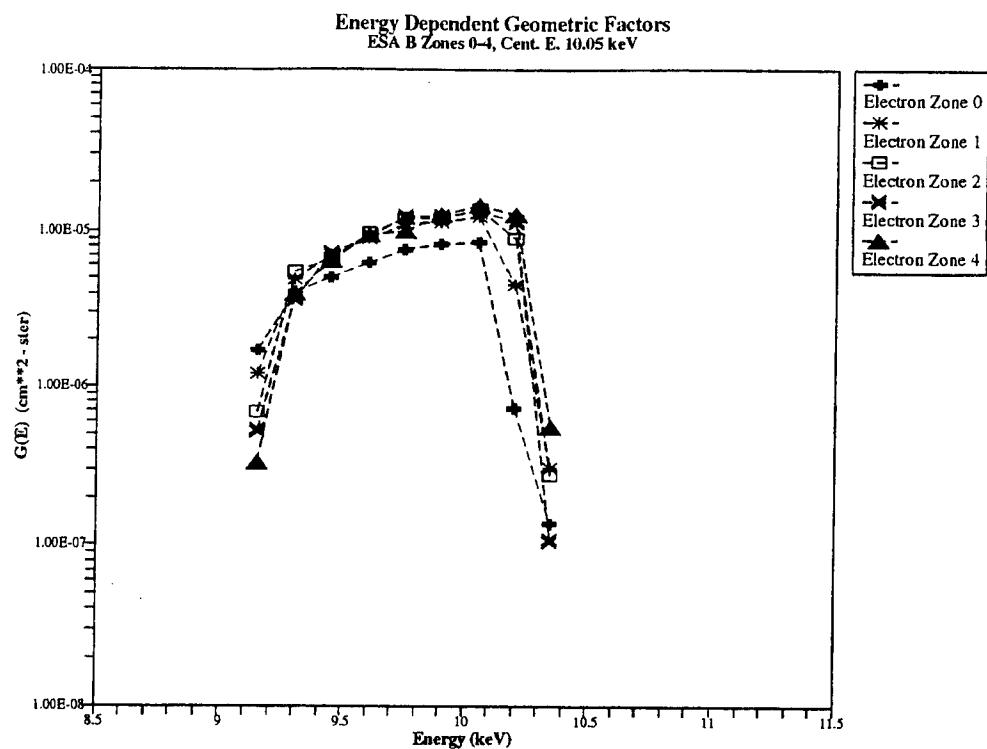


Figure 18. Electron Energy Dependent Geometric Factors for ESA B Zones 0-4 and 6-9
Plotted Versus Energy for the Channel With a Peak Response at 10000 eV
a) Zones 0-4; b) Zons 6-9

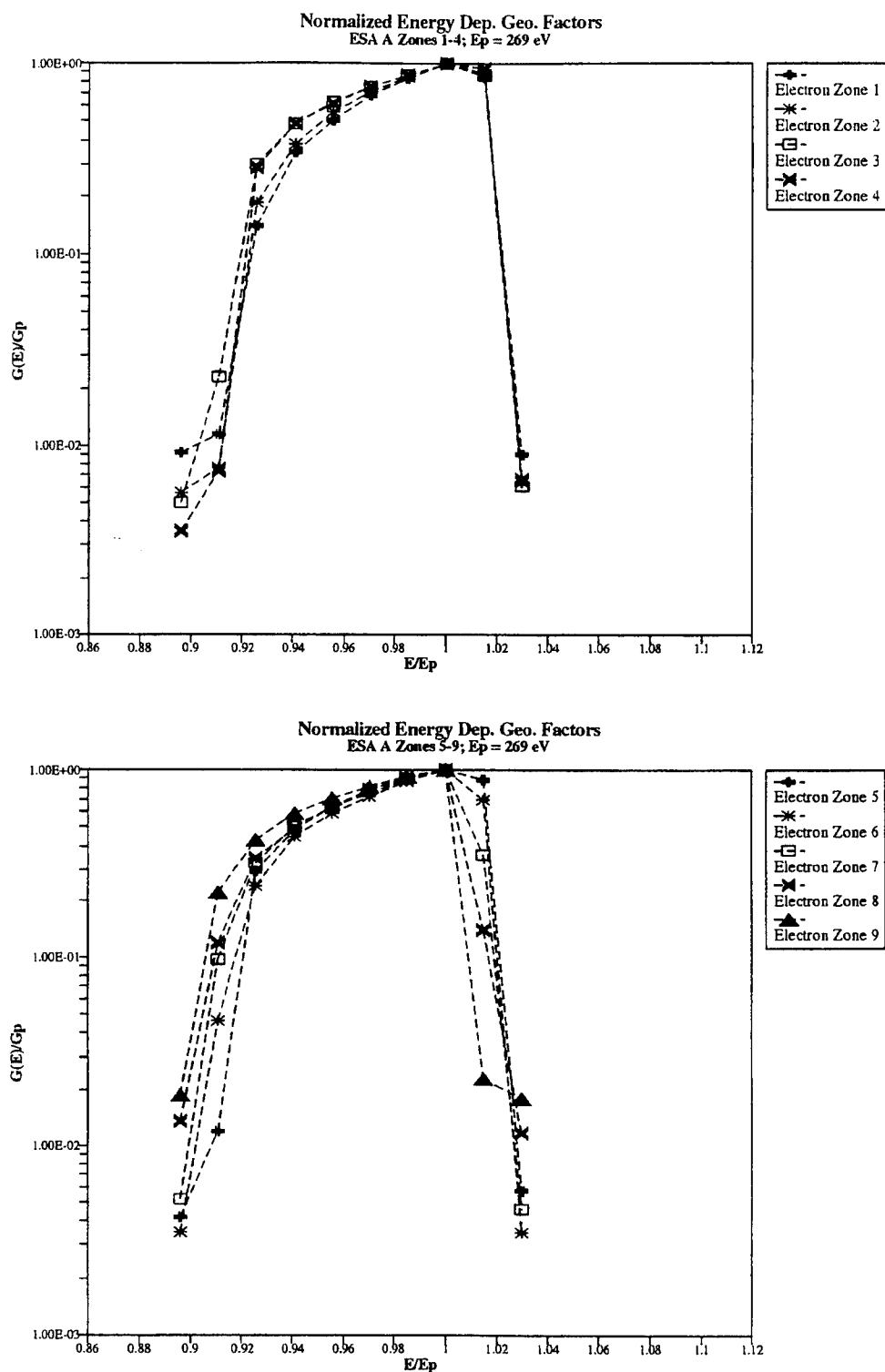


Figure 19. Normalized Electron Energy Dependent Geometric Factors Plotted vs. Normalized Energy for ESA A Zones 1-4 and 5-9 for the Channel With a Peak Response at 269 eV a) Zones 1-4; b) Zones 5-9

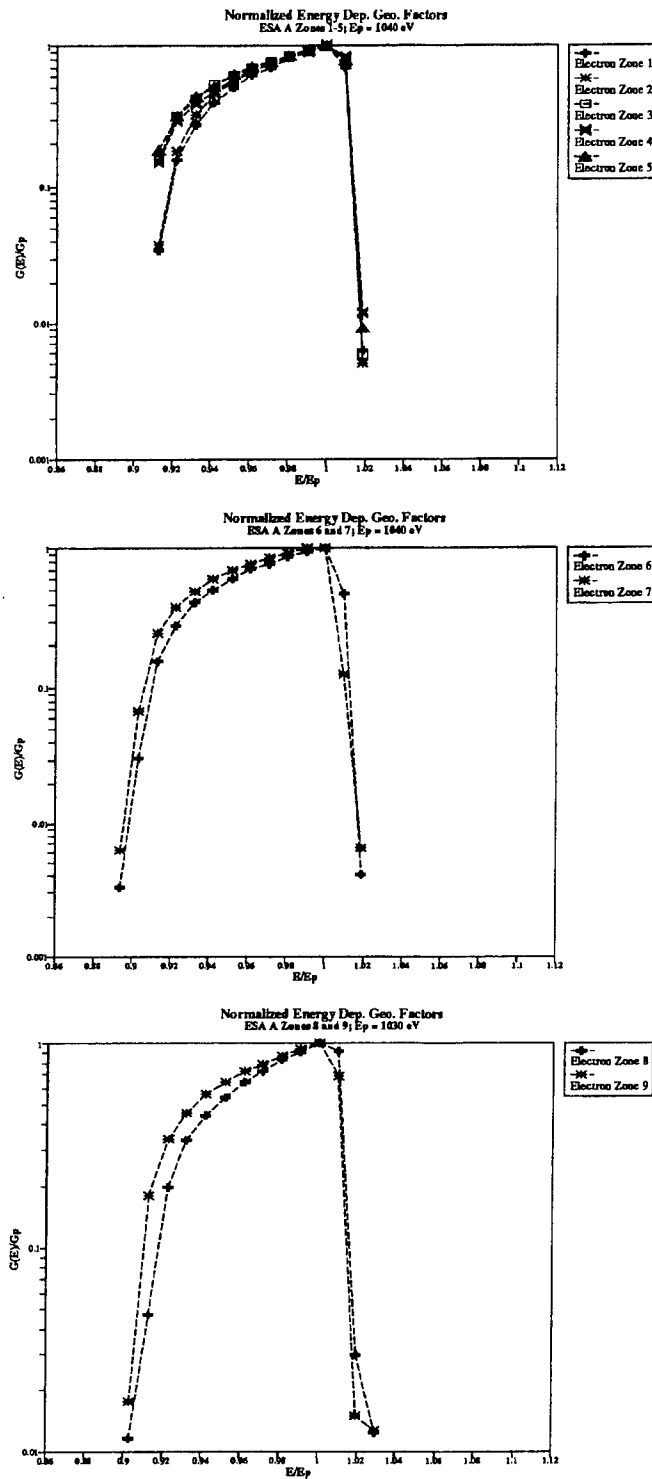


Figure 20. Normalized Electron Energy Dependent Geometric Factors Plotted vs. Normalized Energy for ESA A Zones 1-5 and 6-7 and 8-9 for the Channel With a Peak Response at 1030 eV a) Zones 1-5; b) Zones 6-7; c) Zones 8-9

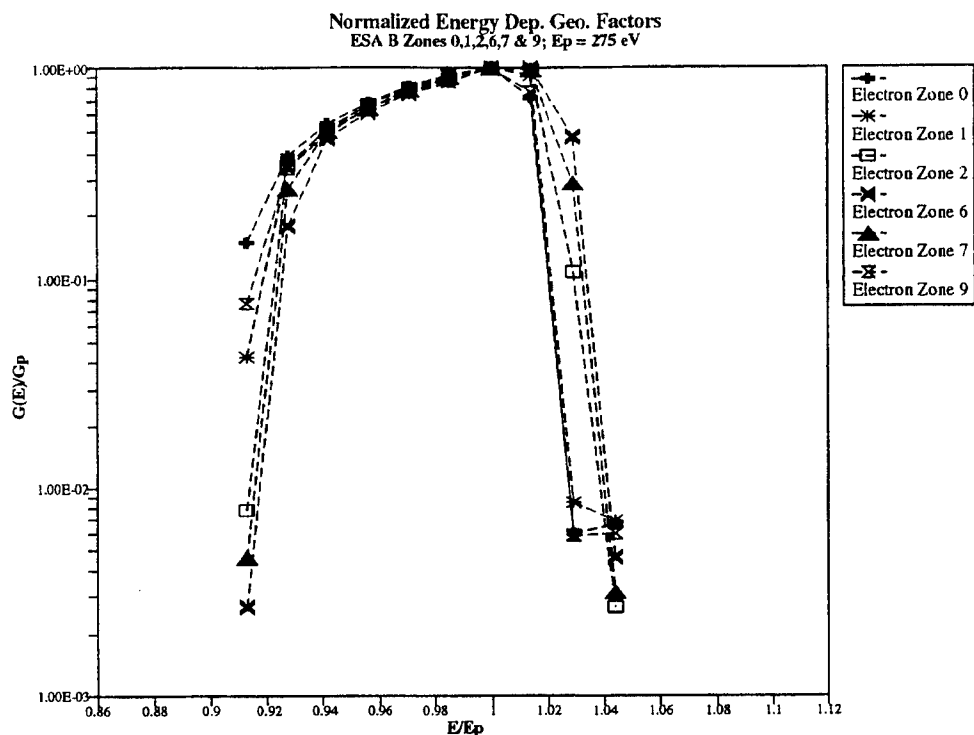


Figure 21. Normalized Electron Energy Dependent Geometric Factors Plotted vs. Normalized Energy for ESA B Zones 0, 1, 2, 6, 7, and 9 for the Channel With a Peak Response at 275 eV

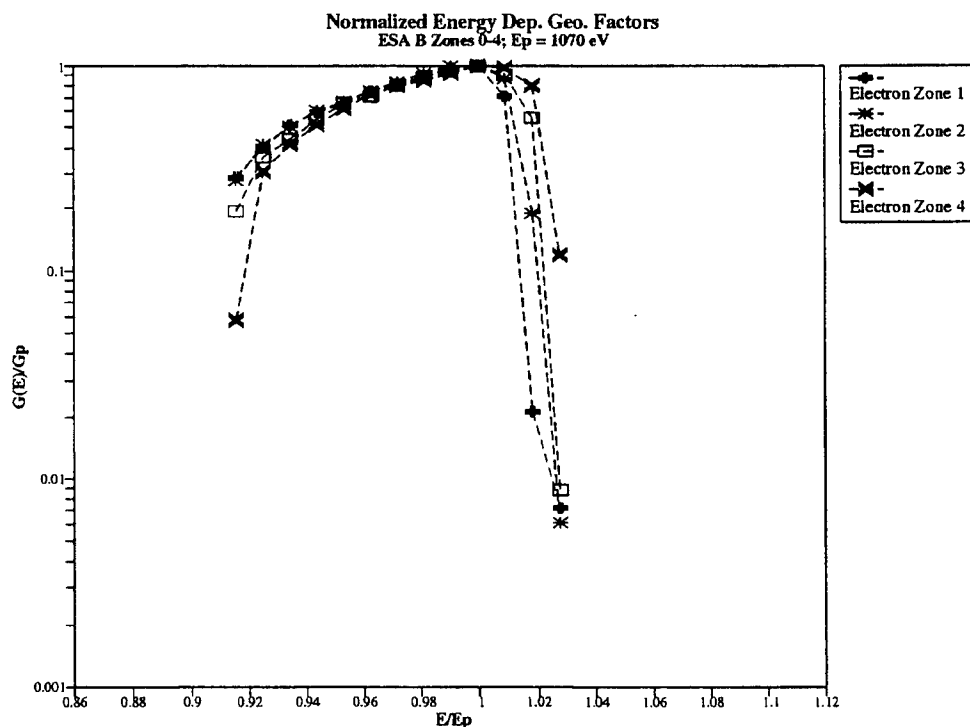


Figure 22. Normalized Electron Energy Dependent Geometric Factors Plotted vs. Normalized Energy for ESA B Zones 1-4 for the Channel With a Peak Response at 1070 eV

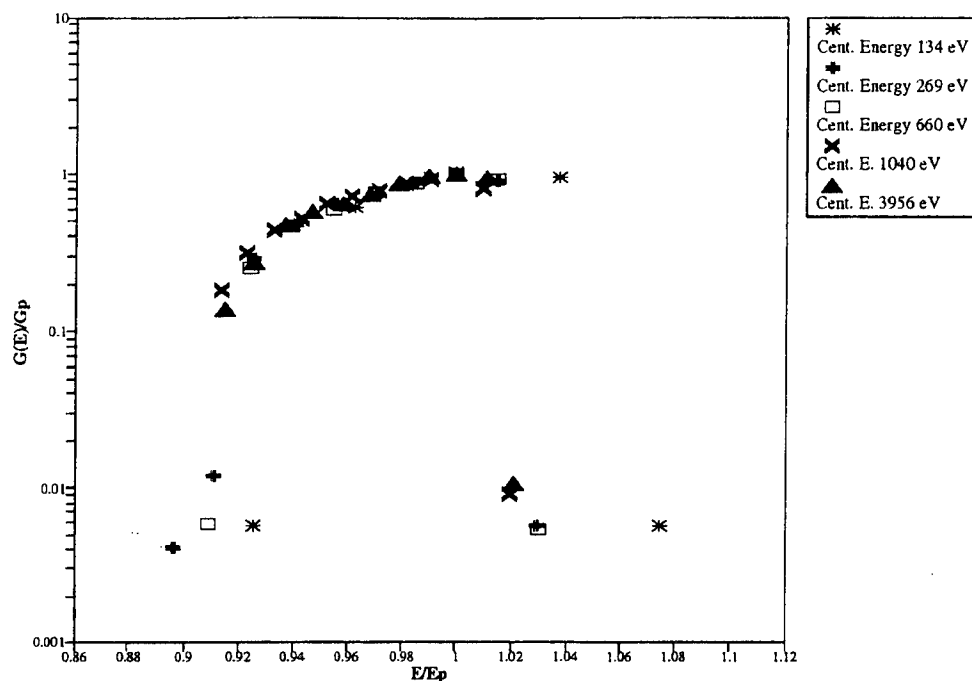


Figure 23. Normalized Electron Energy Dependent Geometric Factors Plotted vs. Normalized Energy for ESA A, Electron Zone 5 for the Channels With a Peak Response at 134, 269, 660, 1040, and 3956 eV

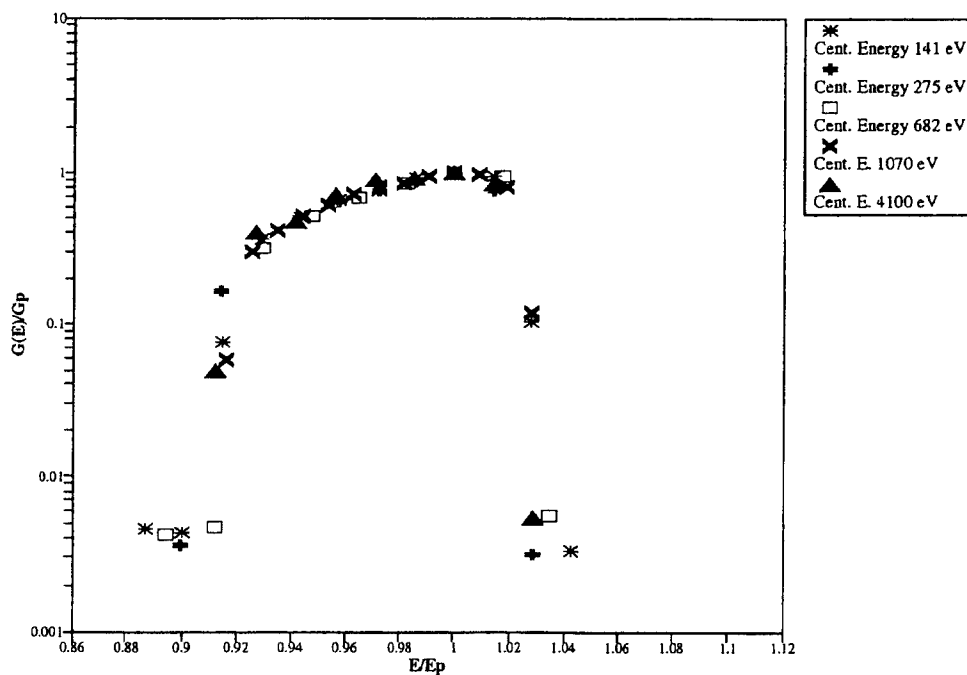


Figure 24. Normalized Electron Energy Dependent Geometric Factors Plotted vs. Normalized Energy for ESA B, Electron Zones 4 for the Channels With a Peak Response at 141, 275, 682, 1070, and 4100 eV

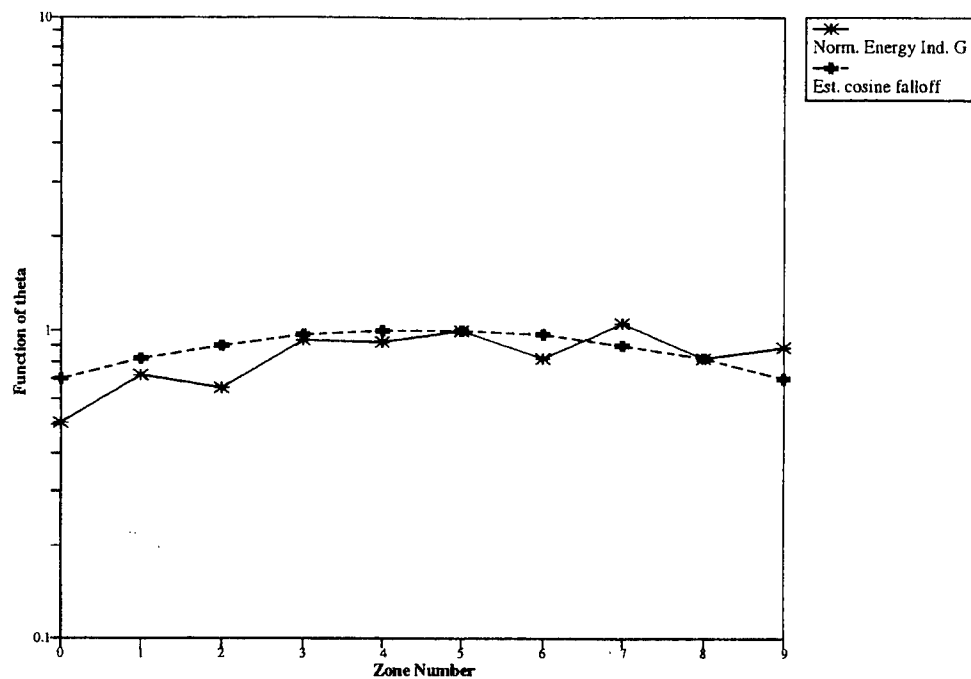


Figure 25. $f(\theta)$, the ESA A Normalized Electron Energy Independent Geometric Factor Averaged Over all Calibrated Energy Channels Plotted Versus Zone Number

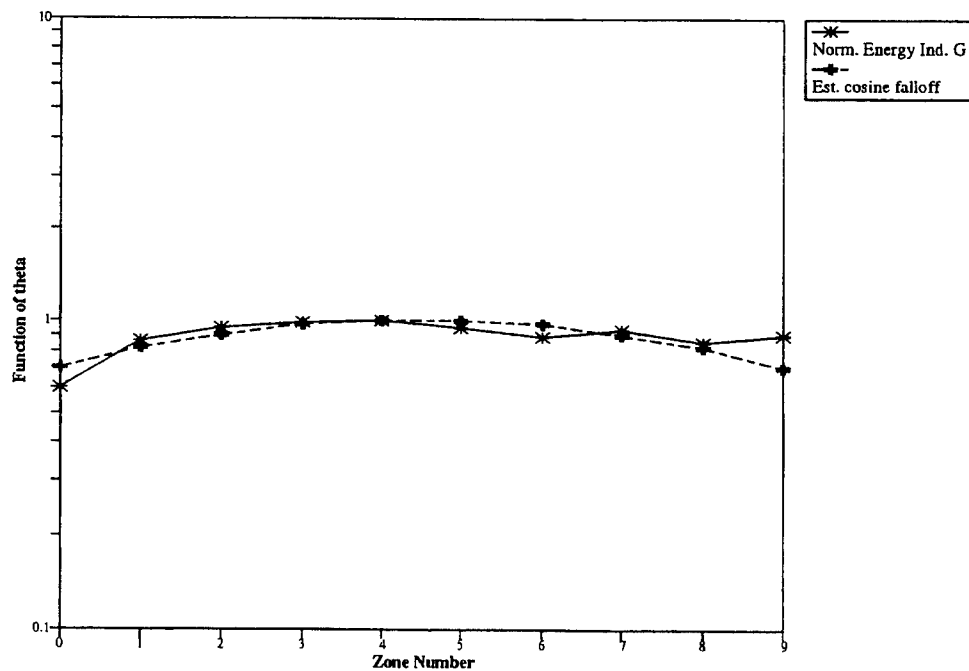


Figure 26. $f(\theta)$, the ESA B Normalized Electron Energy Independent Geometric Factor Averaged Over all Calibrated Energy Channels Plotted Versus Zone Number

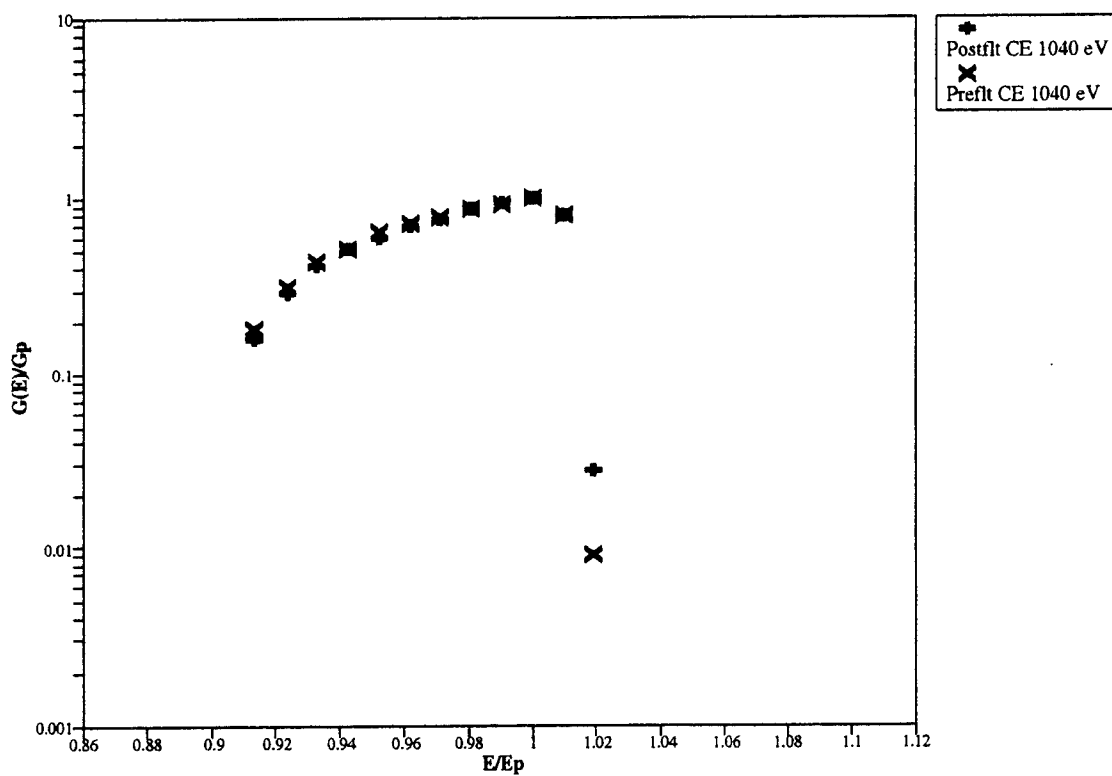


Figure 27. Normalized Electron Energy Dependent Geometric Factors Plotted vs. Normalized Energy for ESA A Zones 5 for Pre-flight and Post-flight Data Taken for the Channel With a Peak Response at 1040 eV

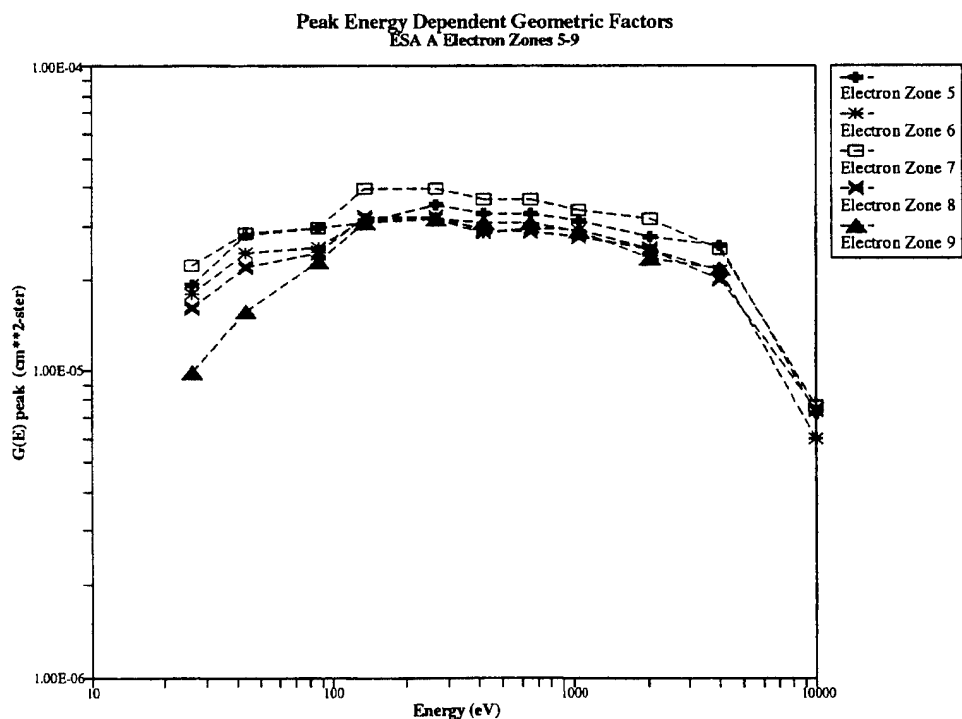
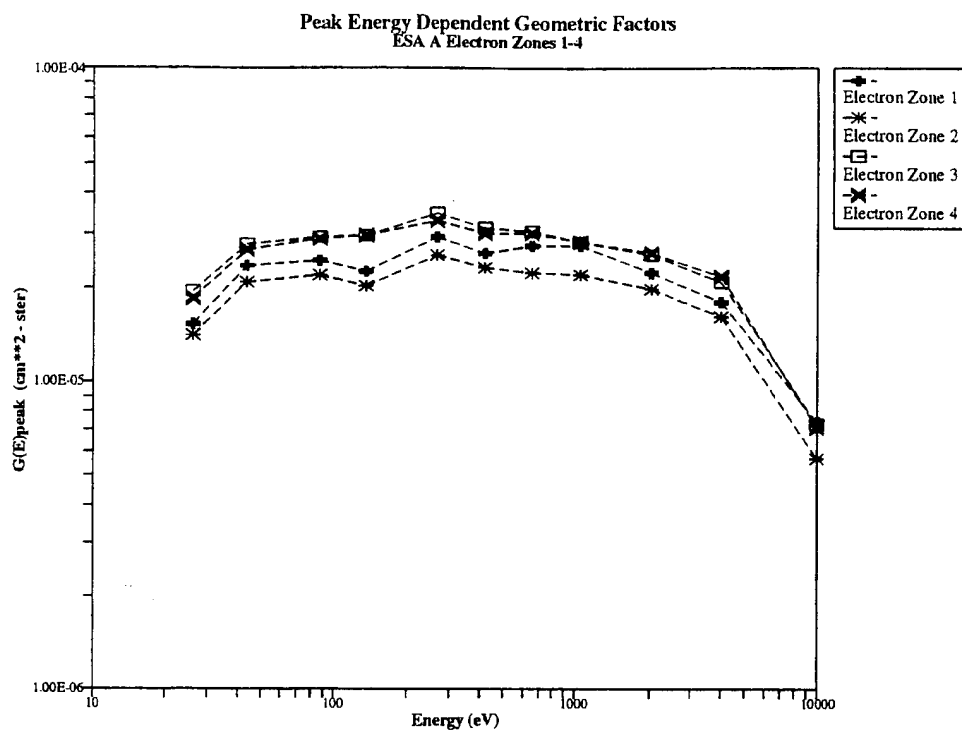


Figure 28. ESA A Peak Electron Energy Dependent Geometric Factors Plotted as a Function of Energy a) Zones 1-4; b) Zones 5-9

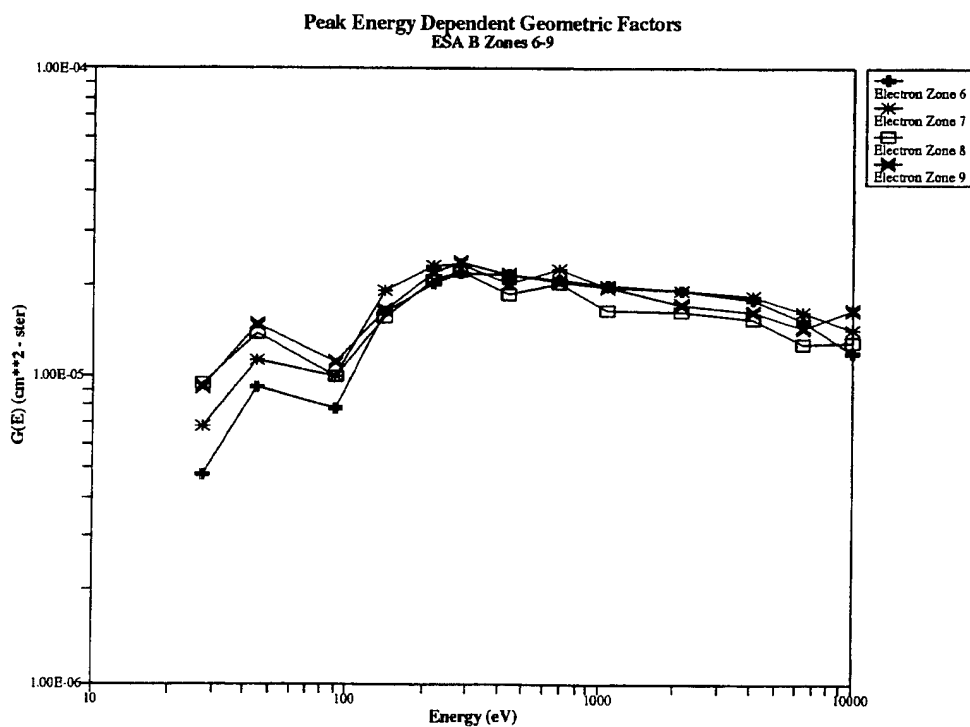
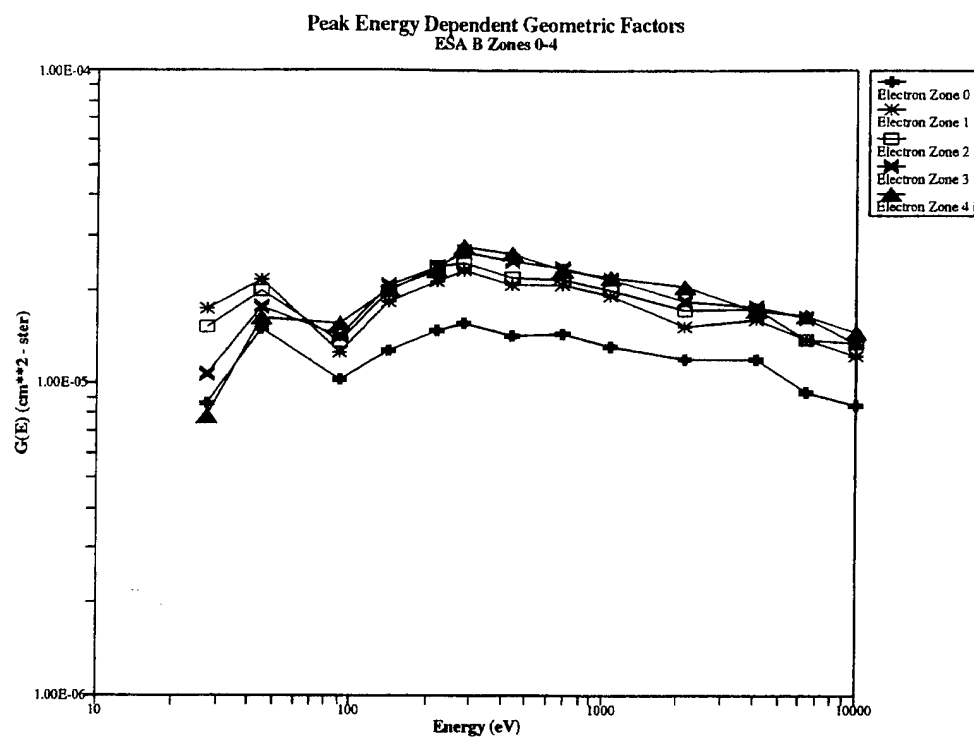


Figure 29. ESA B Peak Electron Energy Dependent Geometric Factors Plotted as a Functions of Energy a) Zones 0-4; b) Zones 6-9

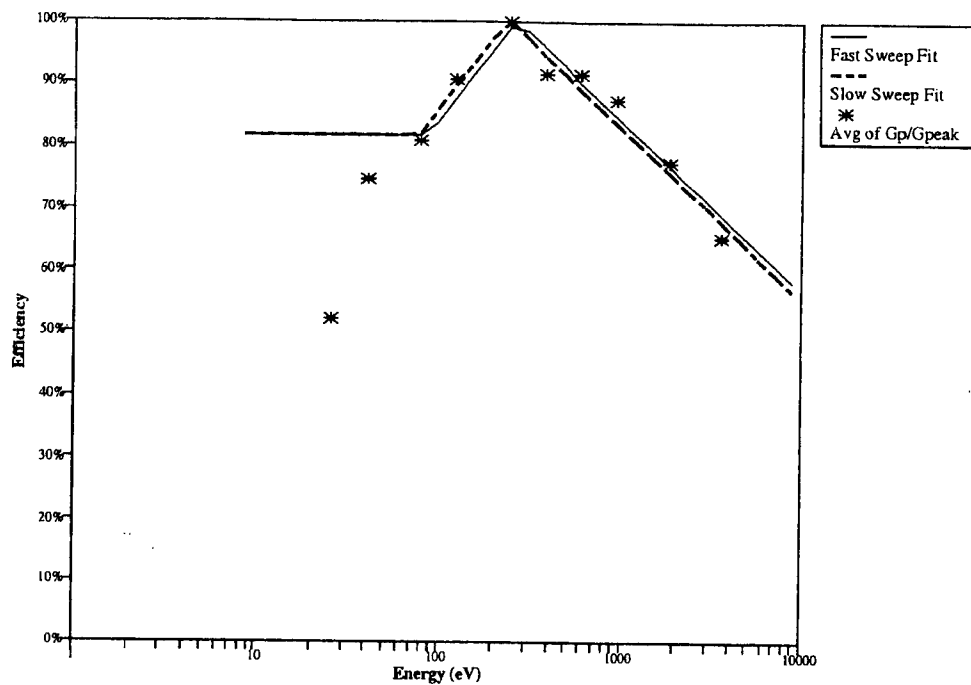


Figure 30. ESA A Electron Detection Efficiency Plotted Versus Energy

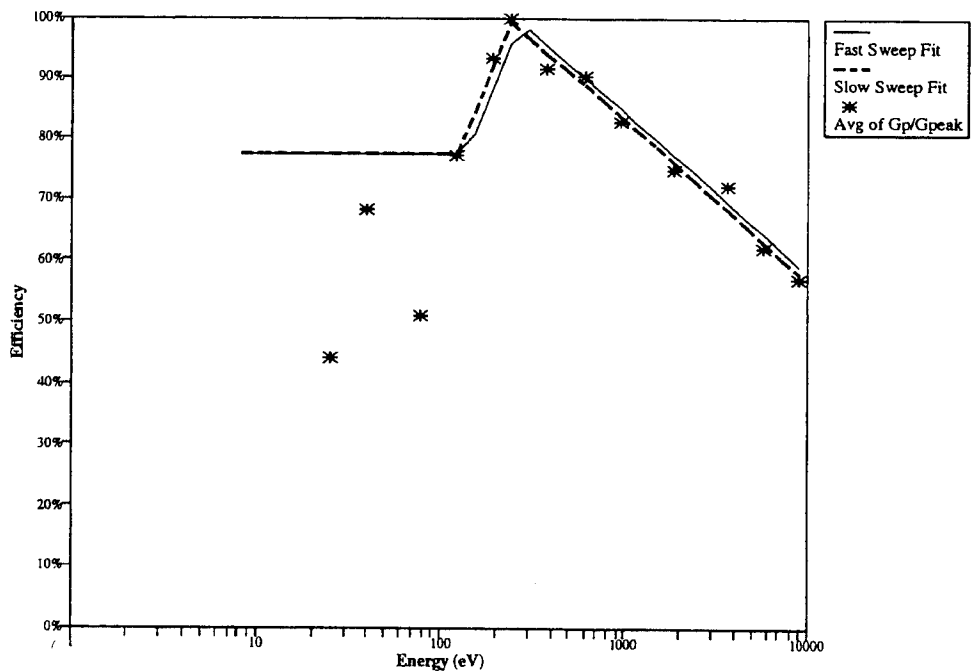


Figure 31. ESA B Electron Detection Efficiency Plotted Versus Energy

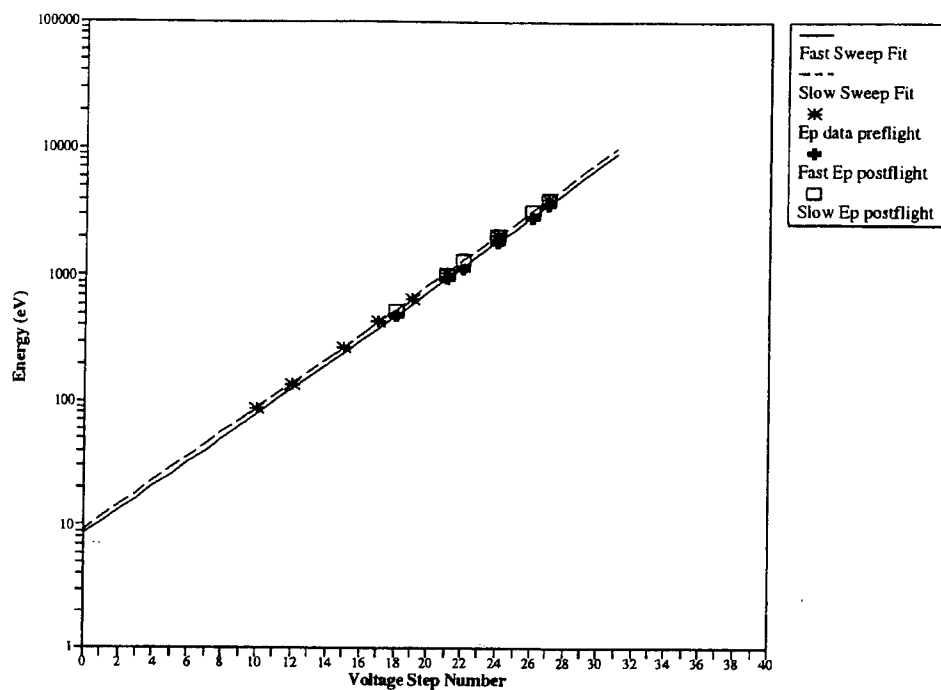


Figure 32. Central Energy of the ESA A Electron Channels Plotted Versus Channel Number

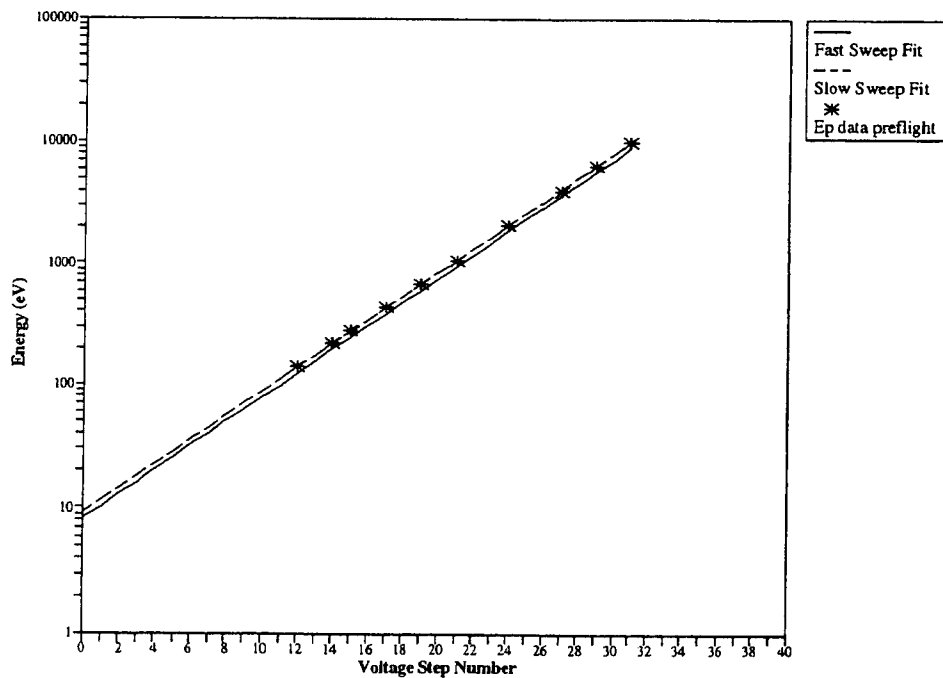


Figure 33. Central Energy of the ESA B Electron Channels Plotted Versus Channel Number

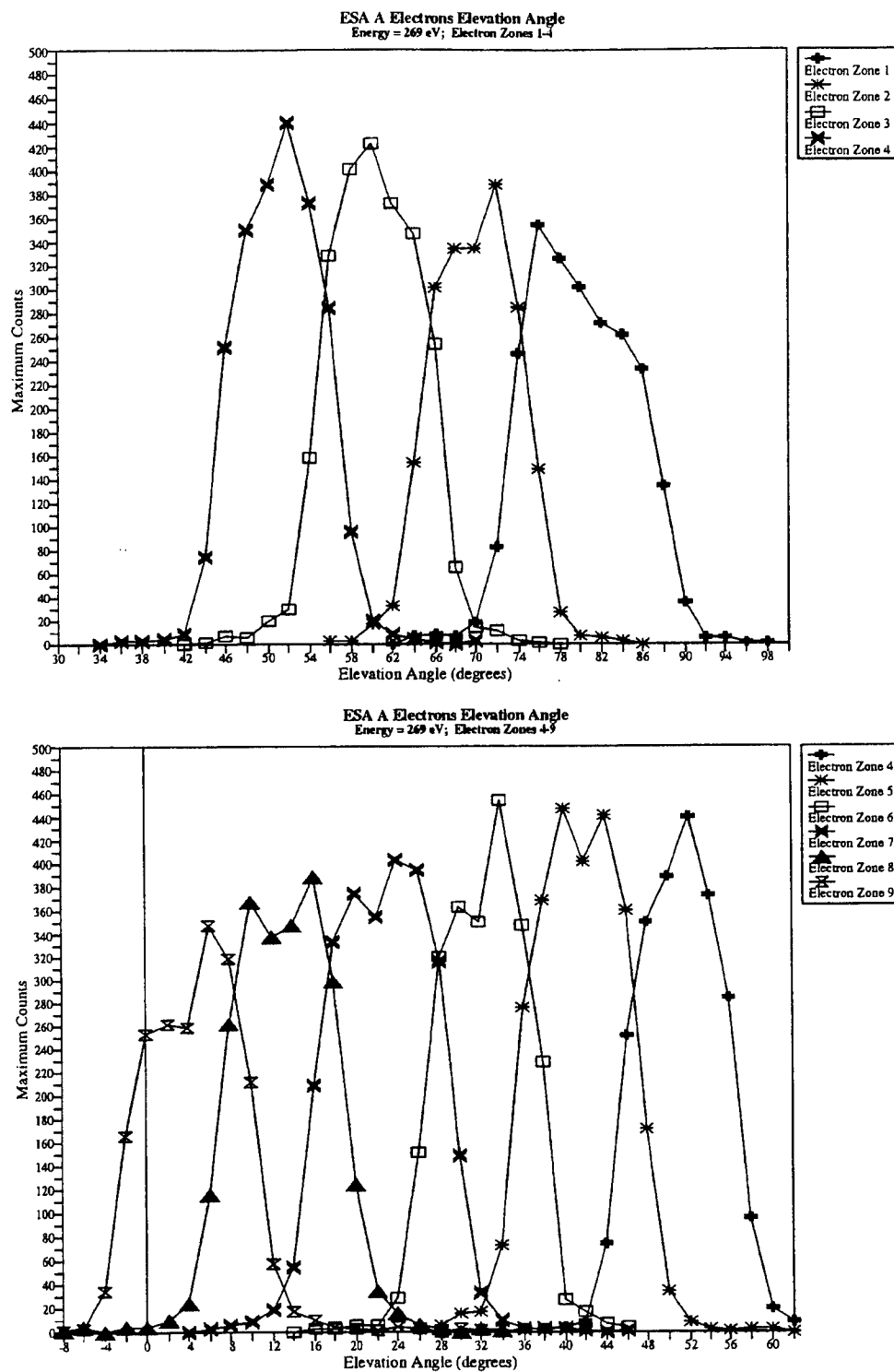


Figure 34. Counts Versus Elevation Angle for ESA A Electron Zones 1-9, for the Energy Channel with a Peak Response at 269 eV. a) Zones 1-4; b) Zones 4-9 The Data are for a Fixed Elevation Angle Within the Angular Scan at 269 eV at a Fixed Azimuth Angle Such That the Elevation Plot Includes the Maximum Counts in the Scan.

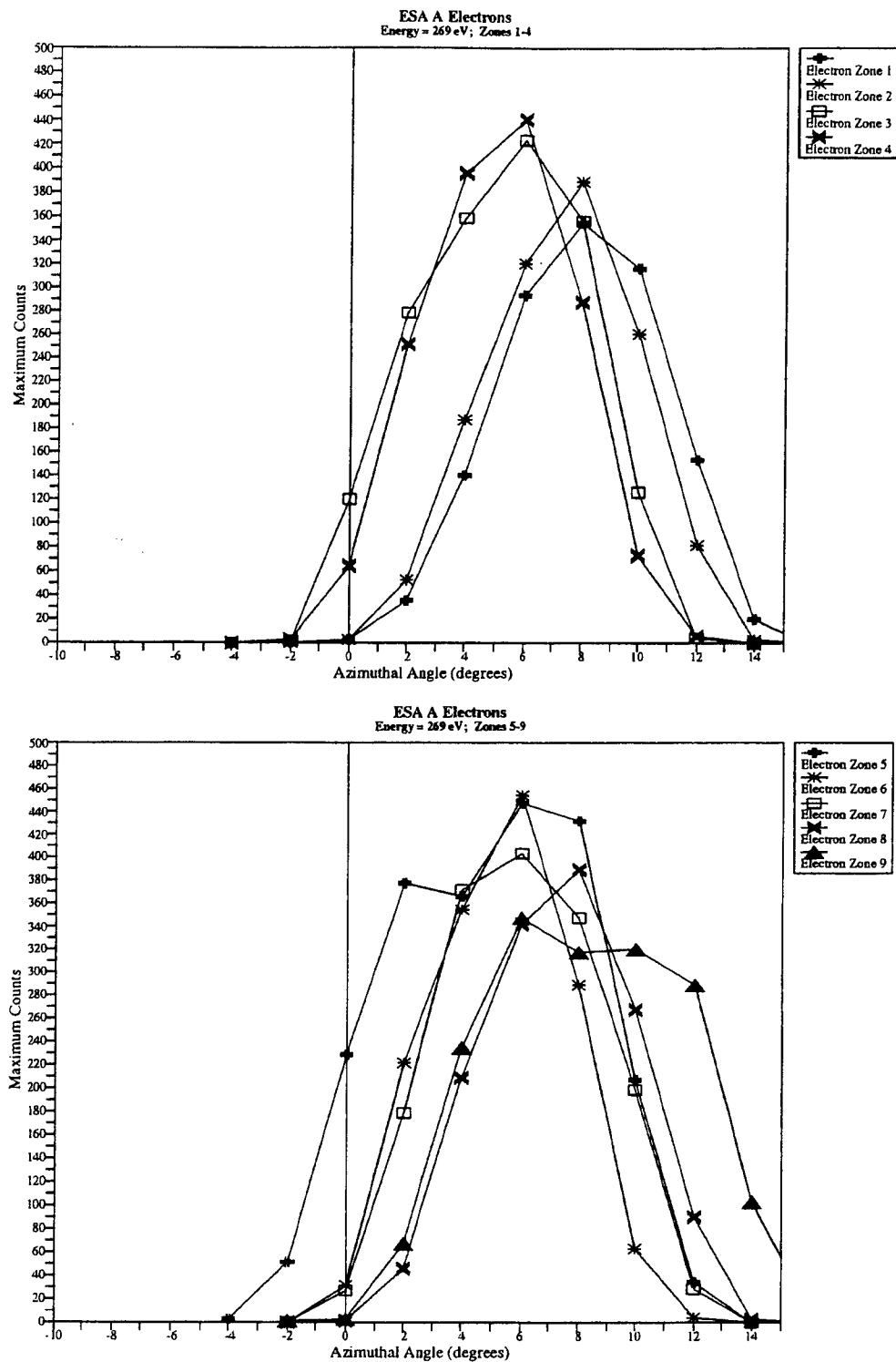


Figure 35. Counts Versus Azimuthal Angle for ESA A Electron Zones 1-9 for the Energy Channel With a Peak Response at 269 eV. a) Zones 1-4; b) Zones 5-9 The Data are for a Fixed Elevation Angle Within the Angular Scan at 269 eV at a Fixed Elevation Angle Such That the Azimuth Plot Includes the Maximum Counts in the Scan

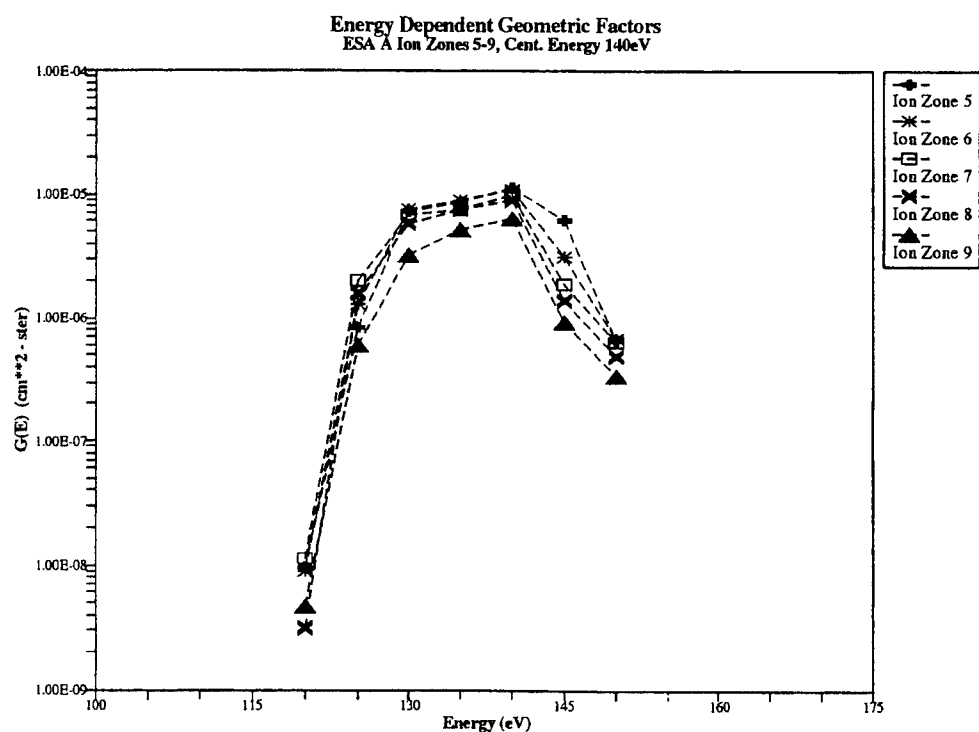
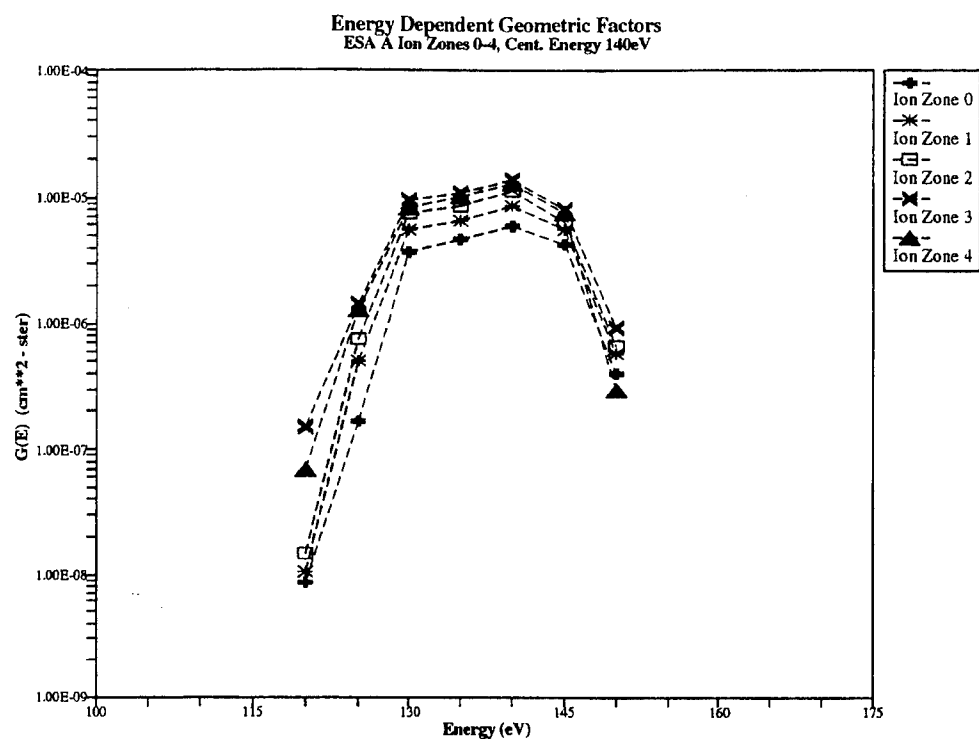


Figure 36. Ion Energy Dependent Geometric Factors for ESA A Zones 0-9 Plotted Versus Energy for the Energy Channel With a Peak Response at 140 eV
a) Zones 0-4; b) Zones 5-9

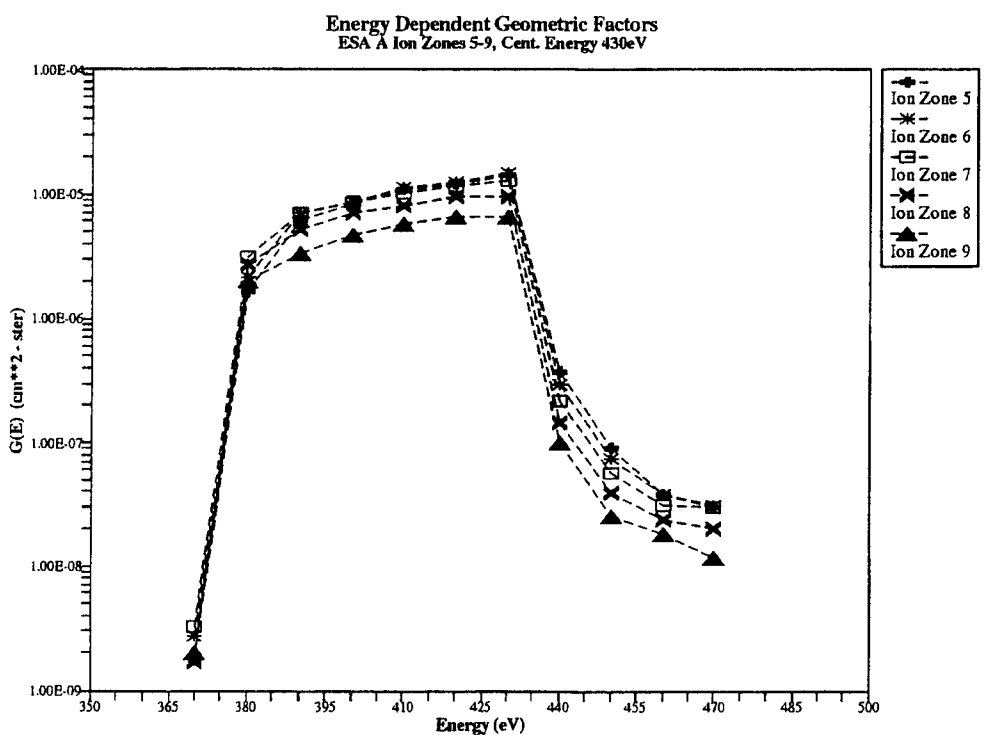
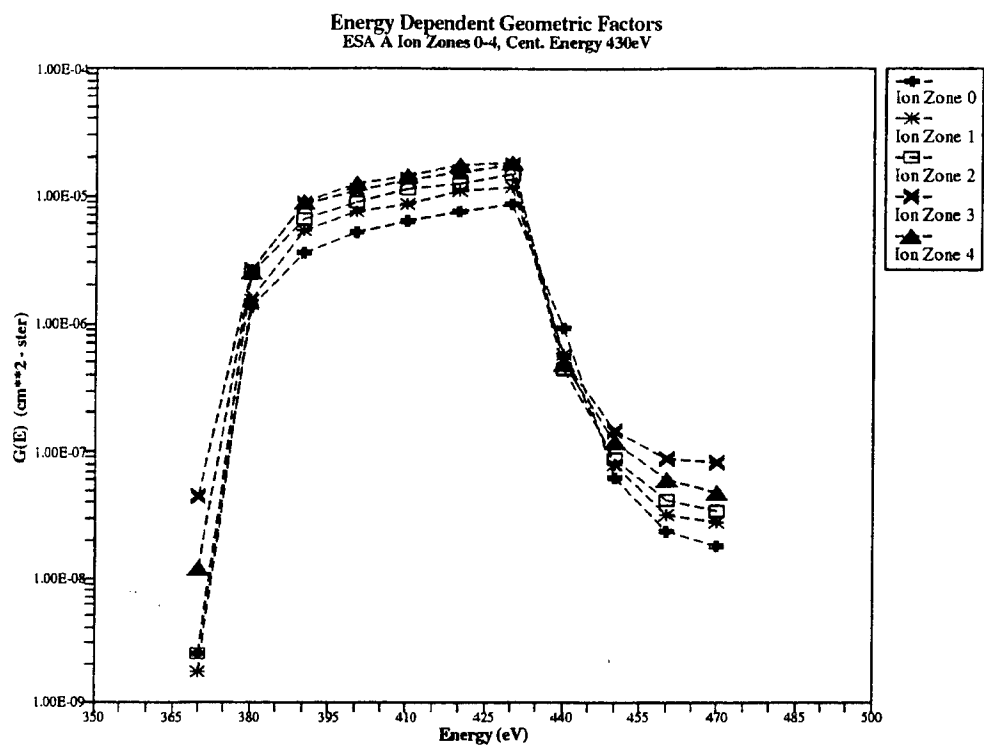


Figure 37. Ion Energy Dependent Geometric Factors for ESA A Zones 0-9 Plotted Versus Energy for the Energy Channel With a Peak Response at 430 eV
a) Zones 0-4; b) Zones 5-9

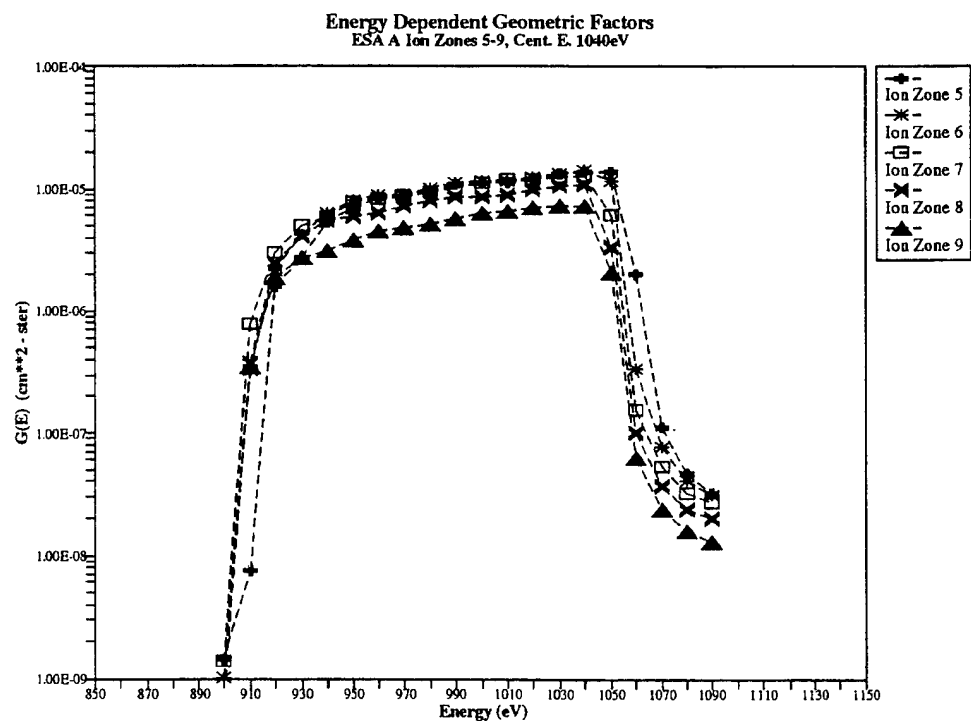
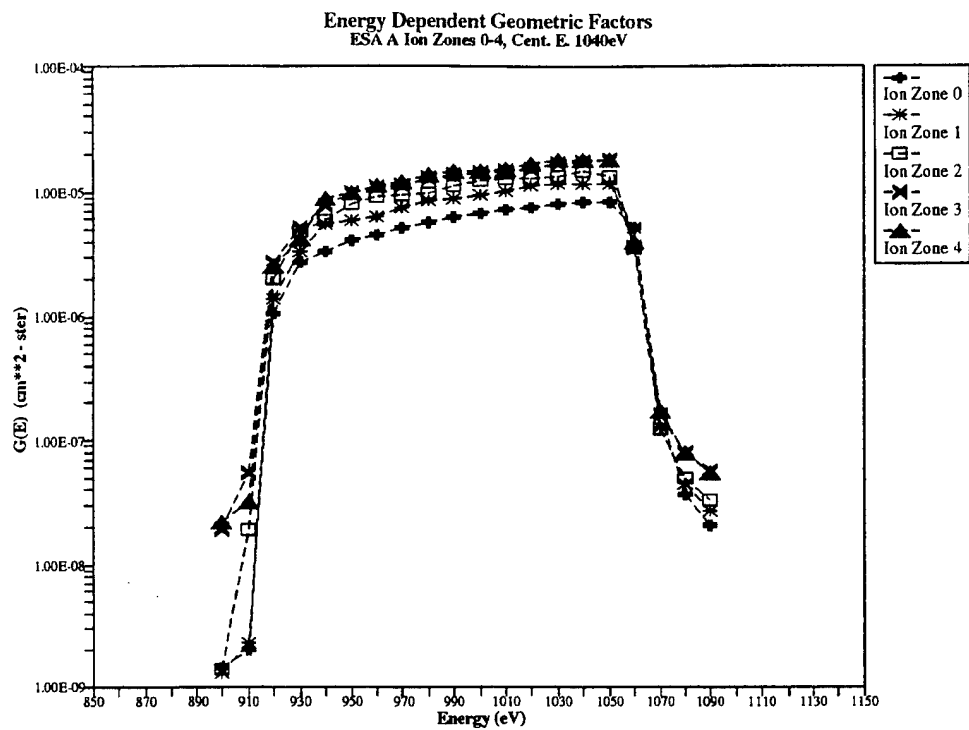


Figure 38. Ion Energy Dependent Geometric Factors for ESA A Zones 0-9 Plotted Versus Energy for the Energy Channel With a Peak Response at 1040 eV
a) Zones 0-4; b) Zones 5-9

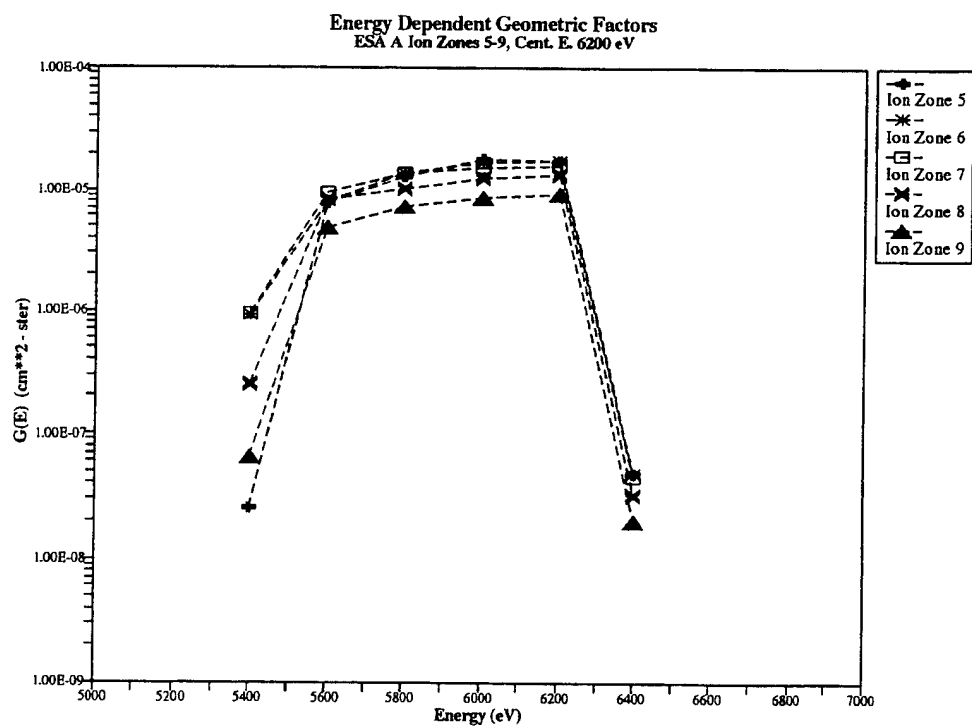
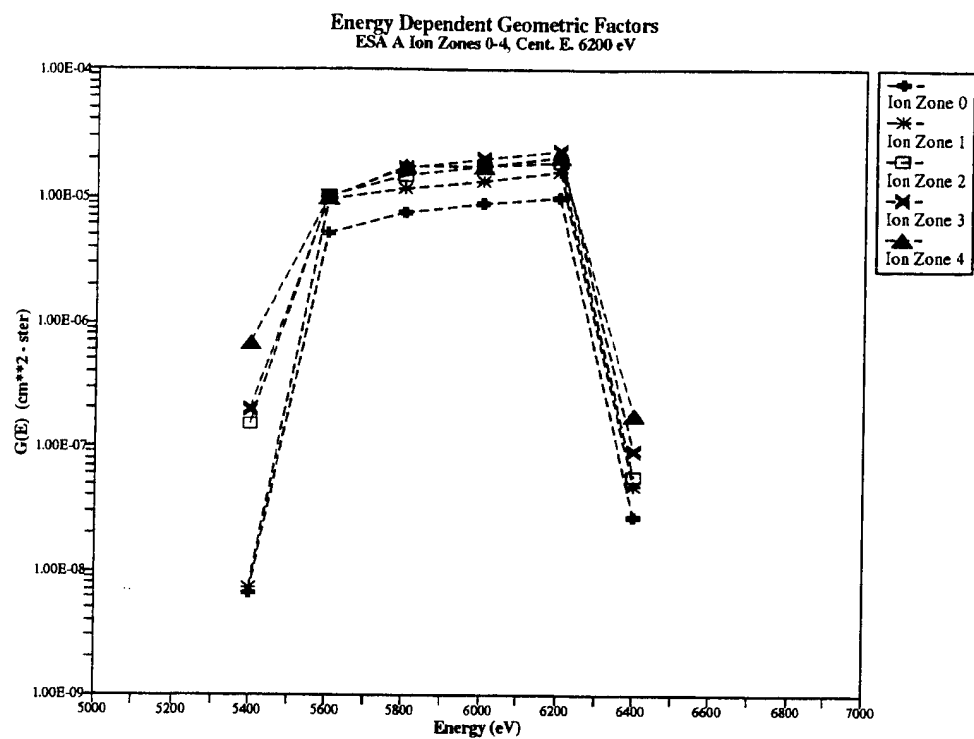


Figure 39. Ion Energy Dependent Geometric Factors for ESA A Zones 0-9 Plotted Versus Energy for the Energy Channel With a Peak Response at 6200 eV
a) Zones 0-4; b) Zones 5-9

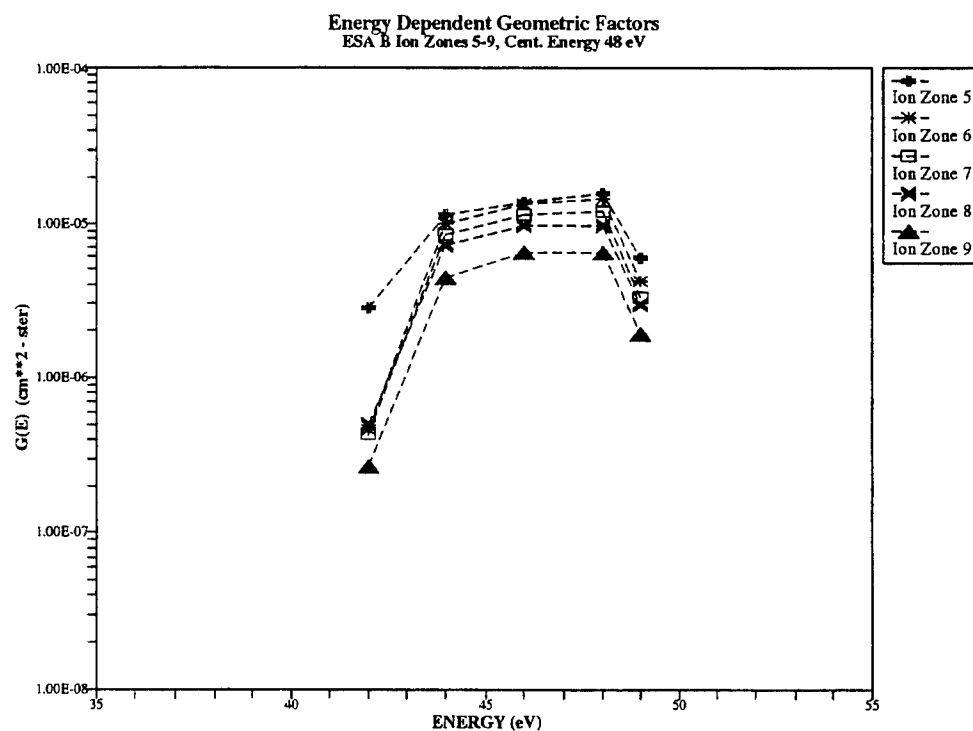
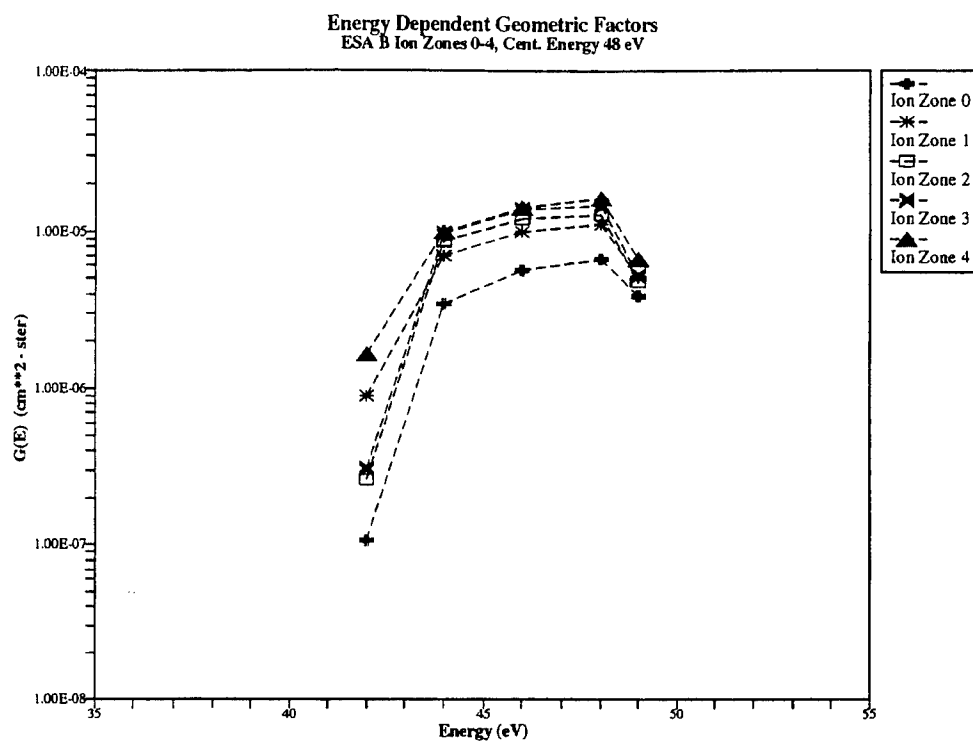


Figure 40. Ion Energy Dependent Geometric Factors for ESA B Zones 0-9 Plotted Versus Energy for the Energy Channel with a Peak Response at 48 eV
a) Zones 0-4; b) Zones 5-9

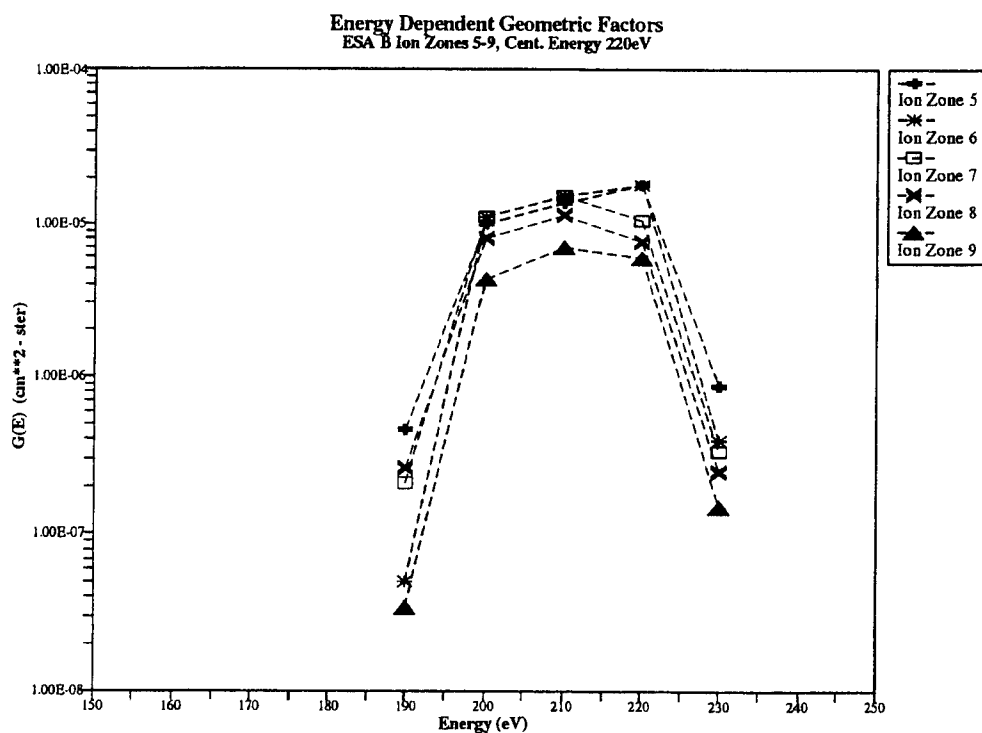
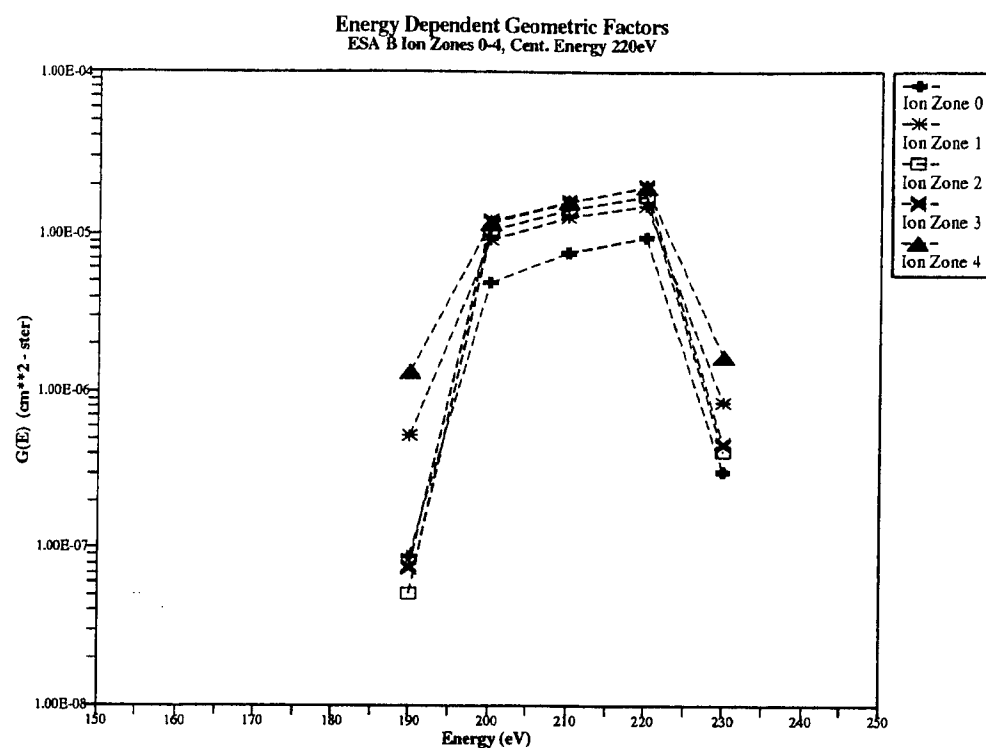


Figure 41. Ion Energy Dependent Geometric Factors for ESA B Zones 0-9 Plotted Versus Energy for the Energy Channel With a Peak Response at 210 eV
a) Zones 0-4; b) Zones 5-9

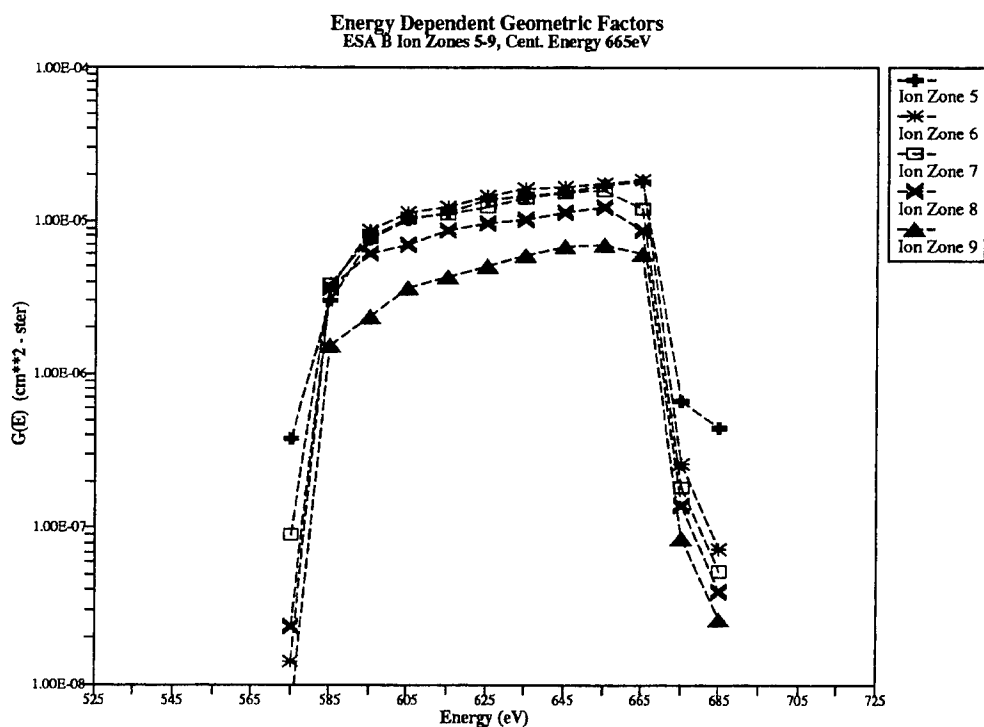
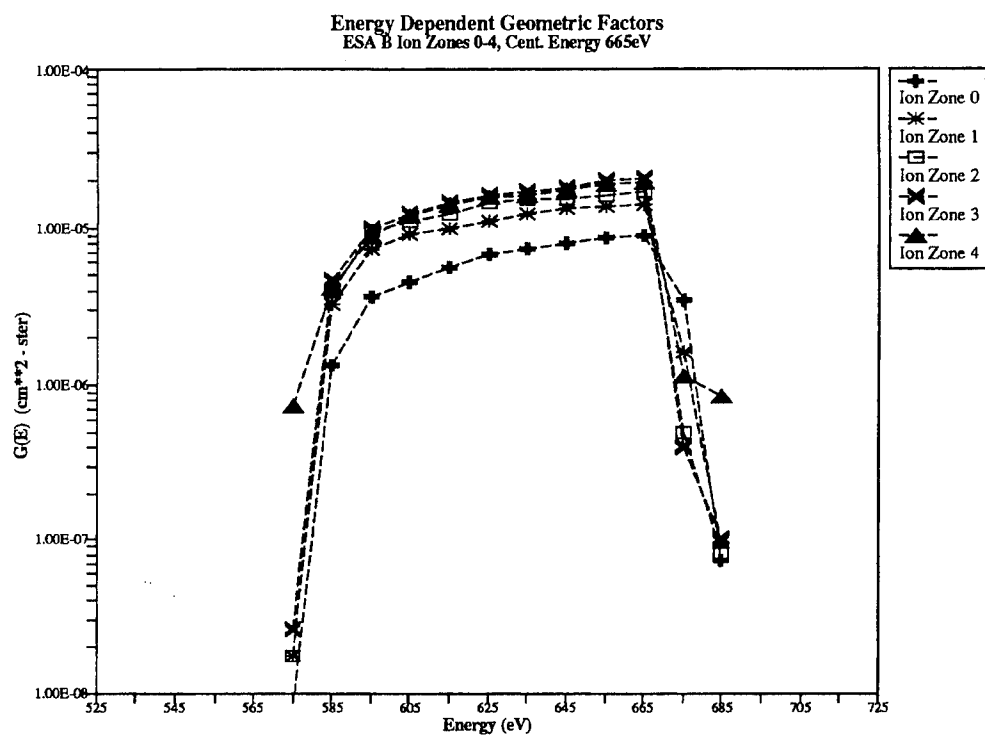


Figure 42. Ion Energy Dependent Geometric Factors for ESA B Zones 0-9 Plotted Versus Energy for the Energy Channel With a Peak Response at 665 eV
a) Zones 0-4; b) Zones 5-9

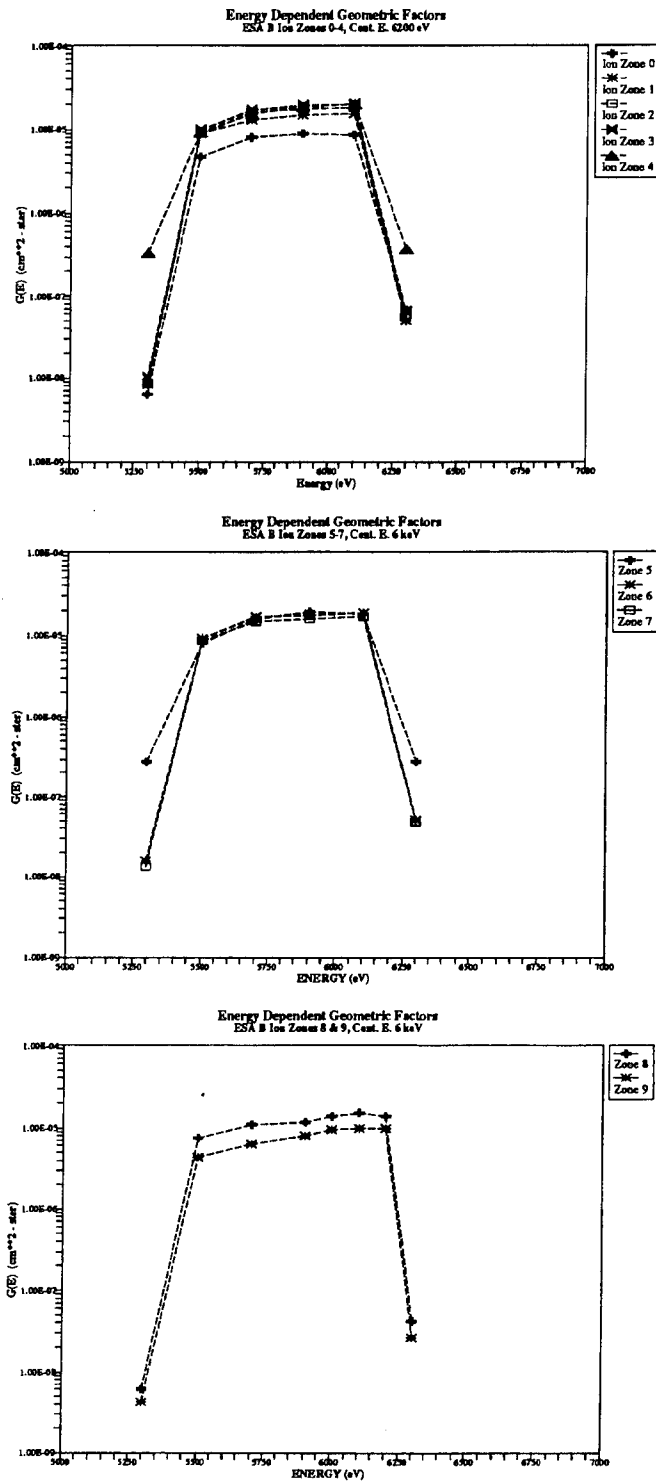


Figure 43. Ion Energy Dependent Geometric Factors for ESA B Zones 0-9 Plotted Versus Energy for the Energy Channel With a Peak Response at 6200 eV
a) Zones 0-4; b) Zones 5-7; c) Zones 8 and 9

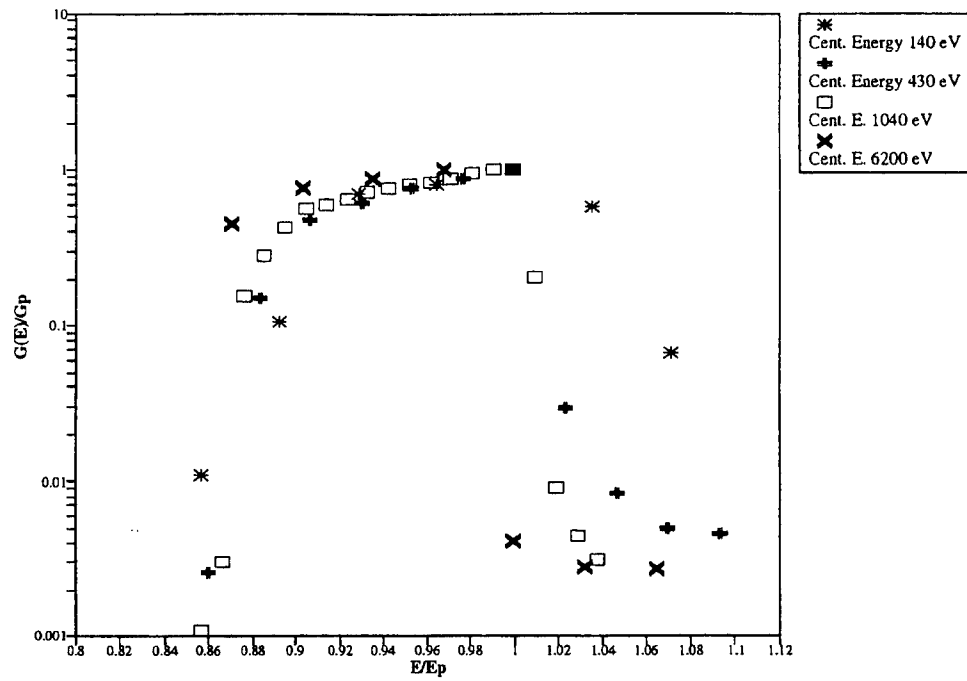


Figure 44. Normalized Ion Energy Dependent Geometric Factors Plotted vs. Normalized Energy for ESA A, Ion Zone 4 for the Energy Channels With a Peak Response at Energies of 140, 430, 1040, and 6200 eV

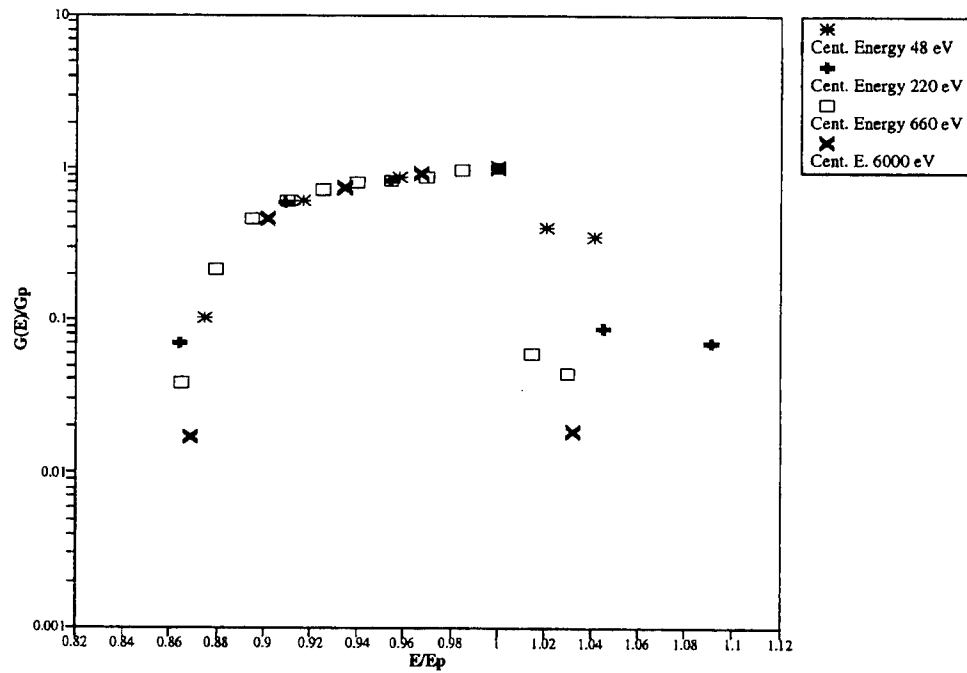


Figure 45. Normalized Ion Energy Dependent Geometric Factors Plotted vs. Normalized Energy for ESA B, Ion Zone 3 for the Energy Channels With a Peak Response at Energies of 48, 220, 660, and 6000 eV

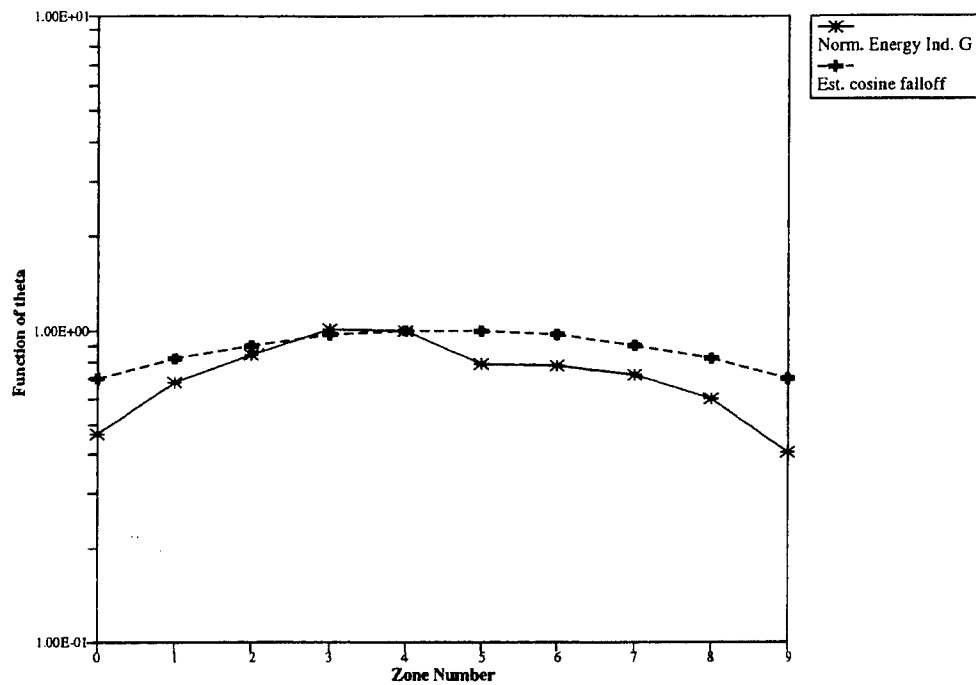


Figure 46. $f(\theta)$, the ESA A Normalized Ion Energy Independent Geometric Factor Averaged Over all Calibrated Energy Channels Plotted Versus Zone Number

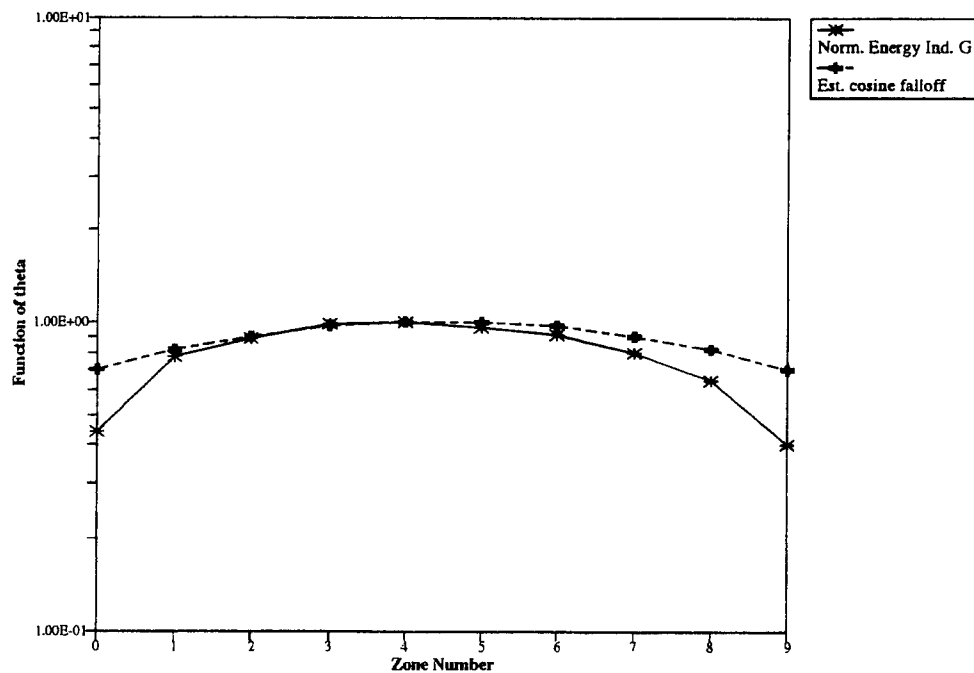


Figure 47. $f(\theta)$, the ESA B Normalized Ion Energy Independent Geometric Factor Averaged Over all Calibrated Energy Channels Plotted Versus Zone Number

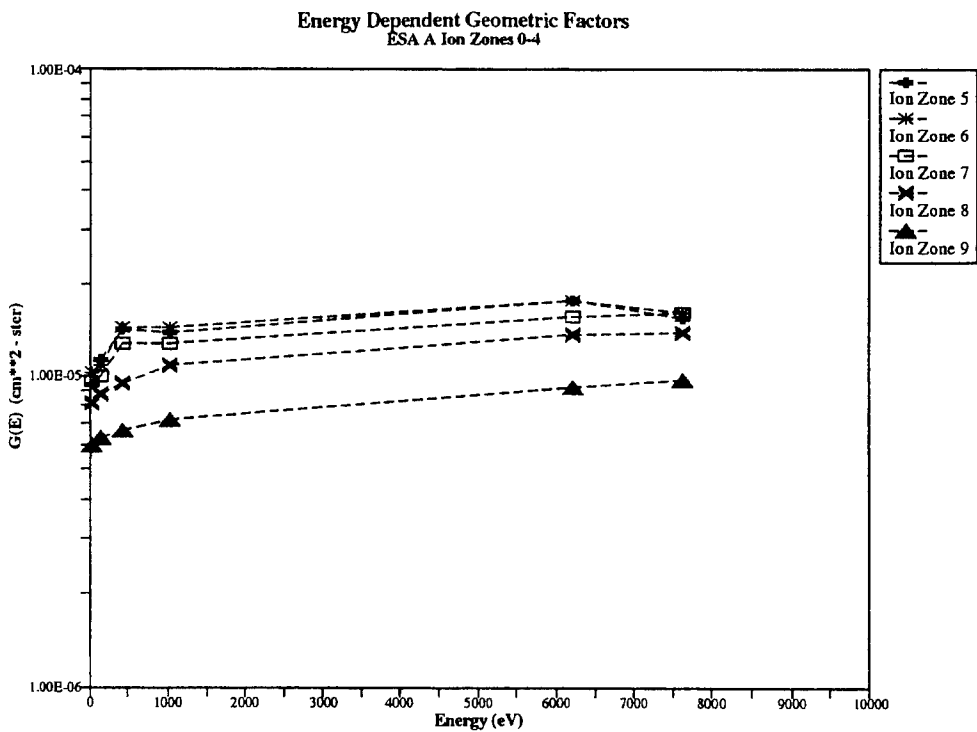
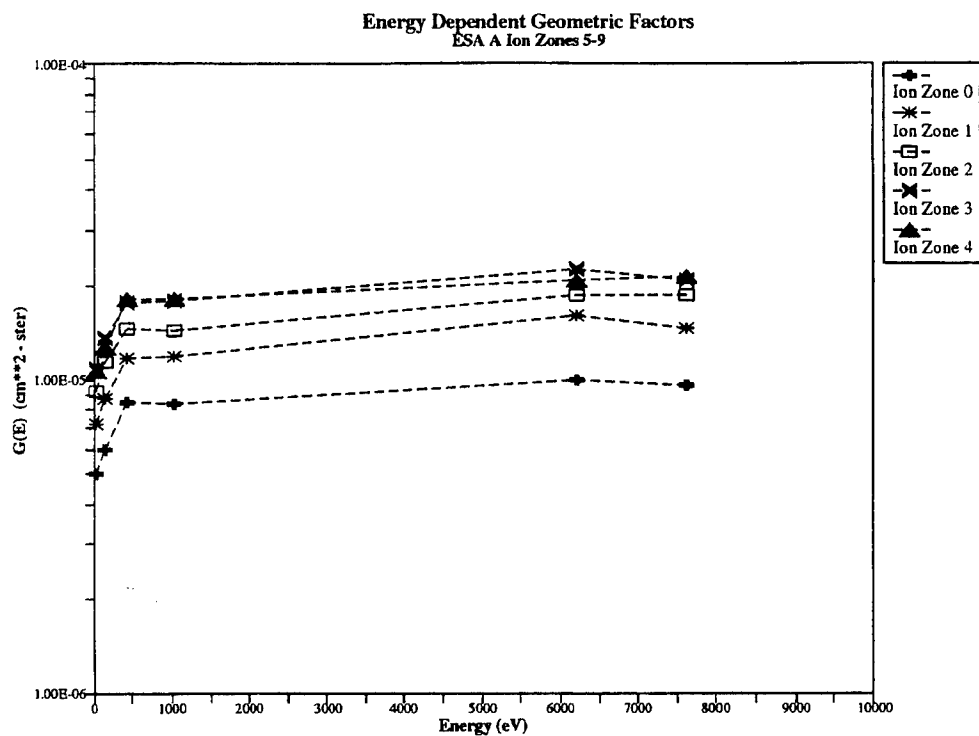


Figure 48. ESA A Ion Peak Electron Energy Dependent Geometric Factors Plotted as a Function of Energy a) Zones 0-4; b) Zones 5-9

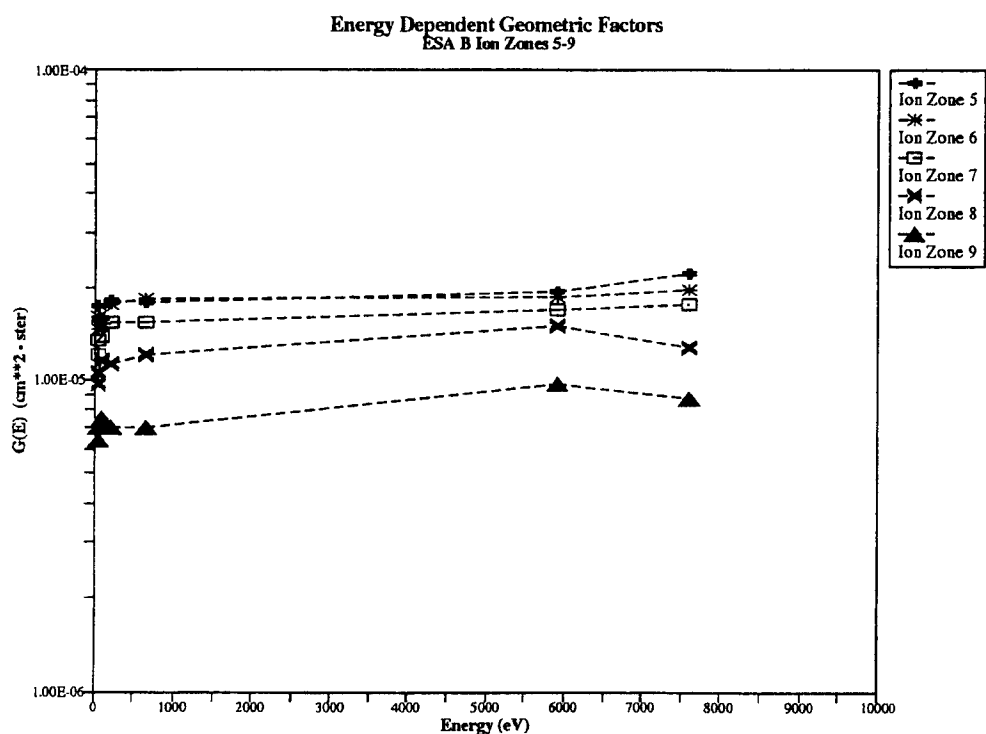
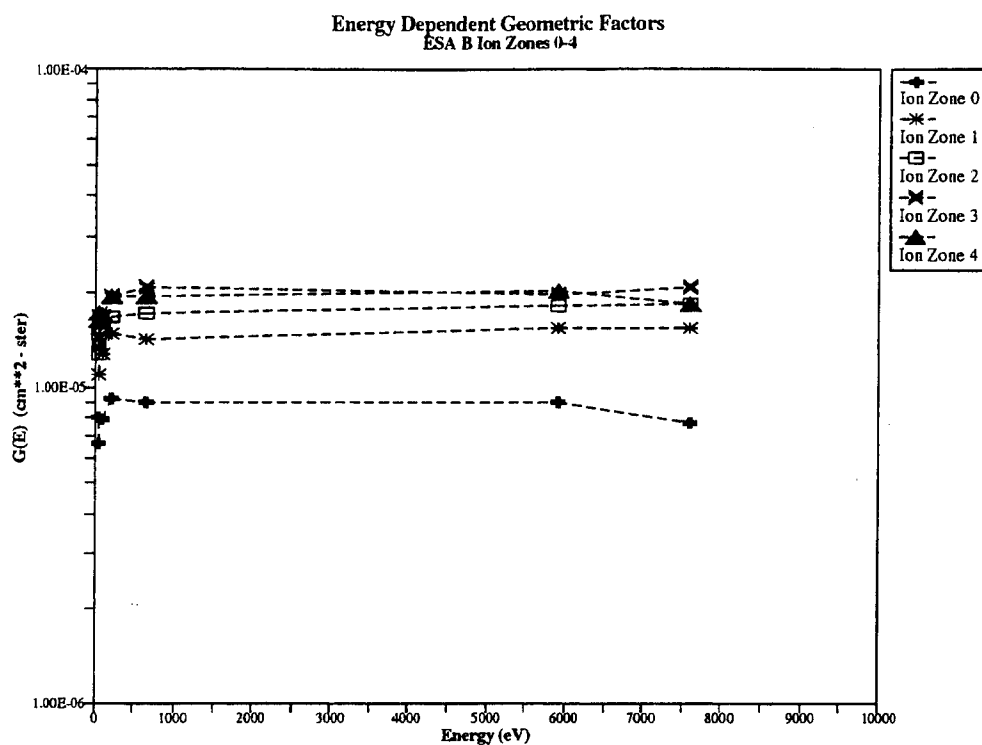


Figure 49. ESA B Ion Peak Electron Energy Dependent Geometric Factors Plotted as a Function of Energy a) Zones 0-4; b) Zones 5-9

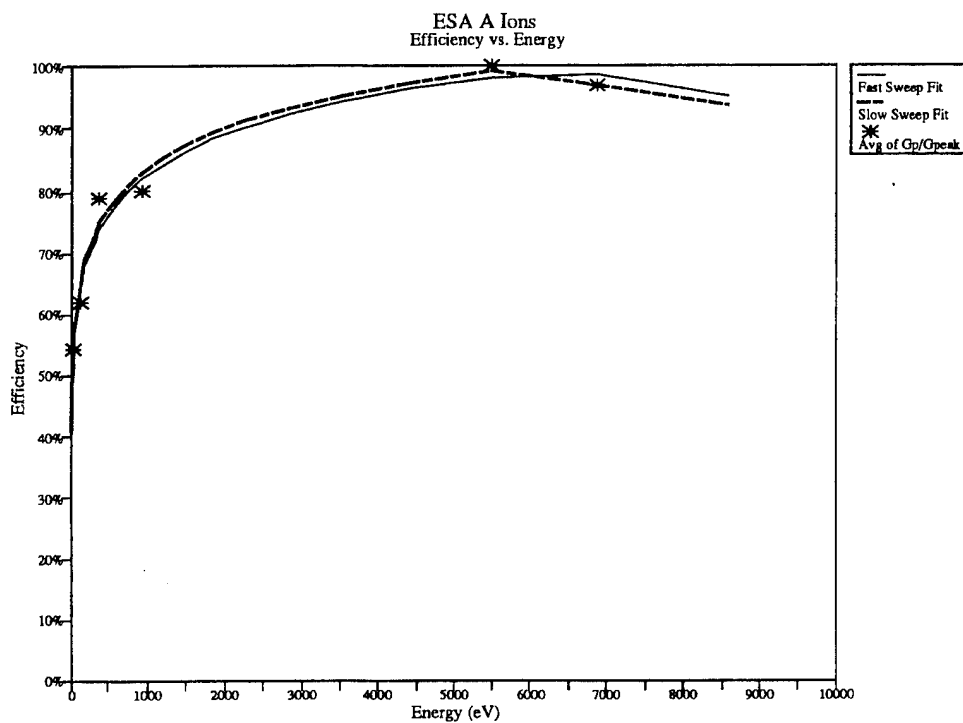


Figure 50. ESA A Ion Detection Efficiency Plotted Versus Energy

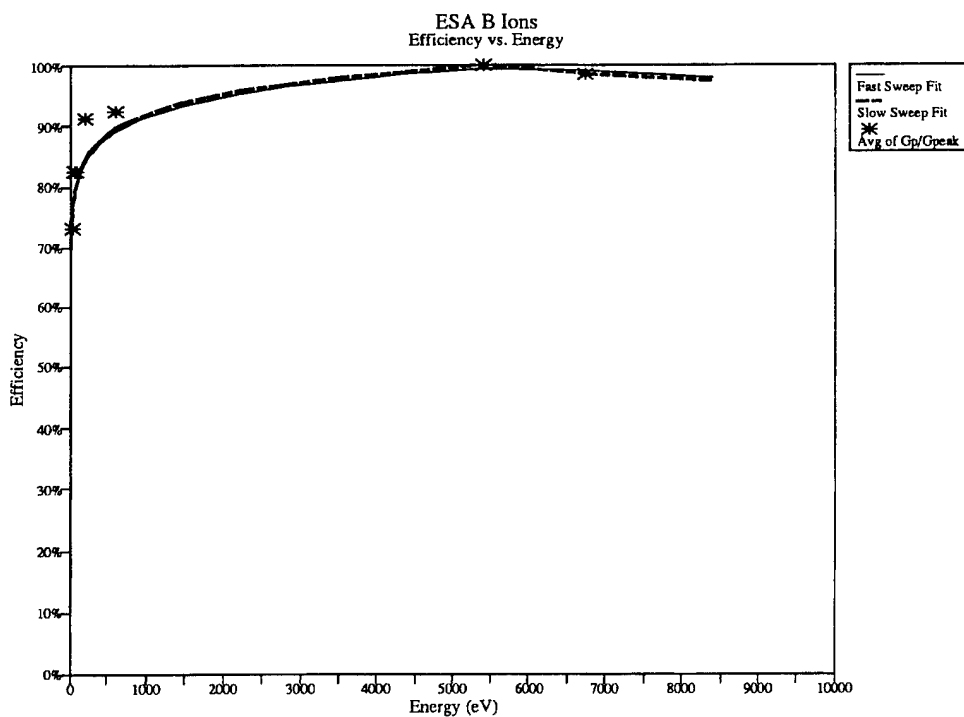


Figure 51. ESA B Ion Detection Efficiency Plotted Versus Energy

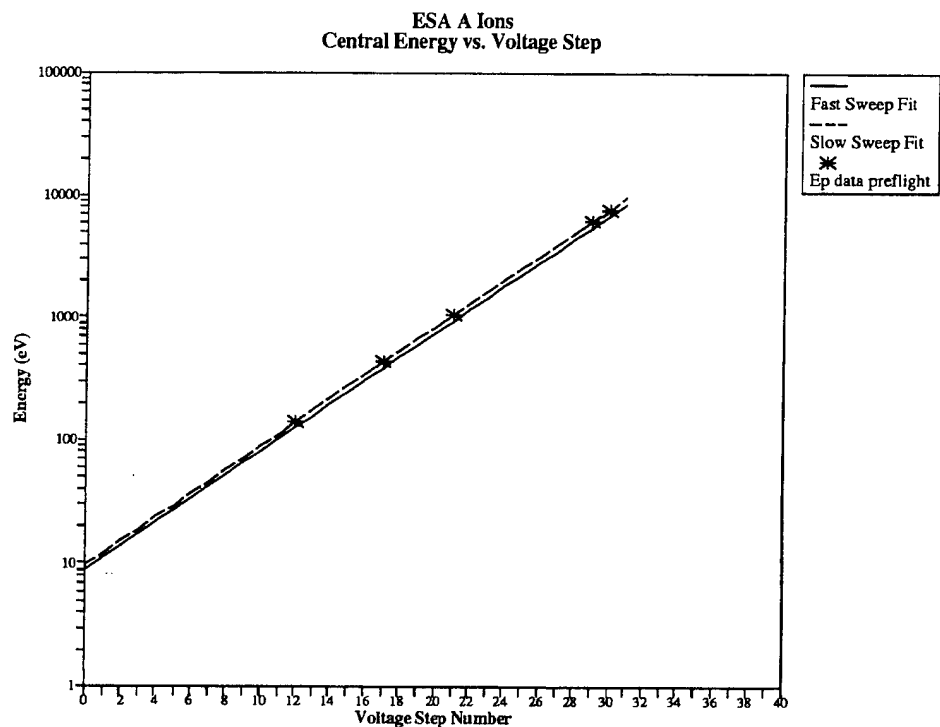


Figure 52. Central Energy of the ESA A Ion Channels Plotted Versus Channel Number

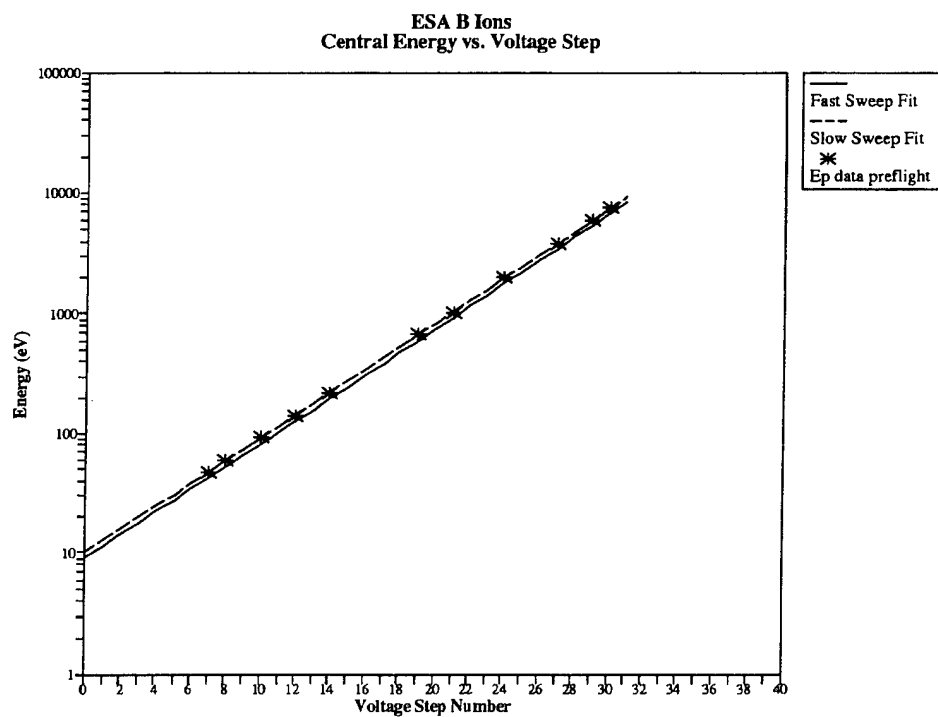


Figure 53. Central Energy of the ESA B Ion Channels Plotted Versus Channel Number

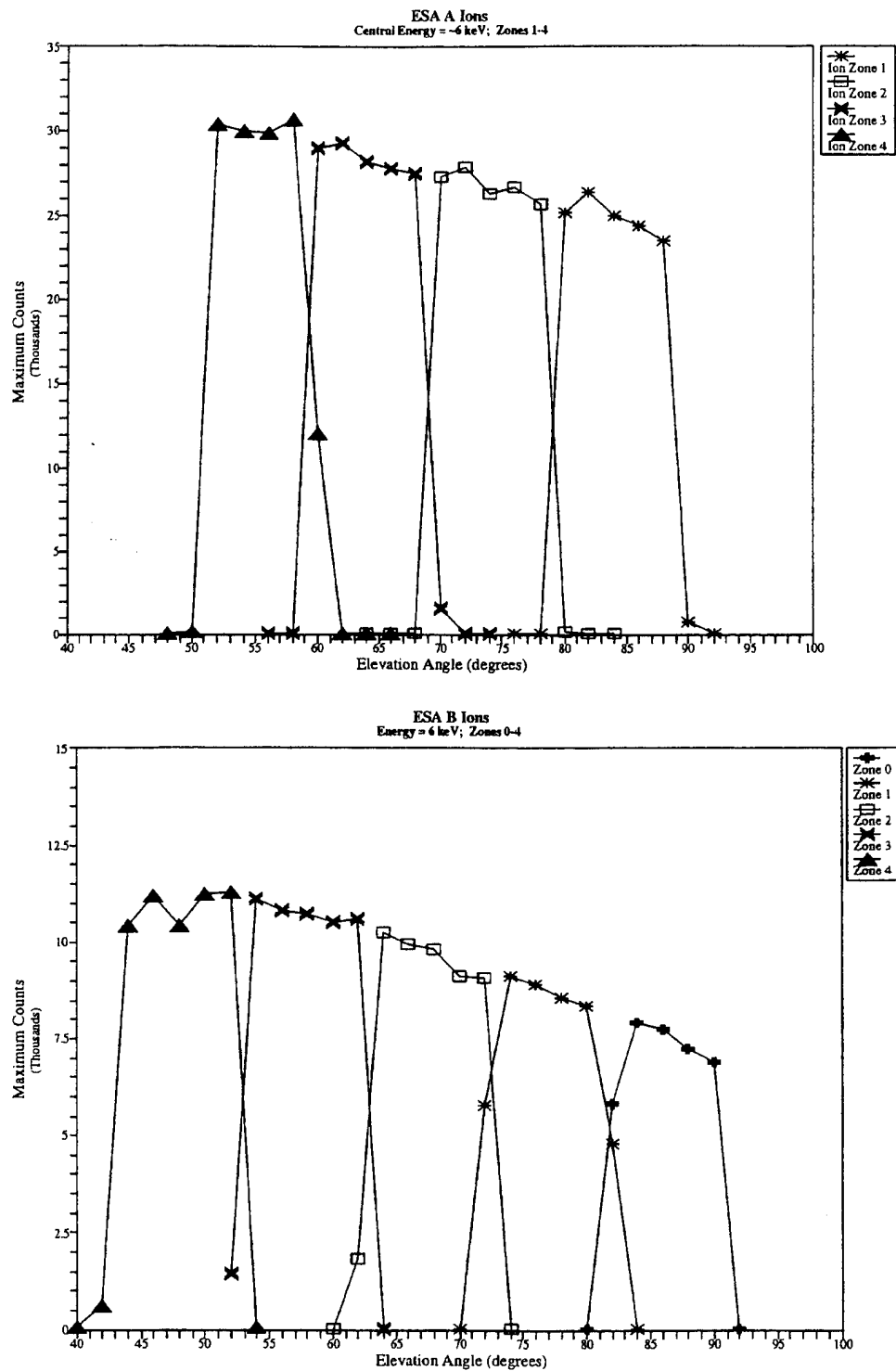


Figure 54. Counts Versus Elevation Angle for ESA A Ion Zones 1-4 and ESA B Ion Zones 0-4, for the Energy Channel With Peak Response at ~6 keV. a) Zones 1-4; b) Zones 0-4 The Data are for a Fixed Azimuth Angle Within the Angular Scan Such That the Elevation Plot Includes the Point of Maximum Count Rate in the Scan.

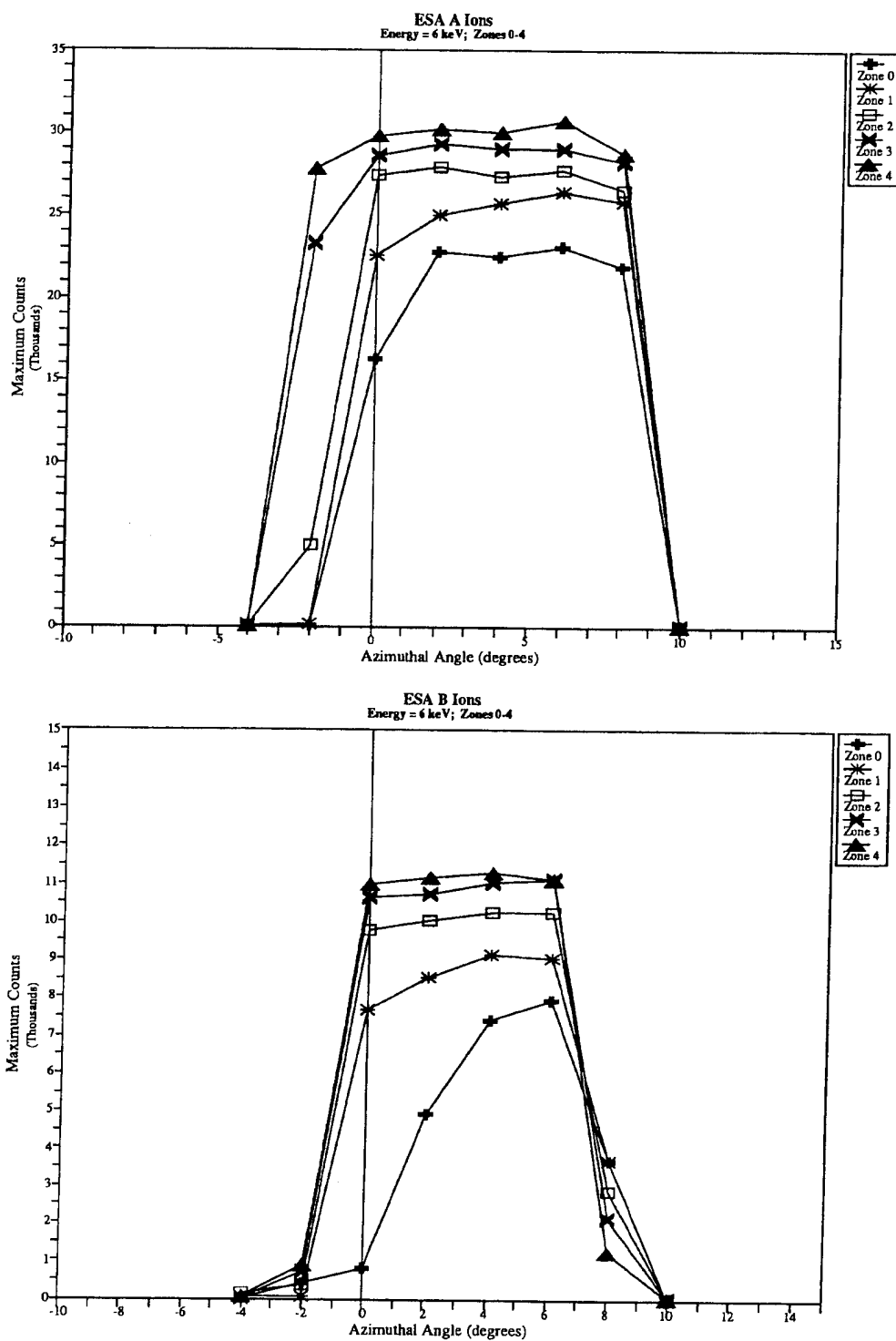


Figure 55. Counts Versus Azimuthal Angle for ESA A Ion Zones 0-4 and ESA B Ion Zones 0-4, for the Energy Channel With a Peak Response at ~6 keV. a) Zones 0-4; b) Zones 0-4 The Data are for a Fixed Elevation Angle Within the Angular Scan Such That the Azimuth Plot Includes the Point of Maximum Count Rate in the Scan.

References

- ¹ Hardy, D.A., Walton, D.M., Johnstone, A.D., Smith, M.F., Gough, M.P., Huber, A., Pantazis, J., and Burkhardt, R. (1993) The Low Energy Plasma Analyzer, *IEEE Trans. Nucl. Sci.* **40**:246
- ² Coates, A.J., Johnstone, A.D., Kellock, S.J., Smith, M.F., Booker, T., and Winningham, J.D. A space-borne plasma analyzer for three-dimensional measurements of the velocity distribution, submitted to IEEE 1984 Nuc. Sci. Symposium, Fla.
- ³ Johnstone, A.D., Coates, A.J., Wilken, B., Studemann, W., Weiss, W., Cerulli Irelli, R., Formisano, V., Borgs, H., Olsen, S., Winningham, J.D., Bryant, D.A., and Kellock, S.J. (1987) The Giotto three-dimensional positive ion analyser *J. Phys.*, (E)
- ⁴ McGarity, J.O., Huber, A., Pantazis, J., Oberhardt, M.R., Hardy, D.A., and Slutter, W.E., (1992) Compact ion/electron analyzer for spaceflight or laboratory use," *Rev. Sci. Instrum.*, **63**:1973
- ⁵ Oberhardt, M.R., Hardy, D.A., Slutter, W.E., McGarity, J.O., Sperry, D.J., Everest, A.W., III, Huber, A.C., Pantazis, J.A., and Gough, M.P. (1994) The shuttle potential and return electron experiment (SPREE) *Nuovo Cimento Sezione*, **17C**:67
- ⁶ Marshall, F.J., Hardy, D.A., Huber, A., Pantazis, J., McGarity, J., Holeman, E., and Winningham, J. (1986) Calibration system for electron detectors in the energy range from 10 eV to 50 keV," *Rev. Sci. Instrum.*, **57**(2):229
- ⁷ Wilton, R., Private communication, 1990
- ⁸ Enloe, C.L., Private communication, Operation of an ion calibration source over four orders of magnitude in energy, 1991
- ⁹ Kurz, E.A., (1979) Channel electron multipliers, *American Laboratory*
- ¹⁰ Paschmann, G., Shelley, E.G., Chappell, C.R., Sharp, R.D., and Smith, L.F. (1970) *Rev. Sci. Instrum.*, **41**:1706
- ¹¹ Huber, A., McGarity, J.O., Pantazis, J.A., Everest, A.W., Sperry, D.J., Moran, S.J., Gough, M.P., and Holeman, E. (1991) Prototype instrumentation and design studies, PL-TR-91-2236, ADA 248378